DISSERTATION

RESPONSE OF CONVECTIVE COLD POOLS AND PRECIPITATION TO CHANGES IN SOIL MOISTURE

Submitted by

Aryeh Jacob Drager

Department of Atmospheric Science

In partial fulfillment of the requirements

For the Degree of Doctor of Philosophy

Colorado State University

Fort Collins, Colorado

Spring 2020

Doctoral Committee:

Advisor: Susan C. van den Heever

Michael M. Bell
Christopher A. Davis
Michael J. Kirby
Wayne H. Schubert

ABSTRACT

RESPONSE OF CONVECTIVE COLD POOLS AND PRECIPITATION TO CHANGES IN SOIL MOISTURE

In Part 1 of this dissertation, we examine the role of soil moisture in modulating convective cold pool properties. This investigation is performed within an idealized modeling framework featuring a cloud-resolving model coupled to an interactive land surface model. Five high-resolution simulations of tropical continental convection are conducted in which the initial soil moisture is varied. The hundreds of cold pools forming within each simulation are identified and composited across space and time using an objective cold pool identification algorithm. Several important findings emerge from this analysis. Lower initial soil moisture results in greater daytime heating of the surface, which produces a deeper, drier subcloud layer. As a result, latent cooling through the evaporation of precipitation is enhanced, and cold pools are stronger and deeper. Increased gust front propagation speed, combined with wider rain shafts, results in wider cold pools. Finally, the "water vapor rings" that surround each cold pool under wet-soil conditions disappear under dry-soil conditions, due to the suppression of surface latent heat fluxes. Instead, when soils are dry, short-lived "puddles" of enhanced water vapor permeate the interiors of the cold pools. The results are nonlinear in that the properties of the cold pools in the two driest-soil simulations depart substantially from the cold pool properties in the three simulations initialized with wetter soil. The dividing line between the resulting wet-soil and dry-soil regimes is the permanent wilting point (PWP), below which transpiration is subdued. Land

surface-boundary layer-cloud interactions are found overall to play a key role in governing the properties of cold pools.

During Part 1 of this dissertation, we identify a novel "intermediate-soil moisture disadvantage" regime in which soils whose initial liquid water content slightly exceeds the PWP receive the least rainfall. In Part 2, we investigate the physical mechanisms behind this result. Four suites of ten idealized, high-resolution numerical experiments are conducted using the same modeling system used in Part 1. Each suite uses a distinct combination of soil type and vegetation, and within each suite, each simulation is initialized with a different amount of soil moisture. The "intermediate soil-moisture disadvantage" from Part 1 is reproduced. This result is found to stem from differing amounts of subcloud rain evaporation across the simulations, as well as from divergent balances between the level of free convection and the strength of boundary layer vertical motions. However, the result only holds for vegetated surfaces; bare-soil surfaces are instead found to exhibit a pure "wet-soil advantage" relationship. These results have important implications for the design of future process-level studies and large-scale model parameterizations.

ACKNOWLEDGMENTS

This work would not have been possible without the contributions of many people over the years. First and foremost, my absolutely brilliant advisor, Prof. Susan van den Heever, has provided unwavering support during the challenges of graduate school. She afforded me ample freedom to explore various topics of interest and to get to the "root" of the processes governing model trends, even when this involved "branching" out into vegetation and soil processes. And—despite my occasional protests—she has guided me toward becoming a more independent, confident scientist. Dr. Leah Grant, who is a coauthor on the papers arising from this dissertation, has also been an invaluable mentor and resource during my time as a Ph.D. student. Along with Sue, Leah helped me on numerous occasions to organize my ideas, and she also provided assistance during my attempts to understand the inner workings of RAMS and the LEAF-3 scheme. Thank you, Sue and Leah!

I also acknowledge Prof. Michael Bell, Dr. Christopher Davis, Prof. Michael Kirby, and Prof. Wayne Schubert for their willingness to serve on my doctoral committee, as well as for their insightful feedback and thought-provoking questions. In addition to those on my committee, Prof. Sonia Kreidenweis and Prof. David Randall have been superb mentors during my time at Colorado State University.

Thank you also to my current and past colleagues in the van den Heever research group—Jennie Bukowski, Nick Falk, Sean Freeman, Dr. Ross Heikes, Dr. Stacey Kawecki, Brianna Lund, Dr. Peter Marinescu, Yasutaka Murakami, Dr. Bowen Pan, Minnie Park, Dr. Emily Riley Dellaripa, Steve Saleeby, Alex Sokolowsky, Ben Toms, and Kristen Van Valkenburg—for moral support and helpful feedback along the way. I would also like to

acknowledge my colleagues on the American Meteorological Society's Student Conference Planning Committee Co-Chair Team—Dr. Josh Alland, Kristy Carter-Mauss, Dr. Stacey Hitchcock, Dr. Erik Nielsen, and Dr. Daniel Rothenberg—for contributing to the success of the 2017 and 2018 AMS Student Conferences that occupied so much of my time as a Ph.D. student. My friends Dr. Kenny Baclawski, Dr. Marie McGraw, Dr. Annareli Morales, and N. J. Rivilis also provided much-needed moral, accountability, and proofreading support as I approached the end of my dissertation writing process. Thank you to them, as well as to the many friends and colleagues that I have likely neglected to list here. Furthermore, thank you to the CSU Department of Atmospheric Science staff, who provided administrative, moral, and IT support.

I extend special thanks to all of the mentors that advised me during my undergrad years and graciously provided countless second chances when I struggled: Prof. Alex Barnett, Prof. Miles Blencowe, Dean Melissa Burt, Prof. Peter Doyle, Prof. Xiahong Feng, Prof. Susannah Heschel, Prof. Matt Igel, Prof. Robyn Millan, Prof. Erich Osterberg, Prof. John Pfister, Prof. Eric Posmentier, Dr. Paul Reasor, Prof. Christopher Sneddon, and Prof. B. Stuart Trembly. Thanks also to my primary and secondary school teachers in Peekskill, NY and West Hartford, CT, who provided a stellar public education.

None of this work would have been possible if not for the unconditional love and support provided by my mother, Jo; my father, Paul; my brother, Elon; my grandmother, Marilyn; and the rest of my family. Thank you so much!

Finally, this work was funded both by the National Science Foundation Graduate Research Fellowship Program under Grant No. DGE-1321845 Amend 5 and by the Office of Naval Research under Grant No. N00014-16-1-3093. All simulations were performed on the Navy Department of Defense Supercomputing Resource Center Cray XC40 system *Conrad*. The

vast majority of analyses were performed using MATLAB, and several figures were produced using the minspace.m code by Prof. Adele Igel.

TABLE OF CONTENTS

CHAPTER 1: INTRODUCTION

1.1 Background

This dissertation focuses on two interrelated aspects of atmospheric convection: cold pools and precipitation. Convective cold pools are surface-based regions of locally dense air that originates from convective downdrafts. Convective downdrafts occur when hydrometeor loading and latent cooling due to evaporation, melting, and/or sublimation act to increase the local density of air, causing it to accelerate downwards. When the downdraft air reaches the ground, it spreads laterally, forming an expanding pool of air that is denser than its surroundings, termed a *cold pool*. Cold pools are important for determining when and where convection will be initiated, and they also play an important role in maintaining certain types of convective organization, such as squall lines (Rotunno et al., 1988).

Cold pools can suppress the formation of new convection by increasing the near-surface static stability and providing a source of sinking motion. On the other hand, they can trigger new convection around their peripheries both by (1) providing a source of lift by wedging beneath surrounding air, termed *mechanical forcing* (Jeevanjee & Romps, 2015; Torri et al., 2015); and (2) creating rings of enhanced water vapor content that circumscribe the cold pool, thereby reducing convective inhibition (CIN), lowering the level of free convection (LFC), and increasing convective available potential energy (CAPE) so as to enable new convection to form more easily (Tompkins, 2001). The latter mechanism is termed *thermodynamic forcing* and is somewhat controversial, as currently there is minimal observational support for the existence of "water vapor rings" (also sometimes termed "moist patches" or "moisture rings"), which have been proposed to exist based primarily on numerical modeling studies (Chandra et al., 2018;

Langhans & Romps, 2015; Schlemmer & Hohenegger, 2016; de Szoeke et al., 2017; Tompkins, 2001; Torri & Kuang, 2016; Zuidema et al., 2017). These two forcings can, in principle, be present simultaneously and can therefore work in concert to initiate new convection.

The second focus of this dissertation is afternoon convective precipitation, i.e., the rainfall that develops from convective clouds during the mid-to-late daytime hours. Afternoon convective precipitation is the dominant form of precipitation in many continental regions (Tan et al., 2019) and is therefore important for the hydrologic cycle and agriculture. Despite its importance, many models experience difficulty predicting the timing and amount of rain that will fall (Baranowski et al., 2018; Dirmeyer et al., 2012; Hohenegger et al., 2009). This is due, in part, to the representation of cold pools, which by triggering new convection act to extend the diurnal cycle of convective rain later into the afternoon and evening (Rio et al., 2009).

An important source of uncertainty in model representations of both continental cold pools and continental afternoon precipitation is their interaction with the land surface. The land surface exchanges sensible heat, latent heat, and momentum with the boundary layer air above, and it also interacts with radiation (e.g., Stull, 1988). The land surface also exchanges mass with the air above through processes such as the lofting of dust (Tegen & Fung, 1994) and the infiltration of rain into the soil (Morin & Benyamini, 1977). Of particular interest to the research described in this dissertation is soil moisture, defined as the amount of liquid water present in the soil. The wetness or dryness of the soil surface determines how the net incoming solar radiation (insolation) is partitioned into fluxes of sensible and latent heat. When the soil is dry, sensible heat fluxes dominate, and when the soil is wet, latent heat fluxes dominate (Stull, 1988). When vegetation is present, there are two potential sources of latent heat fluxes: direct evaporation of water from the top of the soil, and transpiration by plants. Together, these are referred to as

evapotranspiration. By warming the near-surface air, sensible heat fluxes help to generate strong vertical motions and turbulent eddies that entrain air from above into the boundary layer. Latent heat fluxes help to moisten the boundary layer.

1.2 Motivation and Goals

How, then, does the land surface relate to cold pools and afternoon convective precipitation? Aspects of this question have been explored in depth by previous studies. For example, Grant and van den Heever (2018) show using an atmospheric large-eddy simulation coupled to a land surface model that two-way atmosphere-land surface interactions result in slightly stronger cold pool interiors and substantially weaker cold pool edges when compared to a simulation in which these two-way interactions are absent. Drager and van den Heever (2017) find that rain from cold pools' parent convection soaks and cools the land surface beneath, resulting in negative sensible heat fluxes (i.e., fluxes of sensible heat from the atmosphere into the ground) that help to strengthen the cold pools. Additionally, work by Grant and van den Heever (2014) and Drager (2016) has suggested that cold pools are stronger under dry-soil conditions than under wet-soil conditions. However, these two studies examine a set of simulations whose resolution is too coarse to fully resolve important cold pool dissipation processes (Grant & van den Heever, 2016). The goal of Chapter 2 of this dissertation is to revisit the science question of how cold pools respond to changes in soil moisture using high-resolution simulations that are able to resolve cold pool dissipation processes.

A large body of literature exists regarding the interactions between soil moisture and afternoon convection (Santanello et al., 2017). This body of literature has identified several different types of relationships, including a "wet-soil advantage," in which wetter soils generate earlier clouds and/or more precipitation (Findell et al., 2011; Findell & Eltahir, 2003); a "dry-soil

advantage," in which clouds form earlier and/or generate more precipitation over drier soils (Findell & Eltahir, 2003; Taylor et al., 2012); and a non-monotonic regime with an intermediate-soil wetness advantage (Barthlott & Kalthoff, 2011). In Chapter 2, we identify for the first time a non-monotonic regime featuring an intermediate-soil wetness *disadvantage* with respect to both the timing and amount of accumulated precipitation. The goal of Chapter 3 is to explore the physical mechanisms behind this new type of soil moisture-precipitation interaction, as well as its sensitivity to vegetation and soil texture.

1.3 Methods

Throughout the dissertation, the open-source Regional Atmospheric Modeling System (RAMS), which is coupled to the Land Ecosystem–Atmosphere Feedback version 3 (LEAF-3) soil-vegetation-atmosphere transfer scheme, is used to conduct high-resolution numerical experiments in order to address our scientific goals. Although specific experiment details vary between Chapter 2 and Chapter 3, the basic setup of the numerical simulations is the same. Each simulation is initialized with a different spatially homogeneous soil moisture level and is allowed to evolve for 14 hours from 07:00 LT to 21:00 LT. Then, various analytical tools are applied, and the differences across simulations—and, ultimately, the physical mechanisms—are assessed.

1.4 Dissertation Structure

In Chapter 2, we discuss how convective cold pools change under different soil moisture conditions, and in Chapter 3, we probe the relationship between afternoon convective precipitation and soil moisture, with a focus on the intermediate-soil moisture disadvantage with respect to precipitation from Chapter 2. In Chapter 4, we provide some concluding remarks and suggest avenues for future inquiry. Chapter 2 has been accepted pending revision at the Journal

of Advances in Modeling Earth Systems, and Chapter 3 is currently in preparation for submission to the peer-reviewed literature.

CHAPTER 2: COLD POOL RESPONSES TO CHANGES IN SOIL MOISTURE

2.1. Introduction

Convective cold pools help to modulate convective processes by suppressing convection in some locations while promoting it in other regions. Subsidence and enhanced boundary layer static stability suppress the formation of new convection in the interiors of existing cold pools (Tompkins, 2001). Meanwhile, cold pools trigger convection mechanically via the propagation of gust fronts, which lift surrounding boundary layer air to its level of free convection (e.g., Moncrieff & Liu, 1999; Torri et al., 2015). Through some combination of rain evaporation, enhanced latent heat fluxes, and advection of preexisting moisture anomalies, cold pools may also cause the accumulation of water vapor into "rings" near cold pool boundaries (Langhans & Romps, 2015; Schlemmer & Hohenegger, 2016; Tompkins, 2001; Torri & Kuang, 2016). These water vapor rings have the potential to make cold pool peripheries thermodynamically favorable for the formation of new convection.

Several recent studies have performed detailed analyses of processes governing the emergence of water vapor rings in models. Langhans and Romps (2015) conclude that water vapor rings are generated primarily by latent heat fluxes. Schlemmer and Hohenegger (2016) confirm that latent heat fluxes are more important than evaporation of precipitation for providing water vapor to the water vapor rings (their "moist patches") but also note that a substantial fraction (one-third to one-half) of the water vapor comes from moisture present in the subcloud layer prior to cold pool onset. In agreement with Schlemmer and Hohenegger (2016), Torri and Kuang (2016) suggest that latent heat fluxes are more important than evaporation of precipitation but that the latter cannot be neglected, particularly near the surface. Torri and Kuang (2016) and

Langhans and Romps (2015) consider only cold pools over ocean, whereas Schlemmer and Hohenegger (2016) consider cold pools both over land and over ocean.

The precise location of water vapor rings relative to cold pools' boundaries, i.e., whether they are inside, outside, or co-located with cold pools' gust fronts, has been the subject of some debate. In previous modeling studies, these rings have generally formed inside of the gust fronts bounding cold pools. However, observations of cold pools over tropical oceans suggest that these rings, if they exist at all, are co-located with or outside of the gust fronts (Chandra et al., 2018; de Szoeke et al., 2017; Zuidema et al., 2017).

In addition to modifying the location of convection, cold pools influence the nature of convection. Cold pools result in the formation of wider and deeper clouds, especially when cold pools collide with one another (Böing et al., 2012; Feng et al., 2015; Purdom, 1982; Schlemmer & Hohenegger, 2014; Wilson & Schreiber, 1986). In fact, the diurnal transition from shallow to deep convection can be suppressed in numerical models by eliminating the processes that generate cold pools (Khairoutdinov & Randall, 2006; Kurowski et al., 2018).

Despite their importance for convective initiation and organization, cold pools have only recently begun to be incorporated into climate models' convective parameterization schemes (Del Genio et al., 2015; Park, 2014; Rio et al., 2013; Suselj et al., 2019; Zhao et al., 2018). Several aspects of cold pool science, such as microphysical controls on cold pool development (e.g., Dawson et al., 2010; Falk et al., 2019; Grant & van den Heever, 2015; van den Heever & Cotton, 2004; Li et al., 2015; Mallinson & Lasher-Trapp, 2019; Morrison, 2012) and interactions between cold pools and the land or ocean surfaces below (Drager & van den Heever, 2017; Fast et al., 2019; Gentine et al., 2016; Grant & van den Heever, 2016, 2018; Huang et al., 2018; Kurowski et al., 2018; Pei et al., 2018), remain active areas of research. It has also been

recognized that boundary layer properties influence cold pool properties. Deeper boundary layers result in stronger cold pools, as do drier boundary layers (McCaul Jr. & Cohen, 2002). However, interactions between the surface and boundary layer as they pertain to cold pool development have not been examined. This is the area to which the present work aims to contribute.

We investigate the hypothesis that changes in soil moisture result in interactions between the surface, boundary layer, and clouds that feed back onto various cold pool properties such as size, strength, structure, and longevity. Soil moisture helps to govern the Bowen ratio, the ratio of sensible to latent heat fluxes at the surface (Bowen, 1926), by determining the amount of soil water available for evaporation directly off of the soil surface, as well as the vigor of transpiration by vegetation (e.g., Lee, 1992). If the evapotranspiration is limited, then in order to achieve surface energy balance, the sensible heat flux must increase. Therefore, if all else is equal, then decreased soil moisture results in enhanced surface sensible heat fluxes and suppressed surface latent heat fluxes and thus an increased Bowen ratio (e.g., Garratt, 1992). Surface fluxes influence cold pool longevity both directly, through the injection and removal of sensible heat and moisture into the cold pool, and indirectly, by fueling boundary layer circulations and turbulence in the near-cold pool environment that interact with the cold pool via entrainment (Grant & van den Heever, 2016, 2018). The cold pool longevity and structure, in turn, impact the likelihood and location of cold pool triggering of new convection.

The present work was conducted in synergy with the United States Office of Naval Research's Propagation of Intra-Seasonal Tropical OscillatioNs (PISTON) field campaign that took place during 2018 and 2019. The PISTON field campaign aims to improve our understanding of several factors, including land-atmosphere interactions, that affect the propagation of the Boreal Summer Intraseasonal Oscillation (BSISO) through the Maritime

Continent, with a particular emphasis on the Philippines archipelago (Office of Naval Research, 2016). Cold pools are of particular interest given the potential importance of scale interactions between individual convective cells and larger features of the atmospheric circulation (Toms et al., 2020). Furthermore, it is hypothesized that cold pools in this region, in concert with other processes such as mountain circulations and land/sea breezes, impact the diurnal cycle of convection (e.g., Riley Dellaripa et al., 2020). The diurnal cycle in this region is not represented well in most climate models (e.g., Baranowski et al., 2018; Dirmeyer et al., 2012) or regional models (e.g., Riley Dellaripa et al., 2020). Cold pool parameterizations in convection-parameterizing models can potentially improve the simulated diurnal cycle in continental environments (Rio et al., 2009). With an eventual goal of improving these parameterizations, and thereby improving the representation of the diurnal cycle, the present study seeks to clarify whether, and to what extent, soil moisture affects cold pool properties.

This work investigates the effects of soil moisture on cold pool development in a set of numerical model simulations. Five idealized simulations of tropical continental convection are performed, each with a different initial soil moisture content. Composites of the cold pools in each simulation are created using a cold pool identification algorithm, and statistics are calculated. The differences between the various simulations' composites are then assessed in order to elucidate the physical mechanisms. Finally, the results are discussed in the context of convective initiation.

2.2 Model Setup, Sensitivity Experiments, and Analysis Methods

2.2.1 Model Setup and Sensitivity Experiments

In this study, we perform simulations using the open-source Regional Atmospheric Modeling System (RAMS) (vandenheever.atmos.colostate.edu/vdhpage/rams.php) (Cotton et al.,

2003), release 6.2.08. RAMS, which is a regional, non-hydrostatic atmospheric model and is fully coupled to the Land-Ecosystem-Atmosphere Feedback version 3 (LEAF-3) soil-vegetation-atmosphere transfer model (Lee, 1992; Walko et al., 2000), contains a sophisticated double-moment, bin-emulating bulk microphysics scheme with eight hydrometeor classes. The full model settings are provided in Table 2.1; selected aspects specific to these simulations are discussed below.

The idealized simulations are performed on a non-rotating ($f = 0\ s^{-1}$) domain with doubly periodic lateral boundaries and no topography. The domain size is 150 km × 150 km × ~21 km, the horizontal grid spacing is 125 m, and the vertical grid spacing is stretched from 40 m to 250 m (127 vertical levels). At this resolution, it is expected that the largest atmospheric turbulent eddies are resolved (i.e., large-eddy simulation); the effects of smaller eddies are parameterized using a modified form of the Smagorinsky (1963) scheme (Table 2.1). Based on sensitivity tests at various resolutions, Grant and van den Heever (2016) recommend that horizontal (vertical) grid spacing of 100 m (50 m) be used in order to represent turbulent cold pool dissipation processes accurately. The simulations performed here approach this resolution. The coupled LEAF-3 model contains 11 soil levels that extend to a depth of 0.5 m following Grant and van den Heever (2014). The simulations are initialized at 07:00 LT and run for 14 hours, so as to capture a single day's diurnal cycle of convection, with output files saved every 5 minutes.

The initial conditions are horizontally homogeneous except for pseudorandom thermal perturbations in the lowest ~500 m of the atmosphere. The initial atmospheric conditions are based on the conditions on the island of Luzon, Philippines during boreal summer. The initial winds are calm, and the initial thermodynamic and moisture profiles are obtained from the Laoag site in Luzon (http://weather.uwyo.edu/upperair/sounding.html). The profiles used in this study

are adapted from the 0 UTC (~8 LT) sounding on 2 August 2010. This particular morning sounding is chosen because it corresponds to the active phase of the BSISO over Luzon, it is nearly free of apparent cloud layers, it is not influenced by tropical cyclone activity, the winds are weak, and convection is observed to develop later in the day. The red curves in Figure 2.1 show the raw sounding data. Before the sounding data are used to initialize the model, the "spike" in water vapor content at 152 hPa is removed, and then the thermodynamic and water vapor profiles are smoothed using a running mean filter with a span of 2 km. The resulting smoothed sounding is shown by the thick black curves in Figure 2.1. Although we are using a 0 UTC (8 LT) sounding, the model is initialized with this sounding at 23 UTC (7 LT) in order to allow for more model spin-up time.

The soil texture used in the LEAF-3 model is silty clay loam, the vegetation class is wooded grassland, and the prescribed Normalized Difference Vegetation Index (NDVI) is 0.6. These settings are selected to be roughly representative of Luzon during early August based on the RAMS global datasets of soil texture, vegetation class, and monthly NDVI.

Five sensitivity simulations, the DRENCHED-SOIL, WET-SOIL, MID-SOIL, PWP-SOIL (named for the permanent wilting point, which is further discussed in Section 2.2.2), and DRY-SOIL simulations, are performed. The initial uniform soil moisture values in these simulations are 95%, 75%, 50%, 45%, and 25% of the saturation volumetric soil moisture (0.477 $m^3\ m^{-3}$), respectively, and the initial soil temperatures (identical in all simulations) are slightly warmer than those of the air above, following Grant and van den Heever (2014). The 95% value is roughly typical of the mean conditions over Luzon in ERA5 reanalyses (Copernicus Climate Change Service (C3S), 2017) during the boreal summers of 2010 and 2016, representing weak and strong BSISO seasons, respectively, and the 45% and 50% values are approximately

representative of the dry season (based on January through May of the same years). The 75% value is representative of the driest conditions over Luzon during boreal summer in reanalysis, and the 25% value is indicative of drought.

2.2.2 Overview of the Simulations

Figure 2.2 shows domain-mean vertical profiles of various quantities, averaged over a time period extending from 11:00 LT to 18:00 LT, for all four simulations. As is discussed later, this time window corresponds to our cold pool analysis period. In general, there are substantial differences between the two driest-soil simulation and the three wetter-soil simulations, which are quite similar to each other for all of the fields compared here. Figures 2.2a, 2.2b, and 2.2e indicate that the boundary layer becomes warmer, drier, and deeper with decreasing soil moisture. The thermodynamic variable plotted in Figure 2.2a is the density potential temperature θ_ρ, which is defined following (Emanuel, 1994a) as $\theta \frac{1+\frac{R_v}{R_d} r_v}{1+r_v+r_{\text{cond}}} \approx \theta(1 + 0.608 r_v - r_{\text{cond}})$, where θ is the potential temperature, R_v is the gas constant of water vapor, R_d is the gas constant of dry air, r_v is the water vapor mixing ratio, and r_{cond} is the total condensate mixing ratio. The density potential temperature is similar to the virtual potential temperature except that it contains an extra correction for density increases due to condensate loading. It has been used in previous studies (e.g., Drager & van den Heever, 2017; Feng et al., 2015; Tompkins, 2001) to define cold pool regions and boundaries. Although all five simulations are initialized with the same atmospheric profile, the partitioning between surface sensible and latent heat fluxes, which is governed in part by the amount of soil moisture, dictates the amount of near-surface heating and moistening. Decreased soil moisture leads to decreased evapotranspiration and increased sensible heating. Increased sensible heating, in turn, leads to increased near-surface static instability and thus more vigorous and deeper boundary layer mixing. The water vapor mixing ratio (r_v) within

the boundary layer decreases with drier soil because surface latent heat fluxes are diminished and more dry air from above is entrained into the boundary layer by the boundary layer turbulence. Within the boundary layer, increasing temperature and decreasing r_v combine to yield decreased relative humidity and increased saturation deficit (defined here as the difference between the saturation r_v and the actual r_v) with decreasing soil moisture, as shown by Figures 2.2c and 2.2d, respectively.

The cloud-base height increases with decreasing soil moisture (Figure 2.2e), in concert with the increasing boundary layer depth. A perhaps less intuitive result is that the maximum domain-mean cloud water mixing ratio more than doubles in the PWP-SOIL and DRY-SOIL simulations compared to the other three simulations. When this average is taken only over cloudy points, most of this discrepancy disappears (not shown), which indicates that the increase in domain-mean cloud water mixing ratio is dominated by an increase in the cloud fraction (likely a combination of increased number of clouds and increased cloud size) rather than the in-cloud mixing ratio.

We now discuss precipitation production and accumulation, which will help us later to understand the differences in the cold pool properties. The domain-mean precipitation mixing ratio (Figure 2.2f) reaches a greater value aloft in the PWP-SOIL and DRY-SOIL simulations than in the other three simulations. A similar result was obtained by Hu et al. (2017), who compared regions with soils with stronger sensible heat fluxes to regions whose soils had lower sensible heat fluxes. However, they attributed this trend to a "soil-type breeze" similar in character to a land-sea breeze circulation, which is necessarily quite different from the mechanism acting here due to the present study's relative spatial homogeneity in any given simulation. However, this difference in domain-mean precipitation mixing ratio is smaller at the

surface than aloft, which indicates that much more precipitation is evaporating aloft in the PWP-SOIL and DRY-SOIL simulations. Curiously, the MID-SOIL simulation exhibits the least precipitation throughout the column. This intermediate-soil-wetness disadvantage with respect to precipitation will be explored in future work.

In order to understand the nonlinear trends with respect to soil moisture in Figures 2.2a–f, it is important to recognize that soil moisture is allowed to evolve in these simulations. Figure 2.2g shows the evolution of soil moisture saturation fraction for the top and bottom soil layers in each simulation (located at heights of −1 cm and −50 cm, respectively). In the DRENCHED-SOIL simulation, water drains from the upper soil layers into the lower layers due to gravitational settling during the early hours of the simulation, and soil moisture generally decreases in the bottom soil layer during the mid-day and afternoon due to root uptake of water that is transpired into the atmosphere. In the WET-SOIL simulation, the soil loses water from all layers during the mid-day and early afternoon, but during in the late afternoon and evening hours, the top-layer soil moisture partially recovers due to a combination of precipitation and upward conduction of water from the lower layers. The MID-SOIL simulation's soil is sufficiently dry that there is little conduction of water from low layers into the top layer. As a result, the uppermost soil layer becomes decoupled from the layers below (i.e., the uppermost layer ceases to draw much water from the layers beneath), and its soil moisture saturation fraction decreases to approximately 30%. The soil moisture in the lower layers drops throughout the day. The uppermost soil layer in the PWP-SOIL simulation exhibits qualitatively similar behavior to that of the MID-SOIL simulation, and the bottom layer's soil moisture remains nearly constant throughout the simulation. Finally, in the DRY-SOIL simulation, there is a slight

drop in the moisture of the top soil layer over the course of the day, whereas the moisture of the bottom soil layer remains approximately constant.

Also plotted in Figure 2.2g are the field capacity (the amount of soil moisture retained by soil following gravitational draining; 67.5% for the soil type used in the present study) and the permanent wilting point (hereafter PWP, 45.7%) (Lee & Pielke, 1992). The PWP, which is defined as the soil moisture threshold below which plants' roots are unable to absorb enough water to offset losses via transpiration, has been hypothesized to play an important role in the development of atmospheric circulations over land (Hohenegger & Stevens, 2018) because of its role in modulating latent heat fluxes and thus the Bowen ratio. Unlike the simplified soil model used by Hohenegger and Stevens (2018), the LEAF-3 model includes both evaporation and transpiration. Evaporation from the top soil layer into the atmosphere depends on the soil surface specific humidity, which is parameterized following the RAMS Technical Manual (vandenheever.atmos.colostate.edu/vdhpage/rams/docs/RAMS-TechnicalManual.pdf) to be a function of the field capacity, not the PWP. In this formulation, the ground water vapor mixing ratio is multiplied by a wetness factor that equals one when the top layer of soil is wetter than the field capacity, zero when soil is completely dry, and increases gradually with increasing soil moisture between these two extremes. By contrast, transpiration from the root-zone soil layers into the atmosphere is a function of the PWP via its dependence on soil water potential (Lee, 1992). Transpiration is controlled by multiple factors, including soil moisture, and the stomatal conductance's dependence on soil moisture is nearly a step function whose threshold is the PWP. Readers are referred to the aforementioned RAMS Technical Manual, as well as Philip (1957), and Lee and Pielke (1992), for more information about the model's treatment of surface

evaporation, and readers are directed to Lee (1992) for additional details about transpiration in LEAF-3.

Therefore, we may consider there to be three relevant soil moisture regimes within this modeling system. In the wettest regime, with soil moisture greater than the field capacity, there is sufficient soil moisture for both evaporation and transpiration. Within this regime, neither evaporation nor transpiration is a strong function of soil moisture. In the intermediate regime, with soil moisture between the field capacity and PWP, evaporation decreases with decreasing soil moisture, while transpiration remains approximately constant. Finally, in the driest regime, with soil moisture below the PWP, evaporation continues to decrease with decreasing soil moisture, and transpiration is essentially nonexistent. The DRENCHED-SOIL and WET-SOIL simulations represent the wettest regime, the MID-SOIL simulation falls within the intermediate regime, and the PWP-SOIL and DRY-SOIL simulations are part of the driest regime. The nonlinearities apparent across these simulations can be viewed through this lens: the DRENCHED-SOIL and WET-SOIL simulations are nearly identical, and the PWP-SOIL and DRY-SOIL simulations diverge sharply from the other three. The fact that the MID-SOIL simulation more closely resembles its moister counterparts than it does the PWP-SOIL simulation (despite 50% being much closer numerically to 45% than to 75%) provides evidence that transpiration is more important than evaporation in these highly vegetated simulations.

Figures 2.3a and 2.3b show representative snapshots of a sub-region of the WET-SOIL and DRY-SOIL simulations, respectively. In both simulations, the convection is isolated, as might be expected given the calm initial winds, and reaches depths characteristic of cumulus congestus clouds. Many cold pools [apparent as blue blotches in the near-surface density potential temperature (θ_ρ) field] form, and the cold pools are approximately stationary (i.e., not

advected by the mean wind; not shown) and nearly circular in both cases. Note, however, that the color scales for θ_ρ are quite different between the two simulations, in agreement with the variation shown in Figure 2.2a. The DRY-SOIL simulation exhibits higher mean values of θ_ρ, along with greater variability in θ_ρ values.

2.3 Analysis Approach

An updated version of the cold pool identification and tracking algorithm of Drager and van den Heever (2017) is used to analyze the ensemble of cold pools developing within each simulation. Although the spirit of the algorithm is unchanged, new features have been added, and the implementation has shifted from pixel-based cold pools to polygon-based cold pool boundaries for greater precision. The updates made to the Drager and van den Heever (2017) algorithm are discussed in Section A.1 of the Appendix.

Once the cold pool tracking is complete, the cold pools are aligned in space, according to the centers of their respective cylindrical polar coordinate systems, and in time, according to their individual respective reference times (t = 0 minutes, defined for each cold pool to be the time the cold pool is first identified; see Section A.1 for more information). Composites are then generated. To create the composites, each field $\psi(x, y, z, t)$, where t is defined relative to t = 0 minutes and ψ could represent any variable such as, e.g., θ_ρ or vertical velocity w, is linearly interpolated to two types of cylindrical polar grids. In the first type of cylindrical polar grid, the radial coordinate is normalized by the cold pool radius at each azimuth (see Figure 2.4), in a manner similar to that of Langhans and Romps (2015). In the second type, the radial coordinate is not normalized. Then, azimuthal averaging is performed to yield $\psi(r_{\text{norm}}, z, t)$ (normalized radial coordinate) and $\psi(r, z, t)$ (non-normalized) for each variable for every cold pool, with radial spacing of $\Delta r_{\text{norm}} = \frac{1}{15}$ and $\Delta r = 0.25$ km. Finally, composite fields are computed by

taking the arithmetic mean of $\psi(r_{\text{norm}}, z, t)$ and $\psi(r, z, t)$ across the full set of cold pools in each simulation.

An important distinction between the normalized and non-normalized composites is that, although every cold pool is included in the $t = 0$ minutes normalized composites, fewer cold pools are included before and after $t = 0$ minutes based on whether, and to what extent, each cold pool can be tracked backward or forward in time. By contrast, non-normalized composites can be constructed in the absence of cold pool boundary contours, and therefore all cold pools are included in the composites at each time relative to $t = 0$ minutes. The non-normalized composites are computed as far backward as $t = -60$ minutes, in order to capture the environments in which cold pools form, and as far forward as $t = 120$ minutes, so that cold pool dissipation may be assessed. The disadvantage of using non-normalized composites is that "smearing" of the cold pool features occurs due to differing sizes within each ensemble of cold pools, or even at different azimuths within a given cold pool.

2.4 Cold Pool Characteristics

2.4.1 Analysis Period and Numbers of Cold Pools

The remaining analyses presented in this paper consider only those cold pools whose $t = 0$ minutes reference times fall between 11 LT and 16 LT, inclusive. Few cold pools form before 11 LT. Cold pools forming after 16 LT—whose contributions to the composites would extend until after 18 LT—are excluded from the analyses in order to prevent processes that occur only during the evening and nighttime hours, such as dew formation, from influencing the composites. Therefore, only daytime cold pool dissipation processes are considered in the present study. The total numbers of unique cold pools in each simulation that fall within our analysis period are 1869 (DRENCHED-SOIL), 1996 (WET-SOIL), 1930 (MID-SOIL), 3311 (PWP-SOIL), and

3282 (DRY-SOIL). Time series indicating when these cold pools form are shown in Figure A.2 in the Appendix.

2.4.2 Cold Pool Area Statistics

Figure 2.5 displays information about cold pool area. It is immediately apparent from Figure 2.5a that the cold pools in the PWP-SOIL and DRY-SOIL simulations have about twice the area of those in the other three simulations, in a mean sense. This trend holds throughout the plotted time interval. Figures 2.5c and 2.5d corroborate the trend of larger cold pools in the PWP-SOIL and DRY-SOIL simulations: the PWP-SOIL and DRY-SOIL simulations exhibit a smaller fraction of small cold pools and a larger fraction of large cold pools.

The cold pool identification and tracking algorithm operates by looking for well-defined density potential temperature boundaries. If no such boundary exists, or if the boundary is blurred or irregular at a given time, then the algorithm will not identify a cold pool. Therefore, the length of time over which a cold pool is tracked in the final tracking stage can be roughly interpreted as a cold pool lifetime. Under this interpretation, it is apparent from Figure 2.5b that cold pools in the PWP-SOIL and DRY-SOIL simulations are shorter-lived than those in the other three simulations, in agreement with the results shown in Figure A.2 in the Appendix. The topic of cold pool longevity is revisited in Section 2.5.3.

2.4.3 Cold Pool Strength

In the discussion that follows, perturbation quantities are compared in order to allow cold pool properties to be assessed independently of the differences between the simulations' horizontal mean states. All perturbation quantities are calculated as departures from a simulation-dependent, height-dependent, time-varying horizontal mean.

Figure 2.6 shows probability density functions (PDFs) and mean values of various metrics of cold pool strength (Drager & van den Heever, 2017). For reference, several of these quantities are illustrated in Figure 2.4b. The equivalent potential temperature perturbation, θ_e', is included because it has previously been used to identify cold pools, although we will argue that this metric can be misleading (see Section 2.4.5). These PDFs are generated using the non-normalized, azimuthally averaged values at the lowest above-ground model level and within 4 km of the cold pool center across times −60 minutes ≤ t ≤ 120 minutes, except for the maximum updraft: the maximum updraft is obtained for radii between 0.75 km and 4 km and only for $t \geq 0$ minutes, in order to ensure that the value corresponds to the maximum uplift along the gust front rather than the earlier updraft that generates cold pool's parent cloud. Using minimum or maximum azimuthally averaged values rather than pointwise extrema prevents contamination from nearby cold pools.

Examination of Figures 2.6a–e reveals that cold pools in the PWP-SOIL and DRY-SOIL simulations are, on the whole, substantially stronger than those in the DRENCHED-SOIL, WET-SOIL, and MID-SOIL simulations. The mean values of minimum θ_ρ', maximum v_r, w_{min}, and w_{max} are approximately twice as large (in an absolute-value sense) in the PWP-SOIL and DRY-SOIL simulations as in the other three simulations, and the mean p' value is about three times as large in the PWP-SOIL and DRY-SOIL simulations as in the other three. The larger relative change in p' than in θ_ρ' suggests that the cold pools in the PWP-SOIL and DRY-SOIL simulations are deeper than those in the other three simulations (see Section 2.4.6).

In order to elucidate cold pool structure, Figure 2.7 shows normalized-by-radius composites of the same variables as in Figures 2.6a–e, plotted at t = 0 minutes. These composites confirm the direction of the trend toward increased cold pool strength with decreasing soil

moisture (particularly in the case of the PWP-SOIL and DRY-SOIL simulations). In Figure 2.7a, the values of θ_ρ' are minimized near the cold pool center and increase outward. The largest negative θ_ρ' perturbation occurs in the DRY-SOIL simulation, and the trend holds throughout the interior of the cold pool ($0 \leq r_{\text{norm}} \leq 1$). In the PWP-SOIL and DRY-SOIL simulations, there is a peak in θ_ρ' at $r_{\text{norm}} \approx 1.5$, indicating a ring of enhanced warmth outside the cold pool boundary; this ring is revisited in Section 2.5.2. In Figure 2.7b, v_r peaks inside of the cold pool boundary (at $r_{\text{norm}} < 1$) in all five simulations, and the magnitude of this peak is greatest in the DRY-SOIL simulation. Far outside the cold pool, $v_r < 0$ m s^{-1} due to the residual circulation that generated the parent cloud. The vertical velocities (Figure 2.7c) are negative within the cold pool and positive outside the cold pool, indicative of a parent downdraft and uplift ahead of the gust front, respectively. Downdraft and updraft strengths are both greatest in the DRY-SOIL simulation. Finally, values of p' (Figure 2.7d) are maximized near cold pool center and decay outward, and they are much larger in the PWP-SOIL and DRY-SOIL simulations than in the other three. The extent to which the PWP-SOIL and DRY-SOIL simulations' cold pools are stronger than those of the moister three simulations is exaggerated in Figure 2.7 compared to Figures 2.6a–e. This is because the cold pools in the moister three simulations do not reach their peak intensity until *t* = 5 minutes (not shown). Figures 2.6a–e account for this by considering a range of times relative to *t* = 0 minutes, while Figure 2.7 only shows the *t* = 0 minutes snapshots.

2.4.4 Water Vapor Structure

Figure 2.8a shows the composite near-surface water vapor structure, as a function of r_{norm}, for each of the four simulations at *t* = 0 minutes. The DRENCHED-SOIL, WET-SOIL, and MID-SOIL simulations exhibit the water vapor rings, sometimes referred to as moist patches, that were discussed in Section 2.1. These rings manifest as negative values of

perturbation water vapor mixing ratio, r_v', within the cold pool interiors, followed by positive values of r_v' outside of the cold pool (i.e., at $r_{\text{norm}} > 1$). The PWP-SOIL and DRY-SOIL simulations' composites do not contain a water vapor ring. Instead, each of these composites exhibits a small (~0.2 g kg^{-1}) positive water vapor mixing ratio perturbation—a water vapor "puddle"—that is approximately uniform within the cold pool and decays with increasing distance outside of the cold pool.

As was discussed in Section 2.1, there has been some disagreement as to whether water vapor rings, such as those exhibited by the DRENCHED-SOIL, WET-SOIL, and MID-SOIL simulations, reside inside, along the edges, or outside of cold pools. As Chandra et al. (2018) point out, the location of water vapor rings not only provides clues regarding how the water vapor rings are formed, but also has implications for the triggering of subsequent convection. For example, if water vapor rings are located outside of cold pools, then the thermodynamic and mechanical mechanisms for cold pool triggering of convection may act synergistically. This is potentially the case in the DRENCHED-SOIL, WET-SOIL, and MID-SOIL simulations analyzed here: the water vapor rings (Figure 2.8a) and cold pool-induced updrafts (Figure 2.7c) are both located outside of the cold pools. By contrast, if the water vapor rings are located inside of cold pools, then the local moisture enhancements provided by water vapor rings will not as easily assist in generating new convection because they reside within negatively buoyant air.

Attempts to determine the location of water vapor rings relative to cold pools have been complicated by the use of disparate methods for defining cold pools. Several recent studies (e.g., Dawson et al., 2010; Schiro & Neelin, 2018; Schlemmer & Hohenegger, 2014, 2016) define cold pools in terms of equivalent potential temperature, θ_e, whereas others use temperature- or buoyancy-based metrics (Drager, 2016). Since θ_e has such a strong dependence on moisture, a

water vapor ring that is located along or inside the edge of a cold pool will cause the region of low θ_e associated with the cold pool to be smaller than the corresponding region of low temperature or negative buoyancy (Drager & van den Heever, 2017). It follows that if the water vapor ring's positive influence on θ_e due to enhanced moisture is greater in magnitude than the cold pool's negative influence on θ_e due to low temperatures, then the water vapor ring will *always* occur outside of the θ_e-based cold pool, as is the case in Schlemmer and Hohenegger (2016). This is why both Zuidema et al. (2017) and Chandra et al. (2018) characterize the Schlemmer and Hohenegger (2016) study as exhibiting water vapor rings outside the cold pools when in fact the rings appear to be located inside of the gust front [see, e.g., Figure 6 of Schlemmer and Hohenegger (2016), in which the updrafts—which via continuity are indicative of the gust front—are located along or just outside the edge of the water vapor ring]. More generally, it is difficult to compare water vapor ring results across various studies due to the different metrics used to define cold pool boundaries, and we recommend that comparisons across studies take into account the disparate cold pool definitions.

2.4.5 Equivalent Potential Temperature: A Measure of Cold Pool Strength?

Schlemmer and Hohenegger (2014) propose a cold pool parameterization framework in which the buoyancy term in the equation for cold pool propagation speed (sometimes referred to as cold pool intensity) is replaced by a θ_e deficit term. That is, $-g\frac{\theta_\rho'}{\overline{\theta}_\rho}$, where g denotes acceleration due to gravity, the overbar represents the base state, and the prime represents a deviation from the base state, is replaced by, essentially, $-g\frac{\theta_e'}{\overline{\theta}_e}$ (see Equation 6 of Schlemmer and Hohenegger, 2014). Pucillo et al. (2020) take a similar approach.

The equivalent potential temperature can be an attractive variable to use because it is conserved under moist vapor-liquid pseudoadiabatic processes and therefore contains

information about the height of the source region(s) of cold pool air. There are, of course, uncertainties due to entrainment of environmental air into the downdraft, ice processes, other diabatic processes, and the potential for θ_e to vary non-monotonically with height. Nevertheless, θ_e has often been used to obtain estimates of where downdraft air originates [Schiro and Neelin (2018) and Zuidema et al. (2017) are recent examples of studies that do this]. But is it an appropriate variable to use to define cold pool strength, in a conceptual and/or parameterization framework?

Our results suggest that it may not be. The mean values of minimum θ_e' (Figure 2.6f) exhibit a trend opposite to those of the other five metrics in Figure 2.6: the PWP-SOIL and DRY-SOIL simulations' cold pools exhibit approximately *half* the strength (in a θ_e' sense) of those in the DRENCHED-SOIL and WET-SOIL simulations. The MID-SOIL simulation lies between these two extremes. Recall that the PWP-SOIL and DRY-SOIL simulations' cold pools are roughly *twice* as strong as those in the other three simulations according to the other five, more dynamically-based metrics. In short, dynamical strength does not necessarily translate into θ_e' strength, and θ_e' trends can be misleading.

The equivalent potential temperature also appears to be a problematic metric of cold pool strength from a parameterization perspective. In the DRENCHED-SOIL case, $-g\frac{\theta_e'}{\bar{\theta}_e}$ is approximately three times as large as $-g\frac{\theta_\rho'}{\bar{\theta}_\rho}$ for the average cold pool. By contrast, in the DRY-SOIL case, $-g\frac{\theta_e'}{\bar{\theta}_e}$ is about 20% smaller than $-g\frac{\theta_\rho'}{\bar{\theta}_\rho}$. Therefore, not only do the trends reverse, but the magnitude of the error also differs across the soil moisture regimes examined here.

2.4.6 Cold Pool Depth

Figures 2.9a and 2.9b show composites of θ_ρ' and the transverse circulation at t = 30 minutes for the WET-SOIL and DRY-SOIL simulations. For brevity, the following discussion and corresponding plots consider only the WET-SOIL and DRY-SOIL simulations. It is clear that the cold pools in the DRY-SOIL simulation are, in a composite sense, deeper than those in the WET-SOIL simulation. The ground-based region of negative θ_ρ' extends to a greater height in the DRY-SOIL simulation (~1.75 km) than in the WET-SOIL simulation (~1 km). In addition, the surface-based region of radially outward-directed winds, i.e., the outflow, is deeper in the DRY-SOIL simulation (~1 km) than in the WET-SOIL simulation (~0.5 km). It is not immediately clear why the DRY-SOIL cold pools are deeper than the WET-SOIL cold pools, and indeed, the precise mechanisms governing cold pool depth in these soil moisture sensitivity tests are not fully understood. However, cold pool depth does not typically exceed the depth of the subcloud layer, and since the subcloud layer is deeper in the DRY-SOIL simulation, cold pools are permitted to become deeper as well.

2.5. Cold Pool Processes

2.5.1 Mechanisms Governing Cold Pool Strength and Area

As discussed in Section 2.4.3, the cold pools in the PWP-SOIL and DRY-SOIL simulations are stronger than those in the other three simulations. In order to explain this trend, we now explore the latent cooling that gives rise to the cold pools in the first place. Figures 2.9c and 2.9d show composites of model-derived latent heating and cooling from condensation and evaporation processes for the WET-SOIL and DRY-SOIL simulations. The maximum latent cooling in the subcloud layer occurs at different times (relative to t = 0 minutes) in the WET-SOIL and DRY-SOIL simulations. Therefore, instead of plotting the composites at a particular t-value, we construct these plots by taking the minimum composite value across all t-values from t

= −30 minutes to t = 30 minutes at each point in r-z space. Figure 2.10, which shows composites of cloud mixing ratio r_{cloud} (including cloud water and cloud ice hydrometeor species) in the top row and rain mixing ratio r_{rain} in the bottom row, is generated similarly.

In each of the two bottom panels of Figure 2.9, there are two semi-connected regions of latent cooling, one above cloud base, which corresponds to evaporation of cloud droplets as the cold pools' parent clouds dissipate, and one below cloud base, which corresponds to evaporation of rain drops. The lower regions are of particular interest because evaporation within the rain shaft helps to drive cold pool formation. The lower region of latent cooling is both deeper and greater in magnitude in the DRY-SOIL simulation (Figure 2.9d) than in the WET-SOIL simulation (Figure 2.9c). Therefore, if differences in downdraft vertical velocity and rain shaft lifetime can be neglected, then parcels of air descending below cloud base have a greater residence time in the subcloud layer and undergo greater rates of latent cooling during descent in the DRY-SOIL simulation than in the WET-SOIL simulation.

The rates of latent cooling are governed by both the dryness of the subcloud layer and the properties of the falling rain drops. The dryness of the subcloud layer can be quantified according to the saturation deficit (see Figure 2.2d), which is greater in the DRY-SOIL simulation than in the other three simulations. Increased saturation deficit leads to more evaporation and thus enhanced latent cooling. It is clear from the vertical gradients in r_{precip} in Figure 2.2f and r_{rain} in Figure 2.10c and 2.10d that more evaporation is occurring in the DRY-SOIL simulation, in agreement with the latent cooling differences (Figures 2.9c and 2.9d).

As was discussed in Section 2.4.2, the cold pools in the PWP-SOIL and DRY-SOIL simulations are larger than those in the other three simulations at the initial time of detection. This result appears to be due to the greater width of the rain shafts at cloud base in DRY-SOIL

simulation (compare Figure 2.10d at $z \sim 2.5$ km to Figure 2.10c at $z \sim 1.25$ km), which in turn is due to the wider clouds (compare Figure 2.10b to Figure 2.10a). In other words, wider clouds yield wider rain shafts, which in turn generate initially larger cold pools. Since these larger cold pools are also deeper, with more vertically integrated negative buoyancy through the subcloud layer, they expand more rapidly and thus remain wider. The mechanisms leading to wider clouds in the DRY-SOIL simulation are not obvious. We speculate that this result is due to the increased depth of the subcloud layer (i.e., increased cloud-base height), which can result in wider updraft plumes at cloud base (e.g., Williams & Stanfill, 2002) and thus wider clouds. It was noted in Section 2.2.2 that the cloud fraction is much greater in the PWP-SOIL and DRY-SOIL simulations than in the other three simulations. We conclude that this is the result of both greater numbers of clouds (see Figure A.2a for a sense of this) and greater cloud width.

2.5.2 Mechanisms Governing Cold Pool Structure

As discussed in Section 2.4.4, the cold pools in the DRENCHED-SOIL, WET-SOIL, and MID-SOIL simulations exhibit water vapor rings outside of the cold pools, whereas the cold pools in the PWP-SOIL and DRY-SOIL simulations exhibit water vapor "puddles" within the boundary of the cold pools. It should be noted that some ephemeral water vapor rings are apparent in horizontal cross-sections of r_v in the DRY-SOIL simulation, usually in association with the strongest cold pools (not shown). In contrast to the water vapor rings in the wetter-soil simulations, these DRY-SOIL water vapor rings are located inside of the gust front and appear to disappear quickly via mixing.

The relative lack of water vapor rings in the PWP-SOIL and DRY-SOIL simulations sheds additional light on the mechanisms leading to the formation of water vapor rings discussed in Section 2.1. As was discussed in Section 2.5.1, there is more evaporation of precipitation in

the parent rain shafts of cold pools in the DRY-SOIL simulation than in the WET-SOIL simulation. Since water vapor rings only rarely and fleetingly emerge in the DRY-SOIL simulation, we conclude that rain shaft evaporation alone is not sufficient to generate water vapor rings, as other studies have also suggested (Langhans & Romps, 2015; Schlemmer & Hohenegger, 2016; Torri & Kuang, 2016).

The two other main potential sources of moisture for water vapor rings are surface latent heat fluxes and advection of preexisting moisture perturbations (see Section 2.1). Figures 2.8c and 2.8d show normalized-by-radius composites of surface latent heat flux and sensible heat flux, respectively, at $t = 0$ minutes. It is immediately apparent that the Bowen ratio differs dramatically between the two driest-soil simulations and the other three simulations, with more sensible heat flux and less latent heat flux in the PWP-SOIL and DRY-SOIL simulations than in the other three simulations. With the exception of the latent heat flux in the PWP-SOIL and DRY-SOIL simulations, all surface fluxes are suppressed at cold pool center due to the enhanced static stability (not shown) and the suppressed winds (see Figure 2.7b), as was the case in Grant and van den Heever (2018). Cooler land surface and vegetation temperatures (not shown) generated by cloud shading and interception of cool precipitation also help to suppress the sensible heat fluxes near cold pool center (Drager & van den Heever, 2017). The sensible heat flux composites in the PWP-SOIL and DRY-SOIL simulations, along with the latent heat flux composites in the other three simulations, exhibit local maxima near $r_{\mathrm{norm}} = 1$ (Figures 2.8c and 2.8d) in association with enhanced winds (the gust front; Figure 2.7b). These local maxima become much more pronounced shortly after $t = 0$ minutes as winds increase in strength (not shown).

As was mentioned in Section 2.4.3, there is a ring of enhanced θ_ρ that maximizes in strength near $r_{\text{norm}} = 1.5$ in the PWP-SOIL and DRY-SOIL simulations (Figure 2.7a), and in the other three simulations, there are rings of enhanced r_v near $r_{\text{norm}} = 1.5$ (Figure 2.8a). Prior studies are generally in agreement that latent heat fluxes are important, and possibly of primary importance, for the development of water vapor rings (Langhans & Romps, 2015; Schlemmer & Hohenegger, 2016; Torri & Kuang, 2016). If this is indeed the case, then it is possible that the local latent heat flux maxima at $r_{\text{norm}} = 1$ in the three wettest-soil simulations are associated with the corresponding water vapor rings near $r_{\text{norm}} = 1.5$. It is also possible that the local sensible heat flux maximum at $r_{\text{norm}} = 1$ in the PWP-SOIL and DRY-SOIL simulations is associated with the corresponding ring of enhanced θ_ρ (which can be interpreted as a ring of enhanced temperature given the lack of r_v perturbation) near $r_{\text{norm}} = 1.5$.

Complicating matters are the possible roles of preexisting temperature and r_v perturbations. Figures 2.11a and 2.11b show non-normalized-by-radius composites of T' (perturbation temperature) and r_v', respectively, at $t = -30$ minutes. These correspond to half an hour before each cold pool is detected and are therefore representative of the preexisting perturbations. There is a small but significant positive temperature perturbation near $r = 0$ km in the PWP-SOIL and DRY-SOIL simulations, and there is also a large positive r_v perturbation in the other three simulations. We expect that the influence of the preexisting perturbations may be more fleeting than that of the surface heat fluxes given that the air in which the preexisting perturbations reside should be lifted fairly early in the cold pool lifecycle via cold pool mechanics. Nevertheless, since we have not used tracers or Lagrangian particles in this analysis, we cannot make any definitive statements regarding whether surface heat fluxes or preexisting perturbations are more important.

We now discuss the moisture perturbations near cold pool center, which are positive (moist) in the two driest-soil simulations and negative (dry) in the other three simulations (Figure 2.8a). It is evident from Figure 2.2b that moisture decreases more precipitously with height as soil moisture increases. This implies that, if we consider a hydrometeor-free downdraft originating from cloud base, then such a downdraft would generate a larger negative surface moisture perturbation in the wettest-soil simulations than in the drier-soil simulations. However, in reality, downdraft air contains a source of water vapor in the form of evaporating hydrometeors, and there is more evaporation in the PWP-SOIL and DRY-SOIL simulations (see Section 2.5.1). This evaporation is evidently sufficient to generate a positive surface moisture perturbation in the PWP-SOIL and DRY-SOIL simulations but not in the other three simulations.

2.5.3 Cold Pool Dissipation

Figures 2.11c and 2.11d (t = 5 minutes) corroborate many of the results discussed in Section 2.4 regarding cold pool size and water vapor structure, and they provide a spatial reference for comparison with the bottom row of panels (Figures 2.11e and 2.11f, t = 90 minutes). Figure 2.11e shows that the cold pools in the PWP-SOIL and DRY-SOIL simulations are shorter-lived than those in the other three simulations. In the PWP-SOIL and DRY-SOIL simulations, $T' > 0$ K near $r = 0$ km, indicating that the cold pools in this simulation have dissipated by this time. By contrast, the composite T' is negative in the other three simulations, indicating that the cold pools in these simulations have dissipated more slowly. The composites of r_v' at t = 90 minutes (Figure 2.11f) indicate that water vapor puddles in the two driest-soil simulations dissipate along with their associated cold pools, whereas water vapor rings persist in the wettest-soil simulations beyond the lifetimes of their corresponding cold pools.

Cold pool dissipation need not occur uniformly throughout a cold pool (Grant & van den Heever, 2018). Next we describe two cold pool processes that have been discussed in prior literature that appear to be active in our simulations. First, the wet-patch effect primarily affects the evolution of the central parts of the cold pools. Second, the turbulent mixing effect erodes cold pools from their edges inward.

The wet-patch effect (Drager & van den Heever, 2017), in which fallen precipitation cools the ground and vegetation and suppresses (or even reverses the sign of) sensible heat fluxes, prolongs the cold pool dissipation process within the part of the cold pool that has experienced precipitation. Figure 2.8e shows that less rain water is intercepted by vegetation in the PWP-SOIL and DRY-SOIL simulations than in the other three simulations. This is because the time-integrated rainfall, in a per-cold pool composite sense, decreases with decreasing soil moisture (not shown). It is likely that the increased vegetation-intercepted rain water in the wettest three simulations helps to increase the cold pool longevity in these simulations relative to that in the PWP-SOIL and DRY-SOIL simulations (Drager & van den Heever, 2017).

In a large-eddy simulation of an idealized cold pool in a dry continental environment, Grant and van den Heever (2018) documented cold pool dissipation from the outside inward due to turbulent entrainment of warm environmental air and enhanced (suppressed) sensible heat fluxes near the edge (center) of the cold pool. The PWP-SOIL and DRY-SOIL simulations' cold pools exhibit stronger flows, so they should exhibit greater turbulence at their boundaries. Furthermore, given the greater surface heating in the PWP-SOIL and DRY-SOIL simulations, we can expect that turbulent boundary layer motions are more vigorous overall in this simulation than in the other three simulations. This implies that the outer edges of PWP-SOIL and DRY-SOIL simulations' cold pools are more likely to be eroded by turbulent entrainment. The

identification and tracking algorithm is less successful at locating PWP-SOIL and DRY-SOIL cold pools' edges than at locating those of the cold pools in the other three simulations at times after $t = 0$ minutes (see Figure 2.5b), which is likely due to a combination of ill-defined boundaries—indeed, anecdotally they are "fuzzier" in the DRY-SOIL (see Figure A.1 in the Appendix) and PWP-SOIL simulations—and decreased cold pool longevity.

2.5.4 Role of the Permanent Wilting Point (PWP)

As was discussed in Section 2.2.2, there appear to be three main soil moisture regimes. Each regime has a different partitioning of surface sensible and latent heat fluxes, as determined by the amount of evaporation from the top soil level (a function of the field capacity) and the amount of transpiration by plants (a function of the PWP). The partitioning of surface heat fluxes affects the depth, temperature, moisture, and vigor of circulations in the boundary layer. These affect convection and, by extension, the formation and evolution of cold pools.

Although there are some subtle differences between the MID-SOIL simulation's cold pools and those in the moistest two simulations, which are likely controlled by changes in direct surface evaporation, there appear to only be two main regimes for cold pool properties: moister than the PWP, and drier than the PWP. The fact that the PWP-SOIL simulation (initialized at 45% of saturation, just below the PWP of 45.7%) behaves much more like the DRY-SOIL simulation (25%) than the MID-SOIL (50%) simulation serves to emphasize that there are two well-defined regimes bounded by the PWP.

2.6. Discussion and Conclusion

This study has examined the role of soil moisture in governing tropical continental convective cold pool properties using idealized, high-resolution, cloud-resolving model simulations coupled to an interactive land surface model. Cold pool analyses were performed for

five simulations: DRENCHED-SOIL (initialized at 95% of soil saturation), WET-SOIL (75%), MID-SOIL (50%), PWP-SOIL (45%), and DRY-SOIL (25%). Our hypothesis was that soil moisture has important effects on cold pool size, strength, structure, and longevity. The main findings in this regard, which are summarized in the schematic presented in Figure 2.12, are as follows:

- Decreasing the soil moisture to levels below the permanent wilting point (PWP) yields cold pools that are approximately twice as strong and twice as large, both in area and in depth. Even though direct surface evaporation is present in these simulations, transpiration, which is governed in part by the PWP, appears to be the dominant factor controlling this response. In the PWP-SOIL and DRY-SOIL simulations, the stronger surface sensible heat fluxes create a deeper, drier boundary layer with a higher cloud base. The resulting clouds generate wider rain shafts with greater amounts of rain aloft. Due to the relative dryness of the subcloud layer, more evaporative cooling occurs. Larger, stronger cold pools are therefore able to form.
- Soils moister than the PWP yield a water vapor structure in which (1) near-surface air in the center of the cold pool is relatively dry, and (2) the ring of near-surface air surrounding the cold pool is anomalously moist. The water vapor rings are located outside of the cold pools, ahead of the corresponding gust fronts.
- When soil is drier than the PWP, short-lived "puddles" of moist air fill the cold pools. The air inside the cold pools is approximately uniformly moist, and the air surrounding the cold pools is dry. It is speculated that these features are the result of hydrometeor evaporation within the cold pools' parent rain shafts.

- Cold pools are shorter-lived in the PWP-SOIL and DRY-SOIL simulations than in the other three wetter-soil experiments due to a weaker wet-patch effect (Drager & van den Heever, 2017) and stronger turbulent mixing (Grant & van den Heever, 2018) in the PWP-SOIL and DRY-SOIL simulations.

These results are all modulated by soil moisture-induced changes in the partitioning of surface sensible and latent heat fluxes, which in turn affect boundary layer and cloud properties.

We speculate that the results obtained here are applicable to low-shear continental settings, particularly situations in which both of the following criteria are satisfied: (1) the soil moisture fluctuates above and below the PWP; (2) vegetation is present, such that the PWP becomes relevant; and (3) cumulus congestus clouds form and precipitate regardless of soil moisture content.

The results obtained here regarding cold pool structure and longevity suggest different roles for cold pools in regions with different soil moistures that should be considered in parameterizations of cold pools and convective initiation. Based on the decreased cold pool lifetime in the PWP-SOIL and DRY-SOIL simulations relative to the other three wetter-soil simulations, we can infer that cold pools may suppress convection in their interiors for shorter periods of time in low-soil moisture environments compared to high-soil moisture environments. Furthermore, the co-location of water vapor rings and updrafts in the DRENCHED-SOIL, WET-SOIL, and MID-SOIL simulations, combined with the lack of water vapor rings in the PWP-SOIL and DRY-SOIL simulations, suggests that the thermodynamic mechanism of cold pool-induced triggering of new convection becomes more important as soil moisture increases. Evidently, the relative lack of importance of the thermodynamic triggering mechanism in the PWP-SOIL and DRY-SOIL simulations does not prevent new convection from forming. Indeed,

convection continues later into the evening hours in the PWP-SOIL and DRY-SOIL simulations than in the other three simulations (Figure A.2). Further analysis is required to determine the mechanism(s) responsible for this extension of the diurnal cycle of convection.

Future research should further explore the environmental parameter space, including different initial temperature, moisture, and wind profiles and varying amounts of larger-scale forcing. It would also be useful to consider a variety of vegetation types (including no vegetation) and soil textures. Different environmental conditions may be expected to support different types of convection that could serve as a testbed for the generalizability of the results obtained here. We note that other land-surface schemes treat transpiration and direct surface evaporation in a manner that differs from the one used here. For example, the scheme by Chen and Dudhia (2001) suppresses all direct surface evaporation below the PWP, whereas the LEAF-3 scheme used here does not. Therefore, inter-model comparisons in this regard would be appropriate.

The present study contributes to a growing body of literature on land-surface effects on continental cold pools and highlights the interactions between surface heat fluxes, the boundary layer, and clouds that control cold pool properties. More practically, our results also emphasize the importance of accurately representing initial soil moisture conditions for forecasting cold pools, particularly in regions whose soil moisture content regularly transitions across the PWP. Finally, it is recommended that future cold pool parameterization efforts incorporate the effects of the land surface, such as soil moisture, on cold pools in order to better represent the cold pool dissipation process and time scale.

2.7 Table and Figures

Table 2.1. Details of the RAMS model setup.

Model Aspect	**Settings**
Model version	RAMS version 6.2.08 with LEAF-3 land surface model
Grid	$\Delta x = \Delta y = 125$ m; 150 km × 150 km domain size Δz stretched from 40 m at the surface to 250 m aloft; stretch ratio = 1.025 127 vertical levels; model top at $z \sim 21$ km
Time integration	$\Delta t = 1.5$ s 14 h simulation duration, from 23 UTC (7 LT) to 13 UTC (~21 LT)
Initial conditions	Horizontally homogeneous profiles of temperature and moisture (see smoothed model sounding in Figure 2.1), except for pseudorandom potential temperature perturbations that decrease in amplitude linearly with height from 0.1 K at $z \sim 20$ m to 0 K at $z \sim 520$ m. No initial winds.
Land surface	11 soil levels Silty clay loam soil type Wooded grassland vegetation type Normalized Difference Vegetation Index (NDVI) = 0.6
Initial soil moisture	Spatially uniform value that varies according to the simulation: DRENCHED-SOIL: 95% of saturation volumetric soil moisture (100% = 0.477 m^3 m^{-3}) WET-SOIL: 75% MID-SOIL: 50% PWP-SOIL: 45% DRY-SOIL: 25%
Boundary conditions	Periodic lateral boundaries Rigid lid with Rayleigh friction absorbing layer over the top 2 km
Microphysics	RAMS two-moment bin-emulating bulk microphysics with eight hydrometeor classes, coupled to aerosol module (Meyers et al., 1997; Saleeby & Cotton, 2004, 2008; Saleeby & van den Heever, 2013) Gamma distribution shape parameter equals 4 for cloud and drizzle and 2 for all other hydrometeor classes
Aerosols	Sulfate aerosols (Saleeby & van den Heever, 2013), no sources or sinks, radiatively inactive DeMott et al. (2010) ice nucleation formulation Initial surface concentrations of cloud condensation nuclei (CCN), giant CCN, and ice nuclei (IN) are 400 mg^{-1}, 1×10^{-6} mg^{-1}, and 0.01 mg^{-1}, respectively, decreasing exponentially with altitude with a scale height of 7000 m.
Radiation	Harrington (1997) two-stream radiation scheme, updated every 5 minutes Insolation spatially uniform based on 1–2 August 2010 at Laoag, Philippines.
Turbulence	Smagorinsky (1963) scheme with vertical diffusion modifications based on the formulation of Hill (1974). Vertical diffusion of ice-liquid potential temperature and water vapor mixing ratio is calculated based on perturbations relative to the initial sounding.
Topography	none
Coriolis	none

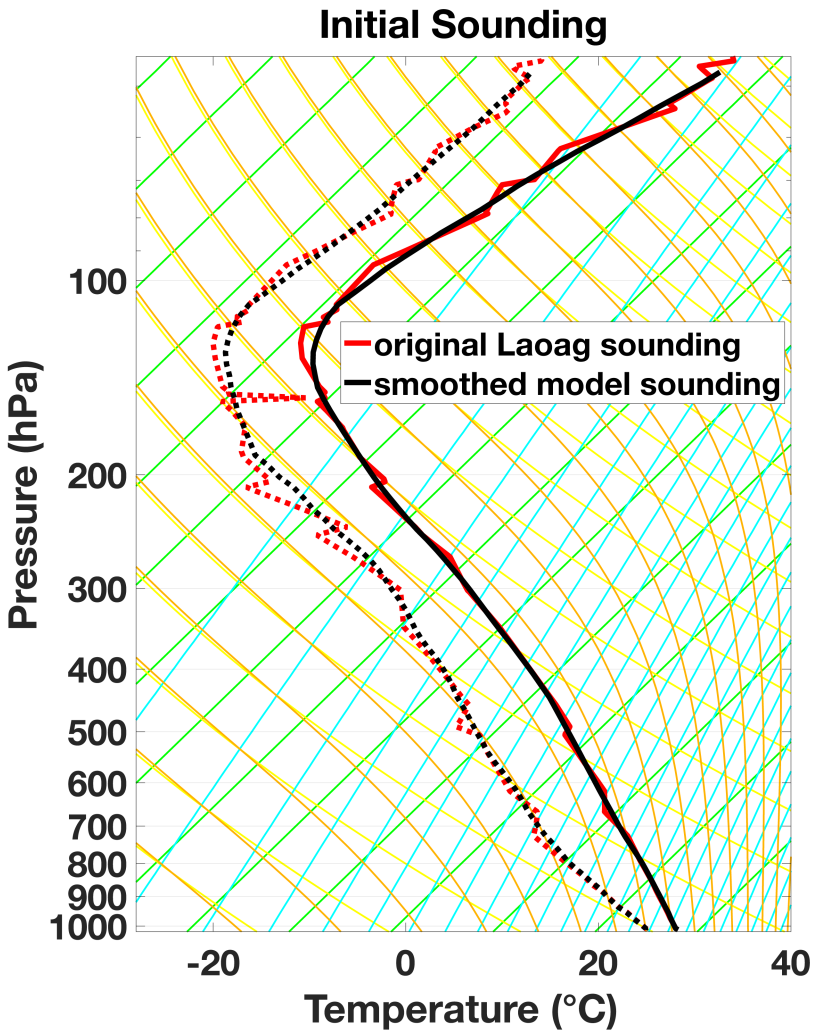

Figure 2.1. Skew$T$ – log$p$ diagram showing the original Laoag sounding and the smoothed model sounding. Thick solid lines indicate temperature, and thick dashed lines indicate dew point. Thin green lines are isotherms, thin cyan lines are lines of constant water vapor mixing ratio, thin yellow lines are dry adiabats, and thin orange lines are moist pseudoadiabats.

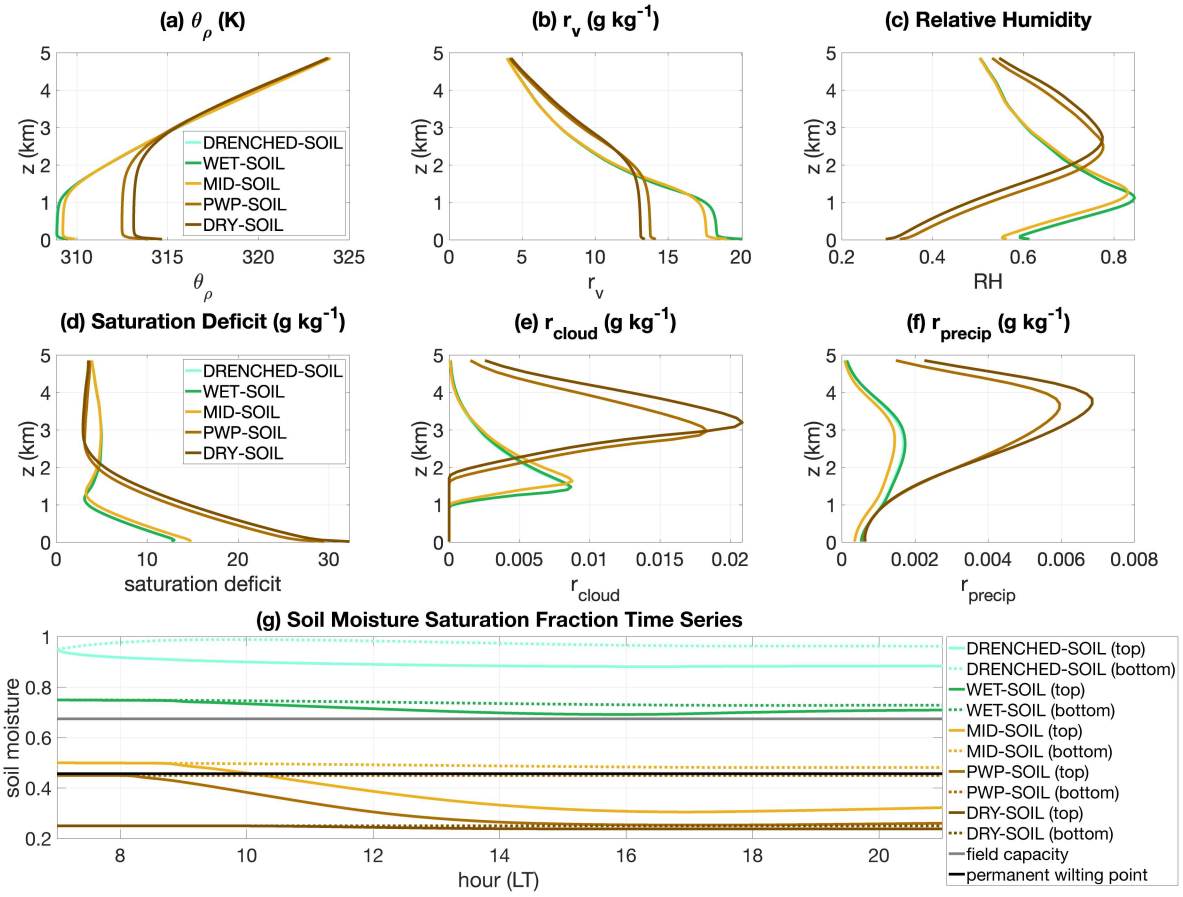

Figure 2.2. Domain-mean vertical profiles (0 – 5 km) averaged over the time period 11:00 LT – 18:00 LT (panels a–f) and time series of soil moisture saturation fraction (panel g). Panel (a) shows the density potential temperature, θ_ρ (as defined by Emanuel, 1994); (b) shows the water vapor mixing ratio, r_v; (c) shows the relative humidity (expressed as a fraction); (d) shows the saturation deficit, defined as the difference between the saturation water vapor mixing ratio and the actual water vapor mixing ratio; (e) shows the sum of cloud water and cloud ice mixing ratios; and (f) shows the sum of the mixing ratios of all other precipitating hydrometeor species. Panel (g) shows the domain-mean soil moisture saturation fraction evolution at the bottom and top soil levels, as well as the field capacity and permanent wilting point (for reference), over the course of the entire simulation.

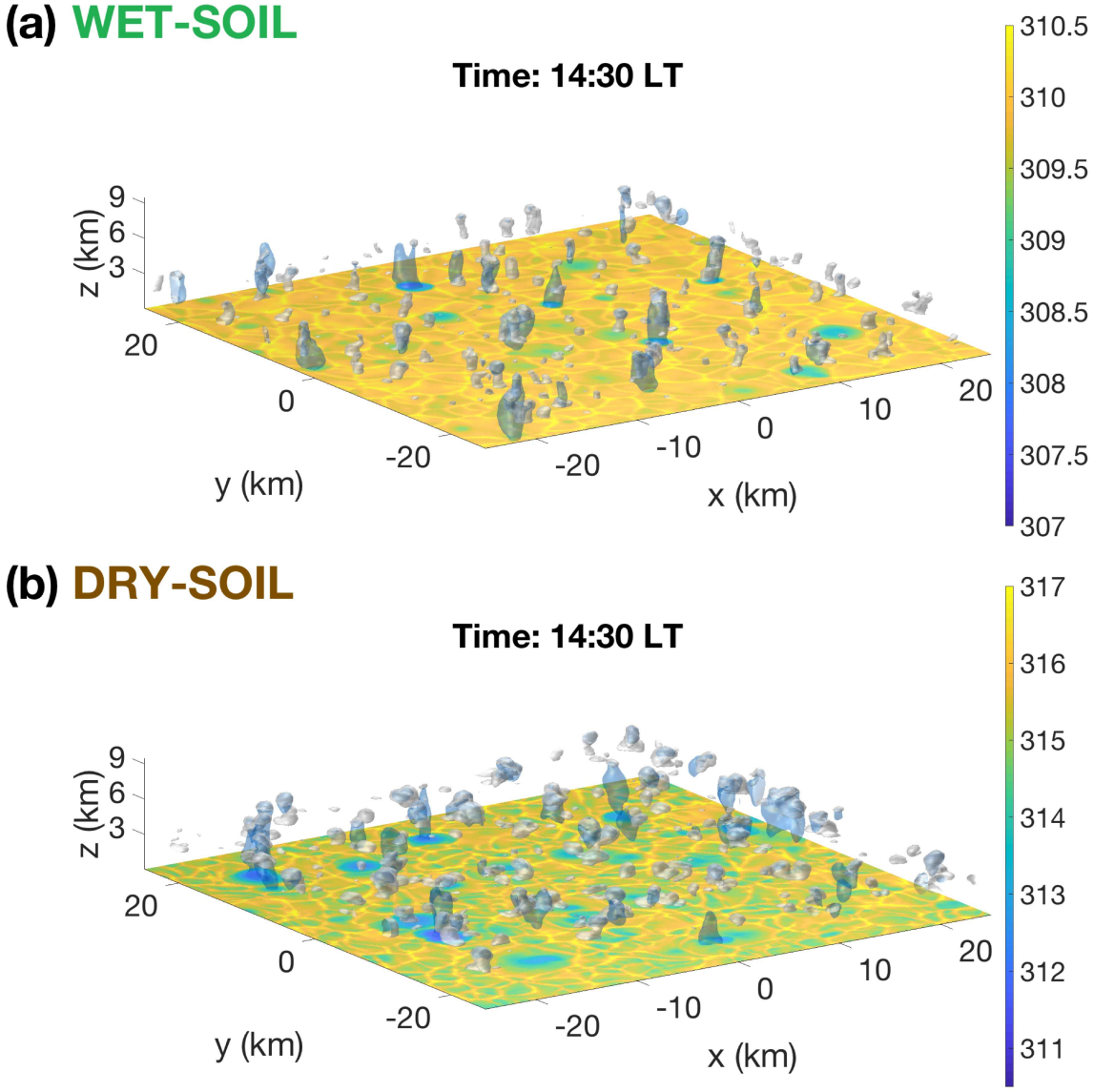

Figure 2.3. Three-dimensional snapshots of the (a) WET-SOIL and (b) DRY-SOIL simulations at 14:30 LT. Only a 50 km × 50 km subset of the domain is displayed here. The 0.1 g kg^{-1} isosurface of the sum of cloud liquid and cloud ice is plotted in white, the 0.1 g kg^{-1} isosurface of the sum of all other precipitating hydrometeor species is shown in blue, and the colors indicate θ_ρ at the lowest above-ground model level, $z \sim 20$ m (note different color scales for WET-SOIL versus DRY-SOIL).

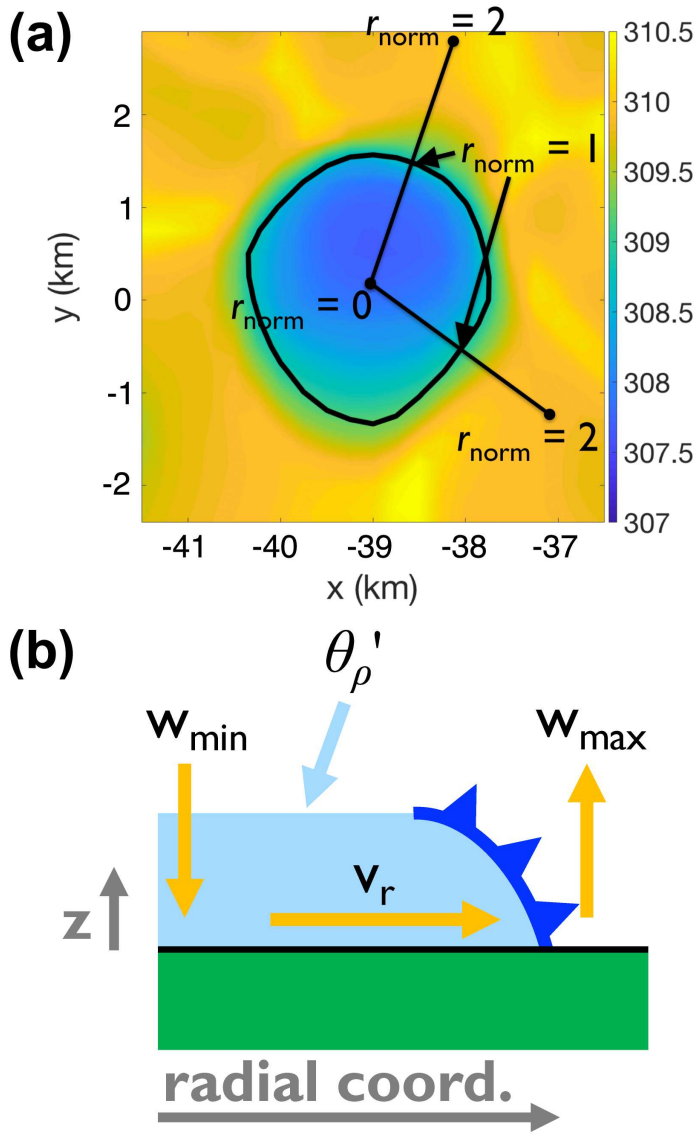

Figure 2.4. (a) Definition of the normalized radial coordinate. A single cold pool from the WET-SOIL simulation at 14:30 LT is used to illustrate the definition of the normalized radial coordinate r_{norm}.The colors indicate θ_ρ (density potential temperature) at the lowest above-ground model level, $z \sim 20$ m, and the black contour indicates the algorithm-derived cold pool boundary. (b) Schematic of various metrics of cold pool strength: density potential temperature perturbation θ_ρ', which is proportional to Archimedean buoyancy; radial outflow strength v_r; w_{min}, the strength of the parent downdraft; and w_{max}, the strength of the uplift at the cold pool boundary. Not shown are equivalent potential temperature perturbation θ_e' and pressure perturbation p', which is related via hydrostatic balance to both θ_ρ' and cold pool depth (and also has some contribution from nonhydrostatic effects). The left edge of the schematic represents the center of the cold pool.

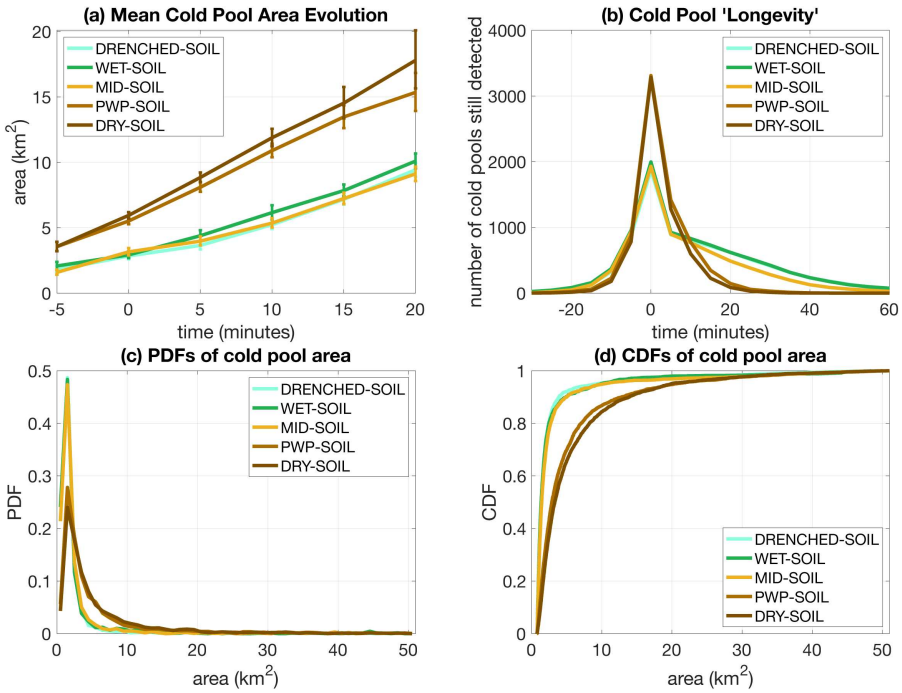

Figure 2.5. Cold pool area statistics. Panel (a) shows the time evolution of mean cold pool area relative to the $t = 0$ minutes reference time based on contours obtained during the final tracking step (see Section A.1 in the Appendix), along with 95% confidence intervals for the mean (constructed using a bootstrapping approach). For each time (relative to $t = 0$ minutes), only those cold pools whose boundaries can be identified are included. Only $t = -5$ minutes through $t = 20$ minutes is shown due to relatively small sample sizes at earlier and later times. Panel (b) (note different horizontal axis) shows the sample sizes for (a), i.e., the numbers of cold pools that can be tracked backward and forward to each time relative to the $t = 0$ minutes reference time, for the entire range $t = -30$ minutes through $t = 60$ minutes. Panels (c) and (d) show the probability density functions and cumulative density functions, respectively, at $t = 0$ minutes (when all cold pools in the data set are included).

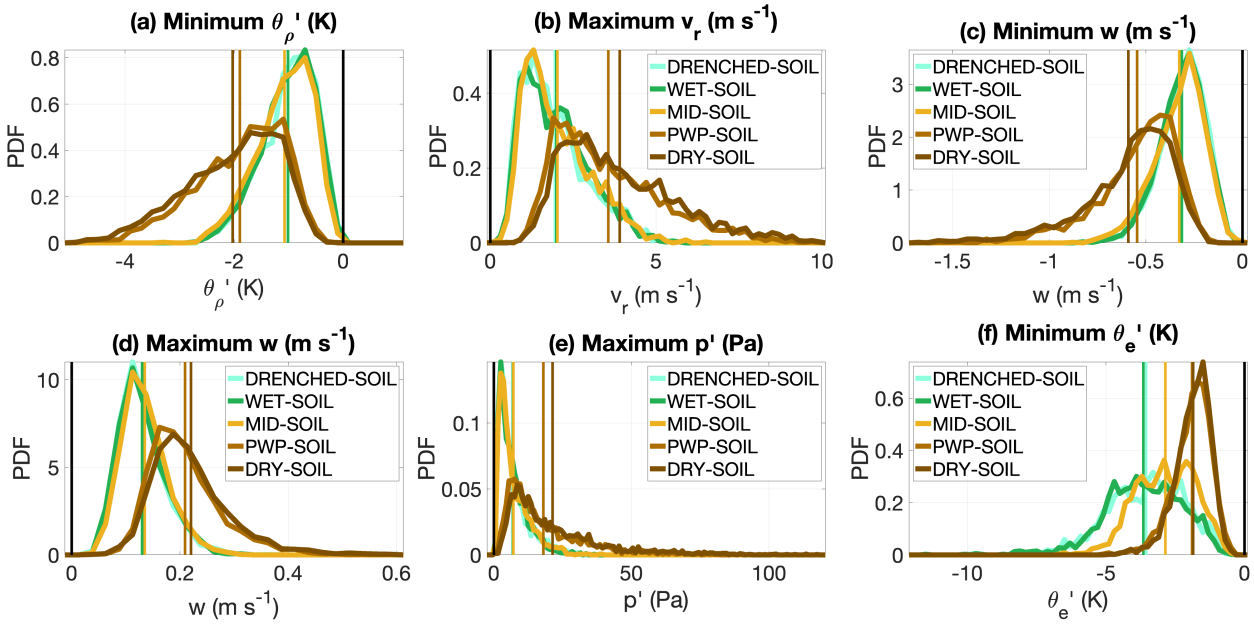

Figure 2.6. Cold pool strength statistics. The thick curves show the PDFs for the various variables, and the vertical lines show the mean values across the entire sample of cold pools (black vertical lines are plotted at zero for reference). The plotted variables are (a) minimum θ_ρ'; (b) maximum v_r; (c) minimum vertical velocity, w; (d) maximum w; (e) maximum p'; and (f) minimum θ_e'. All perturbation quantities are computed relative to a time-varying horizontal domain mean. All panels are plotted at the lowest above-ground model level [$z \sim 20$ m for panels (a), (b), (e), and (f), and $z = 40$ m for panels (c) and (d)]. Each data point included in the PDFs and means is taken from a single cold pool and is the maximum or minimum value of some azimuthally averaged quantity within some radius band (see Section 2.4.3 of the text for details).

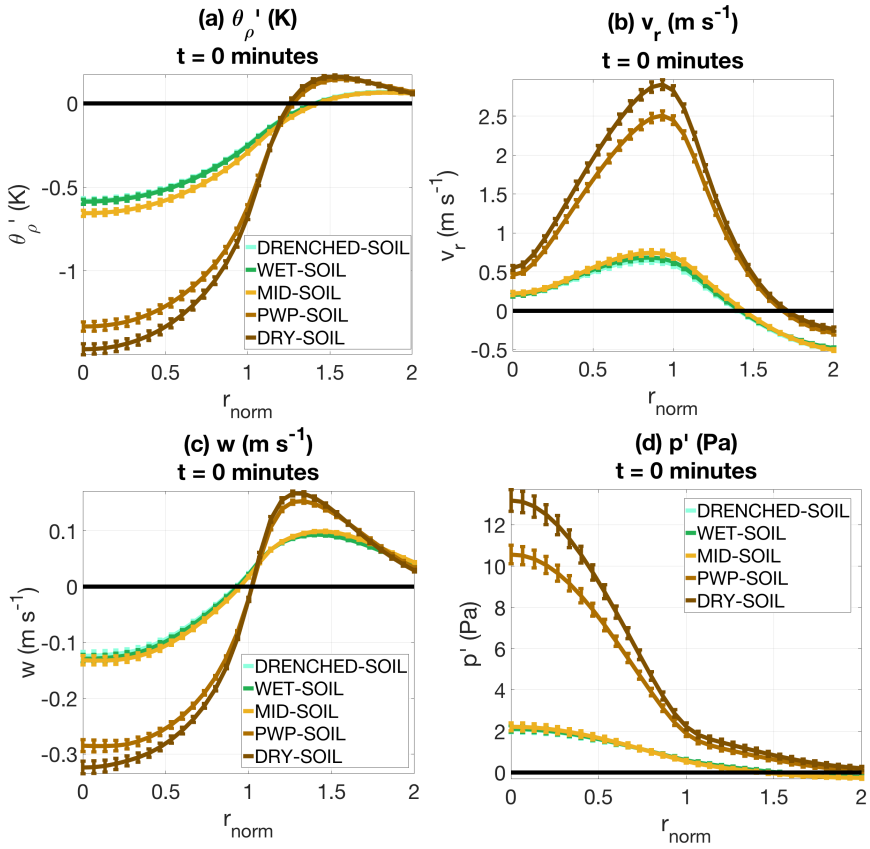

Figure 2.7. Near-surface normalized composites of (a) θ_ρ', (b) v_r, (c) w, and (d) p' at $t = 0$ minutes. Panels (a), (b), and (d) are plotted for $z \sim 20$ m, and panel (c) is plotted for $z = 40$ m. Error bars indicate the 95% confidence interval for the mean, based on a bootstrapping approach.

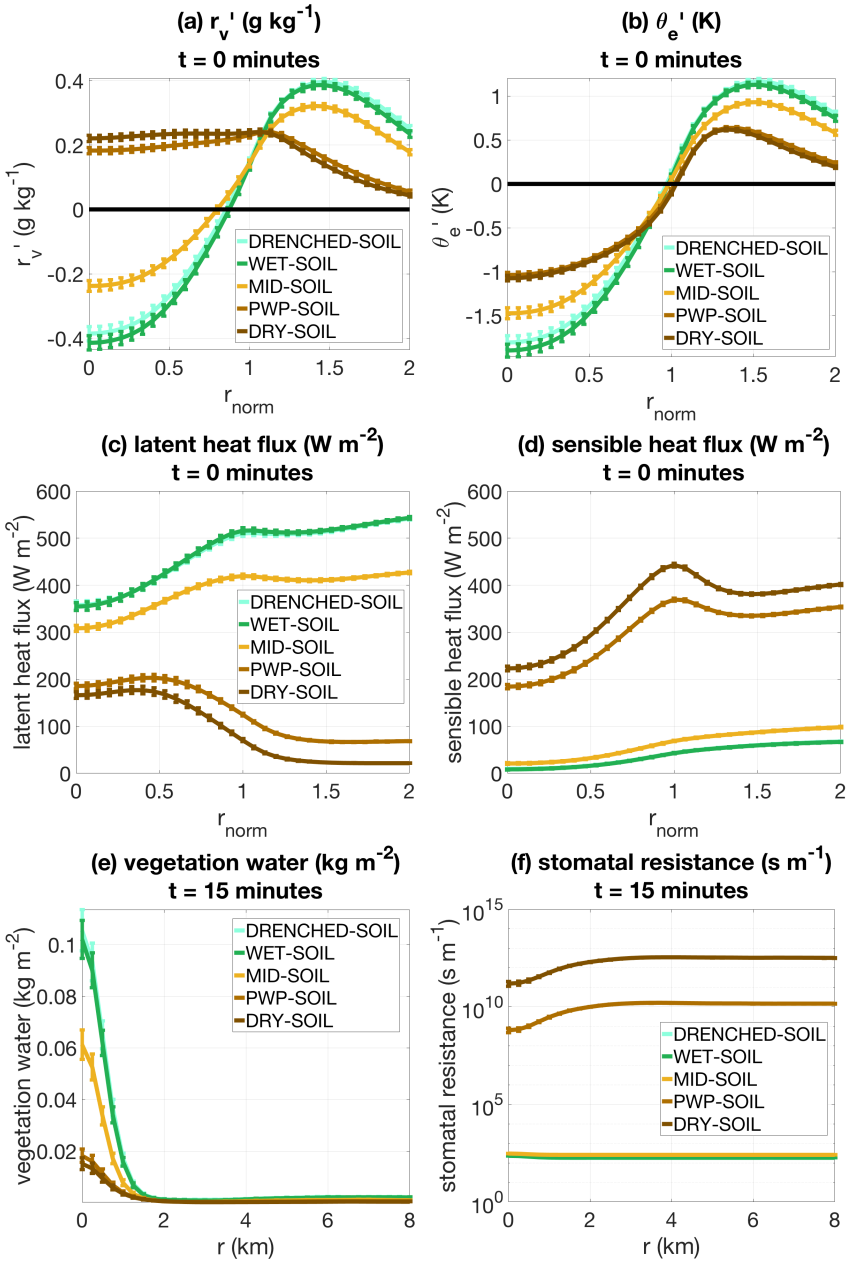

Figure 2.8. Surface and near-surface normalized composites at $t = 0$ minutes (a–d) and non-normalized composites at $t = 15$ minutes (e–f). The plotted variables are: (a) r_v', (b) θ_e', (c) surface latent heat flux, (d) surface sensible heat flux, (e) vegetation water (rain intercepted by and collecting on leaves), and (f) stomatal resistance (note logarithmic vertical axis). Panels (a) and (b) are plotted for $z \sim 20$ m and are computed relative to a time-varying horizontal domain mean, while all other variables are surface quantities.

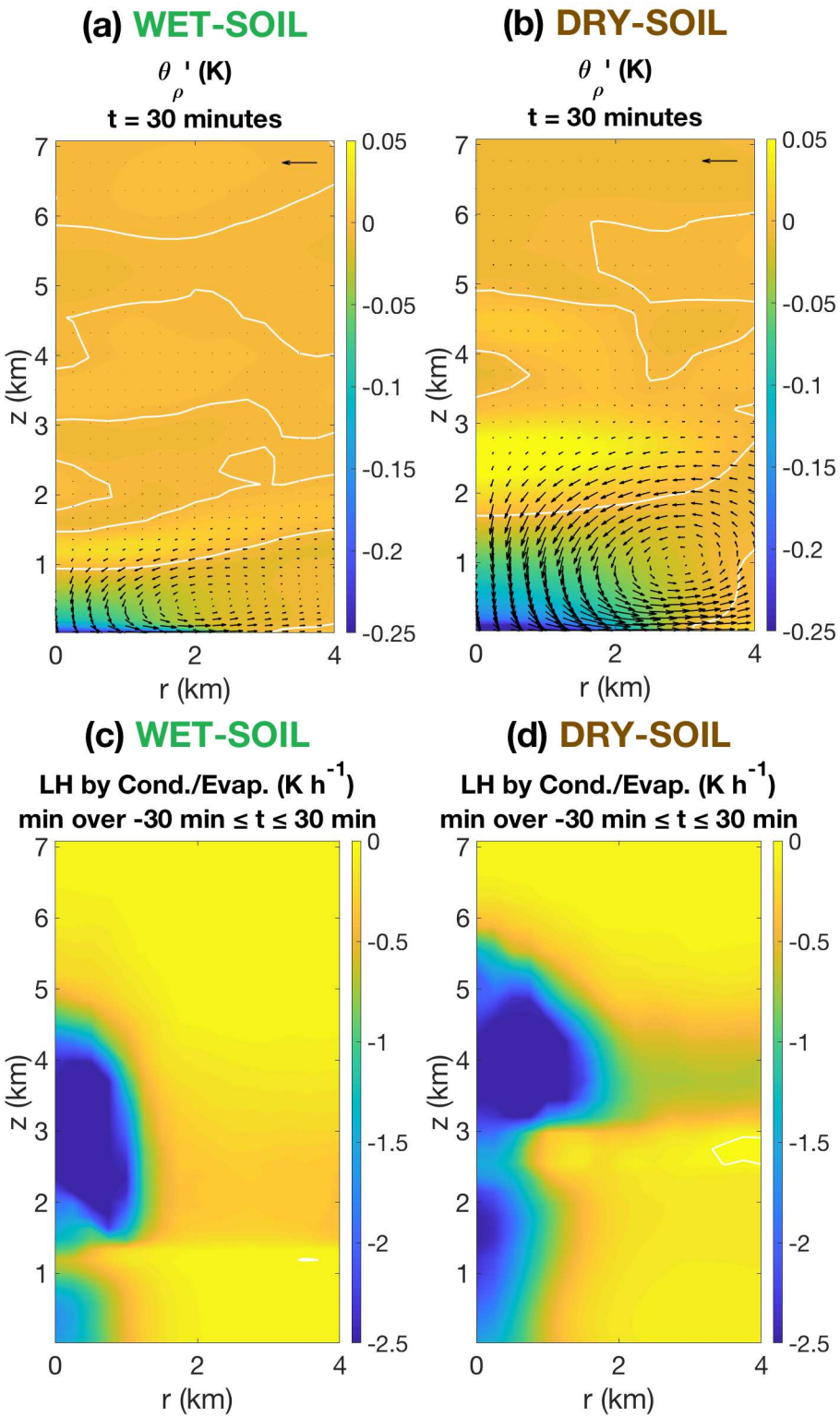

Figure 2.9. Panels (a)–(b) show composite (non-normalized) radius-height cross-sections of θ_ρ' at t = 30 minutes. White curves are the zero-contours, and black arrows are the composite wind vectors in the r-z plane. The arrow in the upper-right corner of each of these panels has a magnitude of 1 m s^{-1}. In order to conserve storage space on local machines during the analysis

process, only one-fourth (one-eighth) of the WET-SOIL (DRY-SOIL) cold pools, evenly distributed across time and space (~400–500 cold pools in both cases), are included in all radius-height composites, and the data at even-numbered vertical levels are not plotted. Panel (a) shows the WET-SOIL composite and panel (b) shows the DRY-SOIL composite. Panels (c) and (d) show (non-normalized) radius-height cross-sections of latent heating and cooling rates from evaporation and condensation (outputted by the model as five-minute averages) in the WET-SOIL and DRY-SOIL simulations, respectively. The specific method for generating the plots is described in the text. White curves are zero-contours.

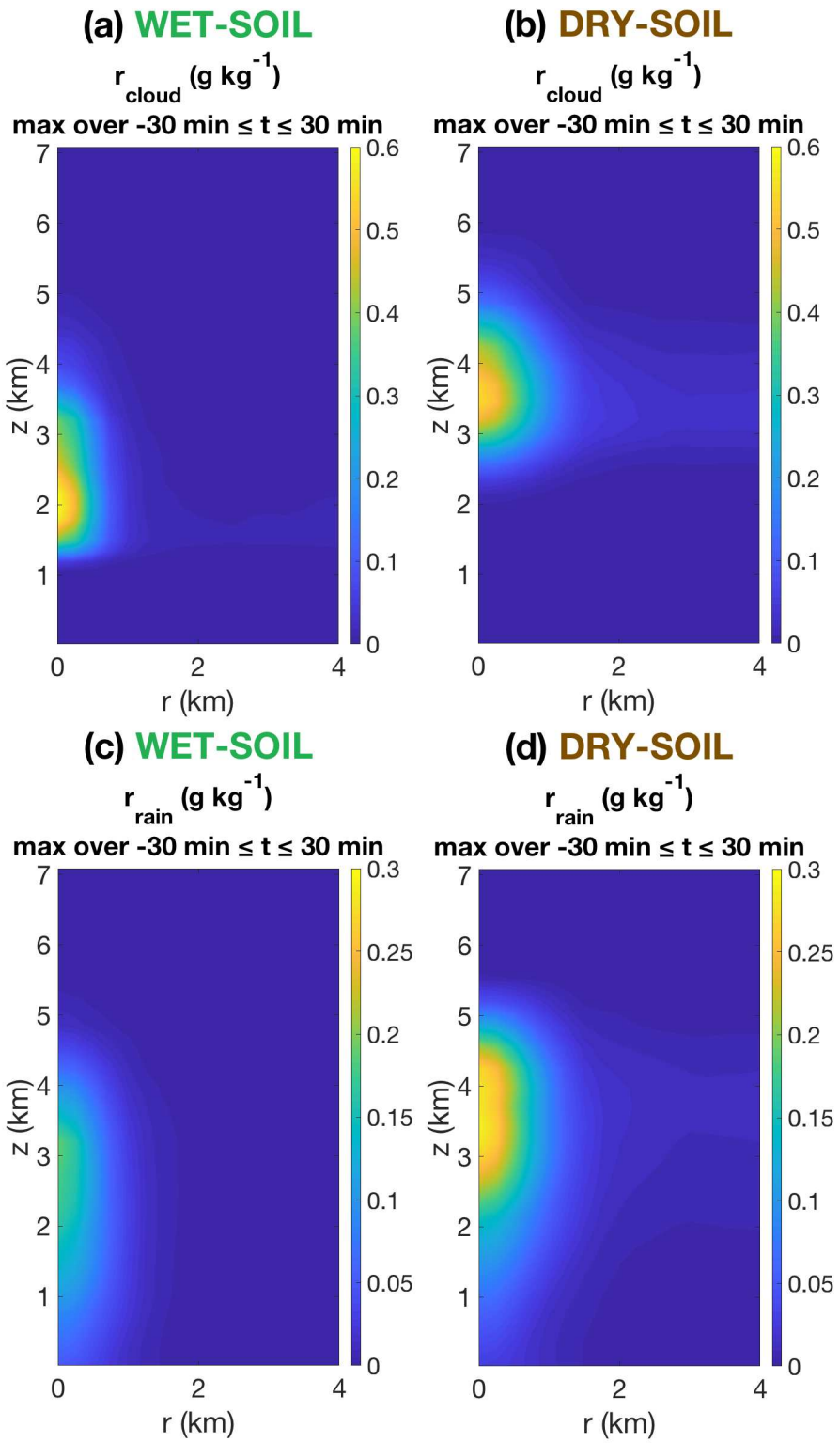

Figure 2.10. As in Figures 2.9c and 2.9d, but for the time-maximum composite cloud mixing ratio (sum of cloud liquid and cloud ice) (panels a and b) and for the time-maximum composite rain water mixing ratio (panels c and d).

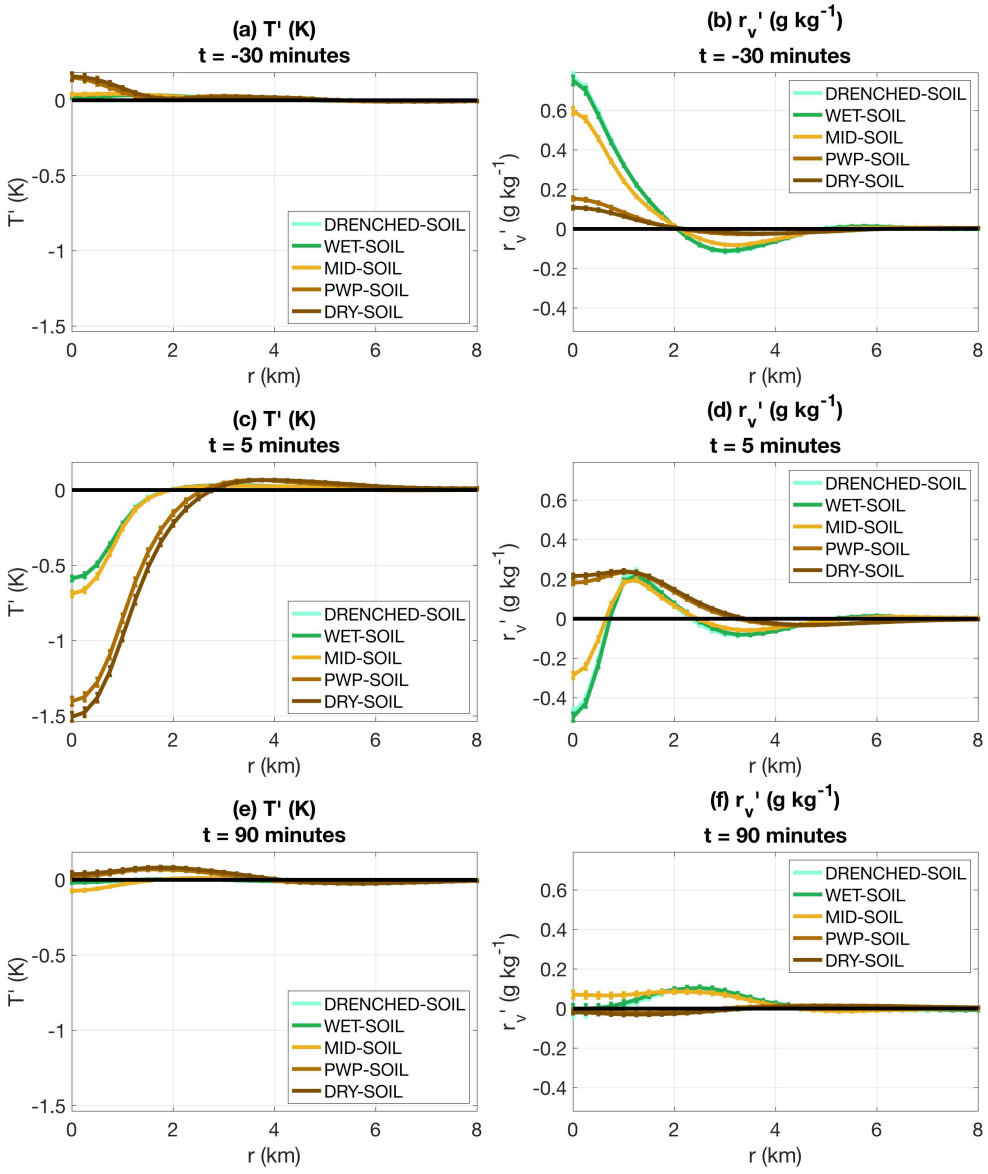

Figure 2.11. Time evolution of non-normalized composites of temperature perturbation T' (panels a, c, and e) and r_v' (panels b, d, and f). The times plotted are $t = -30$ minutes (panels a and b), $t = 5$ minutes (panels c and d), and $t = 90$ minutes (panels e and f).

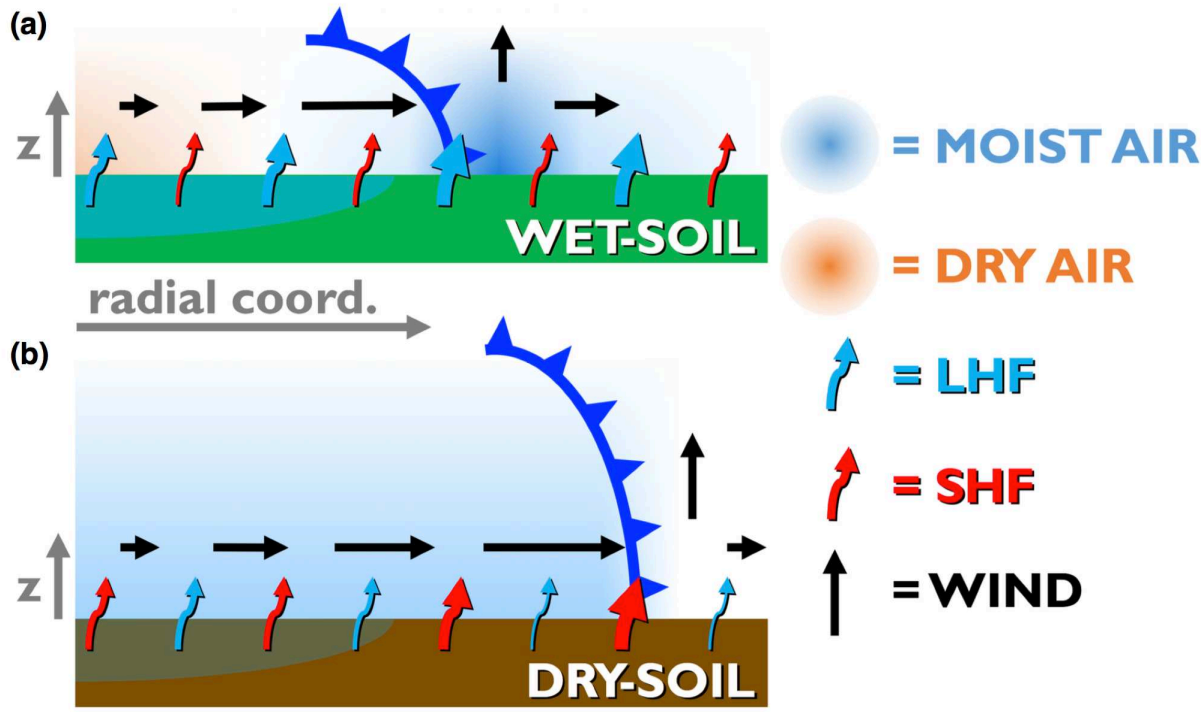

Figure 2.12. Summary schematic. Panel (a) represents the WET-SOIL simulation (but also applies for the DRENCHED-SOIL and MID-SOIL simulations), and panel (b) represents the DRY-SOIL simulation (but also applies to the PWP-SOIL simulation). Both diagrams are vertical cross-sections in the *r*-*z* plane, with the left edge of each diagram corresponding to $r = 0$ km. The blue flags (cold front symbol) represent the cold pool boundary. The blue and orange above-ground shading represent the perturbation water vapor mixing ratio (orange = drier than domain mean, blue = more humid than domain mean). The black arrows depict the most relevant aspects of the wind field in the *r*-*z* plane (stronger wind = longer arrow). The light blue arrows represent the surface latent heat fluxes (LHFs), and the red arrows represent the surface sensible heat fluxes (SHFs). Stronger fluxes are indicated by thicker arrows. Finally, the light blue below-ground shading represents the location of the wet patch (Drager & van den Heever, 2017), where the soil and vegetation have been soaked by cool rain water.

CHAPTER 3: LESS PORRIDGE FOR GOLDILOCKS: AN INTERMEDIATE-SOIL MOISTURE DISADVANTAGE IN AFTERNOON PRECIPITATION MODULATED BY VEGETATION

3.1 Introduction

In Earth's climate system, soil moisture and precipitation are inextricably linked as part of a broader global hydrologic cycle (Rodell et al., 2015). The coupling between soil moisture and precipitation exhibits multiple layers of complexity. At the simplest level, water escapes from the soil into the atmosphere via evapotranspiration (combined transpiration by plants and evaporation of liquid water from the soil surface) (Hillel, 2003). Once in the atmosphere, it is able eventually to condense and return to the soil in the form of precipitation (Eltahir & Bras, 1996; Hillel, 2003). However, the fact that moisture is recycled between the soil and atmosphere does not necessarily guarantee that increases in soil moisture will yield local enhancements in precipitation. Indeed, multiple studies over the past several decades have identified scenarios in which the atmosphere produces more local rainfall over dry soils than over wet soils (e.g., Giorgi et al., 1996; Taylor et al., 2012), as well as scenarios in which the reverse is true (e.g., Findell et al., 2011; Findell & Eltahir, 1997).

The processes governing the response of rainfall to soil moisture, such as boundary layer growth and the development of convective clouds, are not explicitly represented in most coarse global models (Randall et al., 2003). Instead, both weather forecasts and climate predictions rely on parameterizations that are designed to capture the essential aspects of the various processes while remaining computationally efficient. The limitations of these parameterizations, such as their difficulty reproducing the observed diurnal cycle of precipitation (Baranowski et al., 2018; Dirmeyer et al., 2012; Rio et al., 2009), are well documented and highlight the need for

improved process-level understanding. Enhanced process-level understanding of the soil moisture-precipitation relationship will not only improve confidence in model projections of conditions such as drought, but also enable the formulation of strategies for optimizing the efficiency of agricultural practices such as irrigation (Lawston, 2017).

As mentioned above, previous studies have identified both "wet-soil advantage" and "dry-soil advantage" regimes with respect to precipitation. Soil moisture controls the amount of water available for transpiration by plants and evaporation of liquid water from the soil surface, together termed evapotranspiration (Stull, 1988). For a given amount of incoming solar radiation (hereafter *insolation*), and for a given amount of heat flux into the ground, surface energy balance requires that increases in evapotranspiration (latent heat fluxes) be accompanied by compensating decreases in sensible heat fluxes (Stull, 1988). When the soil is dry, evapotranspiration is suppressed, and insolation results in substantial daytime warming of the uppermost layer of soil, which in turn supports strong sensible heat fluxes into the atmosphere (Stull, 1988).

In the context of disorganized afternoon boundary layer cumulus clouds, which are the focus of the present study, wet soil can favor production of precipitation by such clouds by inducing strong latent heat fluxes that inject water vapor into the boundary layer. As water vapor accumulates, the level of free convection descends below the top of the boundary layer, and the boundary layer circulations can then result in convective cloud formation (Findell & Eltahir, 2003a). Wet soil is most likely to favor precipitation under conditions of high free tropospheric stability, which suppresses boundary layer growth and thus supports the required accumulation of water vapor in the boundary layer (Ek & Holtslag, 2004; Ek & Mahrt, 1994; Findell & Eltahir, 2003a; Gentine et al., 2013). On the other hand, the sensible heat fluxes associated with dry soil

generate static instability within the boundary layer that spurs rapid boundary layer growth and strong boundary layer circulations that are able to ascend to the level of free convection (Ek & Holtslag, 2004). A dry-soil advantage regime is most likely to occur when the early morning lower troposphere is moist and exhibits relatively low static stability (Ek & Holtslag, 2004; Findell & Eltahir, 2003a; Gentine et al., 2013).

Findell and Eltahir (2003a) propose a quantitative framework for predicting whether a wet-soil or dry-soil advantage is most likely, based on the properties of the early morning (~6:00 LT) vertical profiles of temperature and humidity. Specifically, they introduce a convective triggering potential (CTP) and a low-level humidity index (HI_{low}). Under this framework, it is possible to map the location of a given sounding in CTP-HI_{low} space to one of three possible outcomes each for wet and dry soils: no convection, non-precipitating shallow convection, or precipitating deep convection. No predictions are made about the precise amount of rainfall. A wet-soil advantage is said to occur when, according to the framework, wet soils are expected to produce deep convection and dry soils are not, or when wet soils are expected to produce shallow convection and dry soils are expected to produce no convection. A dry-soil advantage occurs under opposite conditions.

The wet-soil and dry-soil advantage regimes discussed above relate primarily to the "temporal" perspective of the soil moisture-precipitation relationship, which considers whether days with relatively wet soil experience more or less precipitation (or, in some studies, earlier or later onset of precipitation) than do days with relatively dry soil (Findell et al., 2011). This approach contrasts with the "spatial" perspective, which concerns local heterogeneities in soil moisture and their relationship to the locations where rain falls (Taylor et al., 2012). Both perspectives are important, and a recent study (Guillod et al., 2015) has proposed an elegant

unification of the two. Nevertheless, for purposes of the present work, the temporal approach is of primary interest, and spatial heterogeneities in soil moisture are not considered.

Previous studies have used several different approaches to investigating soil moisture-precipitation interactions. These include analytic and simple numerical models (e.g., Findell & Eltahir, 2003a; Gentine et al., 2013); one-dimensional models (e.g., Ek & Mahrt, 1994); global and regional Earth system models with parameterized convection and land surfaces (e.g., Hohenegger et al., 2009; Koster et al., 2004); regional convection-permitting model simulations, in which convective motions begin to be resolved (e.g., Hohenegger et al., 2009); and high-resolution large-eddy simulations, in which convective clouds are resolved and turbulent eddies begin to be resolved (Chlond et al., 2014; Cioni & Hohenegger, 2017; Drager et al., 2020; Kang, 2016; Kristianti et al., 2018). Even though regional convection-permitting simulations and high-resolution large-eddy simulations resolve various aspects of convection to differing degrees, all of these models still parameterize the land-atmosphere interactions. The ubiquity of such parameterizations across scales further highlights the need to better understand these interactions. Observational work assessing statistical relationships between soil moisture and precipitation has also been successfully performed (e.g., Findell & Eltahir, 1997; Ford et al., 2015; Yuan et al., 2020). While observational studies are critical for evaluating the physical processes involved, one important limitation inherent to observational work is that it is impossible to conduct controlled experiments in which only one parameter (e.g., soil moisture) is changed at a time. As a result, inferring causality is not straightforward (Santanello et al., 2017; Tuttle & Salvucci, 2016). Another limitation is that key physical parameters, such as soil texture and soil moisture, are heterogeneous and difficult to measure (Mohanty & Zhu, 2007), and even when measurements are available, there is no guarantee that they will be representative of their

surroundings (Nicolai-Shaw et al., 2015). By contrast, while there certainly exist shortfalls in numerical models' parameterizations, one strength of such models is that they provide a complete spatiotemporal record of the events being simulated, and model-derived process rates allow diagnosis of physical mechanisms.

The present investigation, therefore, is conducted using an idealized numerical modeling approach. In this approach, the problem of interest is simplified to its bare essence so as to remove complicating factors and confounding variables. The initial conditions are horizontally homogeneous, there is only a single soil texture and vegetation type in each simulation, and there is no topography. Coriolis acceleration is also omitted, and the diurnal cycle of insolation is spatially uniform. The lateral boundaries of the perfectly square domain are periodic. This contrasts with case-study modeling based on observed events, in which spatial heterogeneity complicates attempts to attribute precipitation events to the specific soil moisture levels or patterns. Case studies are useful because they can be used both to shed light on mechanisms governing observed events and to evaluate models using observations. However, we have chosen to use idealized modeling because such an approach minimizes complexity in order to maximize interpretability.

Two recent studies (Drager et al., 2020; Hohenegger & Stevens, 2018) have drawn attention to a particular threshold in soil moisture-convection interactions: the permanent wilting point (PWP). The PWP is, for a given soil texture, the level of soil moisture below which typical plants' roots are unable to remove any liquid water from the soil (e.g., Hillel, 2003). Soils drier than the PWP hold onto their water too tightly for root uptake of water, and as a result, transpiration by plants shuts down. Hohenegger and Stevens (2018) found using idealized convection-permitting modeling that spatial differences in soil moisture, where one region is

moister than the PWP and an adjacent region is drier, induce a moist region-to-dry region flow that initiates convection over the dry region. It was found in the large-eddy simulations of Drager et al. (2020) that as the initialization soil moisture decreases to levels below the PWP, the character of convective cold pools (Drager & van den Heever, 2017) changes abruptly and dramatically. However, this study did not probe surface rainfall accumulations. In further examining the simulations of Drager et al. (2020), we have found that the amount of domain-mean accumulated precipitation is substantially lower for initialization soil moistures that are just above the PWP than for very moist or very dry soils. The present work seeks to examine this non-monotonic soil moisture-precipitation relationship. In general, most previous high-resolution numerical modeling studies examining the soil moisture-precipitation relationship have not directly examined trends in accumulated precipitation as a function of soil moisture relative to the PWP. Some have used an idealized setup but examined only soil moistures above the PWP (Cioni & Hohenegger, 2017; Kristianti et al., 2018). Chlond et al. (2014) do sample below the PWP but only simulates non-precipitating cumulus, and Kang (2016) does not use a realistic soil parameterization, instead opting to specify the ratio of sensible to latent heat fluxes (the "Bowen ratio"). Others have used a case-study setup in which the initial soil moisture is nonuniform such that behavior near the PWP threshold cannot be assessed directly (e.g., Barthlott & Kalthoff, 2011; Hohenegger et al., 2009).

In light of the findings and limitations of previous work, the present study is guided by the following question: How does the permanent wilting point modulate the precipitation response to changes in soil moisture, and how does this modulation depend on the characteristics of the land surface? Based on results from the simulations performed in Drager et al. (2020), the examination of which served as the impetus for the present work, a decrease in precipitation is

expected for soils just slightly moister than the PWP. But what physical processes drive this trend in precipitation? Furthermore, Drager et al. (2020) examine only a single soil texture and land covering type, with five initial soil moistures. The present study seeks to sample the soil texture, land cover, and soil moisture parameter space more comprehensively in order to elucidate the physical mechanisms behind the described precipitation response.

3.2 Materials and Methods

High-resolution, cloud-resolving model simulations are performed using the open-source Regional Atmospheric Modeling System (RAMS), version 6.2.10 (Cotton et al., 2003; Saleeby & van den Heever, 2013), which is fully coupled to the Land Ecosystem–Atmosphere Feedback, version 3 (LEAF-3) soil–vegetation–atmosphere transfer scheme (Lee, 1992; Walko et al., 2000). The LEAF-3 scheme uses a modified big-leaf framework in which a layer of vegetation—when vegetation is present—covers the entire surface. A layer of canopy air exists in which vegetation is embedded, and there are distinct vegetation temperatures and canopy air temperatures. LEAF-3 also contains a soil model with a user-specified number of soil layers, each with its own volumetric soil moisture and temperature. Fluxes of sensible and latent heat are parameterized using a voltage-resistance approach. Direct surface evaporation follows the RAMS Technical Manual (Mission Research Corporation, 1997), and transpiration follows Lee (1992). Under vegetated scenarios, transpiration is controlled by a stomatal resistance that responds to temperature, insolation, and water stress, and at any given time step and location, it extracts water from whichever soil layer in the root zone has the greatest soil water potential.

All simulations have been conducted using the Navy Department of Defense Supercomputing Resource Center Cray XC40 system *Conrad*. As in Cioni and Hohenegger (2017), the horizontal grid spacing of the numerical experiments is 250 m, and the horizontal

dimensions of each simulation's domain are 100 km × 100 km. The lateral boundary conditions are periodic. The vertical grid spacing increases from 40 m near the surface to 250 m aloft with a stretch ratio of 1.025 and a total of 127 vertical levels. Each simulation is run from 7:00 LT to 21:00 LT, so as to capture a single afternoon convection event. The LEAF-3 land surface is configured with 11 soil layers extending to a depth of 0.5 m, and the initial soil temperatures are slightly warmer than the lowest level of the atmosphere, following Drager et al. (2020) and Grant and van den Heever, (2014).

This research is undertaken in conjunction with the Office of Naval Research's Propagation of IntraSeasonal Tropical OscillatioNs (PISTON) field campaign, one of whose goals is improve our understanding land-ocean-atmosphere interactions over the Philippine archipelago (Office of Naval Research, 2016). Simulations are initialized with a modified morning sounding from the Laoag site on the island of Luzon in the Philippines, and the initial state is horizontally homogeneous except for pseudorandom thermal perturbations in the lowest ~520 m of the atmosphere, following Drager et al. (2020). Initial winds are calm. When the methods of Findell and Eltahir, (2003a) are applied to the initial sounding, values of CTP = 204 J kg^{-1} and HI_{low} = 10.6 K are obtained. According to this framework, these indices place the sounding in dry-soil advantage regime but near a transition zone (in the CTP-HI_{low} plane) between wet soil-advantage and dry soil-advantage regimes.

Other aspects of the model setup are identical to those in Drager et al. (2020). Of these, we note that the RAMS two-moment, bin-emulating microphysics scheme with eight hydrometeor classes is used (Meyers et al., 1997; Saleeby & Cotton, 2004, 2008; Saleeby & van den Heever, 2013). The LEAF-3 scheme has sophisticated interactions with the microphysics scheme. Precipitation is allowed to be intercepted by leaves, and the internal energy of falling

hydrometeors is able to influence the temperature of the surface. Furthermore, precipitation replenishes the soil moisture. We also employ the two-stream radiative transfer scheme of (Harrington, 1997), with radiative fluxes and heating rates updated every 300 seconds, as well as a modified form of the Smagorinsky turbulence parameterization (Drager et al., 2020; Hill, 1974; Smagorinsky, 1963). There is no topography or Coriolis acceleration.

We perform forty simulations, each representing a unique combination of soil type (silty clay loam or clay loam), land cover type (bare soil or wooded grassland), and soil moisture (25%, 40%, 45%, 50%, 55%, 60%, 65%, 70%, 75%, or 95% of soil saturation). Wooded grassland occupies much of Luzon, and bare soil is tested in order to assess the role of vegetation. The soil moisture values are chosen in order to examine the entire soil moisture spectrum, from very dry to very moist, and a fine soil moisture interval of 5% is used over 40% to 75% in order to provide high "resolution" for soil moistures ranging from just below the permanent wilting point to just above the field capacity. Silty clay loam and clay loam are chosen because, as formulated in LEAF-3, they have similar saturation values of volumetric soil moisture (0.477 $m^3\ m^{-3}$ and 0.476 $m^3\ m^{-3}$, respectively) and field capacity (0.322 $m^3\ m^{-3}$ and 0.325 $m^3\ m^{-3}$, respectively) but substantially different permanent wilting points (0.218 $m^3\ m^{-3}$ and 0.250 $m^3\ m^{-3}$, respectively). Both soil types are prominent in Luzon according to the RAMS soil type database. Therefore, by testing these two soil types, we are able to vary permanent wilting point while approximately controlling for field capacity and saturation volumetric soil moisture, without substantial loss of realism. It should be noted that the permanent wilting point and field capacity in LEAF-3 are not specified but are rather calculated based on other soil parameters prescribed for each soil texture. This fact has two important implications: (1) it would be impractical and potentially unrealistic to hold saturation volumetric soil moisture and field

capacity values precisely constant while varying only the permanent wilting point; and (2) the two soil types examined here have other differences that influence processes such as heat and moisture conduction beyond the three parameters discussed here, and therefore we can expect variation between simulations with different soil textures beyond that which can be attributed to differences merely in field capacity and permanent wilting point.

Calculations of variables derived from parcel theory, such as convective available potential energy (CAPE) and the level of free convection (LFC), are performed using a version of the getcape.F code (version 1.04) from Cloud Model 1 (Bryan & Fritsch, 2002) that has been modified to use the physical constants and thermodynamic formulas used in RAMS. All calculations are pseudoadiabatic, and the latent heat of freezing is not considered.

In order to assess statistical significance of trends in total accumulated precipitation, we partition the 100 km × 100 km domain into an 8 × 8 grid containing a total of 12.5 km × 12.5 km subdomains. The mean precipitation is calculated for each of the 64 subdomains, and 95% confidence intervals for the mean are constructed using bootstrapping. This process assumes that the subdomains are statistically independent of one another, which appears to be approximately true given the small cloud sizes. In increasing the number of subdomains to values as large as 400, we find that the confidence interval bounds exhibit minimal sensitivity to the number of subdomains.

3.3 Results

3.3.1 Overall Results

Figure 3.1 shows the total domain-mean accumulated rainfall over the course of each simulation, as a function of initial soil moisture saturation fraction. The four curves correspond to the four series of simulations outlined in Section 3.2: (1) wooded grassland and silty clay loam

soil; (2) wooded grassland and clay loam soil, (3) bare silty clay loam soil; and (4) bare clay loam soil. Series 1 and 2, in which vegetation is present, exhibit qualitatively similar variation in accumulated rainfall as a function of initial soil moisture, as do Series 3 and 4, in which vegetation is absent. In all four series of simulations, there is limited soil moisture sensitivity for the driest and wettest soil moisture initializations.

When vegetation is absent (Series 3 and 4), rainfall increases nearly monotonically with increasing soil moisture. By contrast, when vegetation is present (Series 1 and 2), the curves' interiors are V-shaped, with the least rainfall occurring for mid-range values of initial soil moisture. As will be discussed later, the local minima in Series 1 and Series 2 occur for values slightly moister than the respective soil types' PWPs.

The initial soil moisture in these simulations potentially affects not only total precipitation accumulation, but also the timing of precipitation. Figure 3.2a shows time series of domain-mean accumulated rainfall for all ten simulations in Series 1 (wooded grassland, silty clay loam). Between 12:00 LT and 16:00 LT, the curves are clustered into three main groups. The three driest simulations (initialized at 25%, 40%, and 45% of soil saturation) exhibit the earliest precipitation, where "precipitation onset" may be defined to occur when the domain-mean accumulated precipitation first reaches ~0.02 mm. An alternative absolute metric, which is not shown but yields the same interpretation of results, is the time at which 1% of the domain has received 0.01 inches (0.254 mm) of rain. The three driest simulations are followed by the four wettest simulations (65%, 70%, 75%, and 95%) and then by the three intermediate-wetness simulations (50%, 55%, and 60%). The corresponding time series for Series 2 (wooded grassland, clay loam) behave qualitatively similarly to the Series 1 times series, although in Series 2 there is no delay in the intermediate-wetness simulations' onset of precipitation relative

to the wettest simulations' onset of precipitation. In Series 3 (bare soil, silty clay loam; Figure 3.2b) and Series 4 (bare soil, clay loam; not shown), wet soils generally exhibit an earlier onset of precipitation than do dry soils.

3.3.2 Simulations with Vegetation

When dense vegetation is present, as in Series 1 and Series 2, transpiration plays a significant role. By contrast, when vegetation is absent, as in Series 3 and Series 4, there is no transpiration, and therefore all surface latent heat fluxes occur via evaporation from the top soil level into the atmosphere. In LEAF-3, as in nature, transpiration and evaporation are governed by different factors. Transpiration is modulated by a stomatal conductance that depends on carbon dioxide availability, photosynthetically active radiation, temperature, and water stress, the latter of which has contributions both from soil moisture and from the humidity of the near-surface air (Lee, 1992). Since LEAF-3 does not track carbon dioxide concentrations, it is assumed that sufficient carbon dioxide is always available. A vegetation type-dependent base stomatal conductance is then multiplied by several factors ranging from 0 to 1, each representing one of the remaining processes that modulate stomatal conductance. The mathematical form of these factors, along with threshold values, can be found in (Lee, 1992).

3.3.3 Examination of Series 1

We now discuss the results from the ten Series 1 simulations in detail. Starting at the beginning of each simulation, the factor that immediately acts to distinguish the drier-soil simulations from the wetter-soil simulations is the soil moisture component of the water stress. Figure 3.3a shows how this factor varies as a function of soil moisture for both the silty clay loam and clay loam soil types. Below each soil type's PWP, the multiplicative factor is very close to 0. Above the PWP, the factor sharply increases to nearly 1. Therefore, transpiration is a

strong function of soil moisture via the soil moisture-based water stress control on stomatal conductance.

Figure 3.4a shows time series of stomatal resistance (the reciprocal of stomatal conductance) for the ten simulations in Series 1. Indeed, soon after the simulations are initialized, the stomatal resistance in the three driest simulations diverges from that in the seven wettest simulations. (This divergence is not instantaneous due to LEAF-3's built-in *e*-folding time of 15 minutes for changes in stomatal resistance.) As the simulations progress through the afternoon hours, the stomatal resistances in the three driest simulations grow by several orders of magnitude (note the logarithmic vertical axis), whereas the stomatal resistances in the seven wettest simulations remain approximately constant until sunset, when the lack of photosynthetically active radiation limits photosynthesis and thus increases stomatal resistance. The threshold separating the group of three dry simulations from the group of seven wet simulations appears to be the PWP, which occurs between 45% and 50% of saturation for the silty clay loam soil type used in Series 1.

In LEAF-3, transpiration is limited to 400 W m^{-2}. The remainder of the latent heat flux is accomplished by evaporation of water from the top soil level into the air above. This surface evaporation is driven by the difference between the soil-surface water vapor mixing ratio, $r_{v,sfc}$, and the canopy-air water vapor mixing ratio, $r_{v,canopy}$. Following the RAMS Technical Manual (Mission Research Corporation, 1997), the value of $r_{v,sfc}$ is calculated by combining formulas from (Philip, 1957) and (Lee & Pielke, 1992), and it has an explicit dependence on the field capacity but not the PWP. Figure 3.3b shows how $r_{v,sfc}$ depends on soil moisture for representative values of $r_{v,canopy}$, surface temperature, and surface pressure. Note that $r_{v,sfc}$ is essentially constant above the field capacity, which is nearly identical for the silty clay loam and

clay loam soil textures, and approaches the prescribed $r_{v,\mathrm{canopy}}$ value of $20\ \mathrm{g\ kg^{-1}}$ for saturation fractions below ~0.2 (20%). In between these two extremes, there is a gradual transition in direct surface evaporation from dry soils to wet soils. This transition contrasts with that for stomatal conductance, which more closely resembles a step function centered near the PWP.

In Series 1, surface evaporation does play a role in determining the total latent heat flux, which reaches values well above the transpiration limit of 400 W m^{-2}. The total latent heat fluxes in Series 1 (Figure 3.4b) appear to be dominated by transpiration, as the same partitioning into three dry-soil and seven wet-soil simulations as in Figure 3.4a is apparent. However, there is more variation in latent heat fluxes within each of the two groups than can be explained by the variation in stomatal resistance. It can therefore be concluded that the within-group variation in latent heat flux is due to differences in surface evaporation. In particular, during the time range of ~11:00 LT to ~16:00 LT, the latent heat flux increases as initial soil moisture is increased from 50% to 65% (just below the field capacity). For those simulations initialized with soil wetter than the field capacity, there is minimal variation in latent heat flux with increases in the initial soil moisture.

Since the sum of surface latent and sensible heat fluxes is largely constrained by surface insolation and albedo, which do not vary appreciably across the Series 1 simulations (not shown), increases (decreases) in surface latent heat fluxes across simulations translate (to first order) into decreases (increases) in surface sensible heat fluxes. Figure 3.4c shows time series of sensible heat fluxes for the ten simulations in Series 1. As was observed for latent heat fluxes, the simulations are partitioned into two groups: three simulations initialized with soil drier than the PWP, and seven simulations initialized with soil wetter than the PWP. Again, there is variation within each group, although the absolute values of the within-group differences in

sensible heat flux are smaller than those observed for latent heat fluxes. The lower magnitude of within-group sensible heat flux differences is likely due to a corresponding increase in ground heat flux associated with top-soil layer heating under dry-soil conditions.

When soil is drier than the PWP, latent heat fluxes diminish, thereby boosting the sensible heat fluxes. The stomatal resistance increases not only due to decreased soil moisture, but also due to increased temperatures and increased vapor pressure deficits. But even within the set of three driest simulations, latent heat fluxes increase with increasing initial soil moisture, and sensible heat fluxes decrease. Surface evaporation increases with increasing soil moisture over the sub-PWP range of soil moistures examined (25% – 45% of saturation; Figure 3.3b).

We now discuss the implications of changes in sensible and latent heat fluxes across simulations. Stronger sensible heat fluxes drive stronger boundary layer vertical motions (Figure 3.5). The two driest simulations displayed here (the 40% initial soil moisture simulation is omitted) exhibit much stronger boundary-layer vertical motions than do the seven wettest simulations, to the extent that different color scales must be used for the two groups in order to be able to discern the within-group trends. The three driest-soil simulations (one of which is not shown) also exhibit the deepest boundary-layer circulations.

These boundary-layer motions, in turn, generate clouds near the top of the boundary layer. Cloud fraction values (Figure 3.6) are greater, and clouds are deeper, in the two driest simulations than in the seven wettest simulations. This increased cloudiness translates into greater amounts of precipitation aloft (Figure 3.7). At heights between ~2 km and ~5.5 km, precipitation is much greater in the two driest-soil simulations than in the seven wettest-soil simulations. Nearly all of this precipitation exists in the form of rain (not shown). Therefore, it can be inferred that more precipitation is produced and/or lofted in the two driest simulations

than in the seven wettest simulations. The implications for the amount of precipitation reaching the ground will be discussed later in this section.

The seven wettest-soil simulations exhibit much larger surface latent heat fluxes (Figure 3.4b) and much smaller surface sensible heat fluxes (Figure 3.4c) than do the three driest-soil simulations. Therefore, the near-surface temperatures are lower (Figure 3.4f) and the near-surface water vapor mixing ratios are higher (Figure 3.4e). These combine to increase the near-surface relative humidity (Figure 3.4g), which in turn lowers the lifted condensation level (not shown) and the LFC (Figure 3.4h). This lowering of the LFC enables near-surface-based parcels to reach their LFCs without undergoing as much ascent as would otherwise be required. Among the seven wettest-soil simulations, the driest (initialized at 50% of saturation, hereafter S50) exhibits the lowest LFC, and the wettest (initialized at 95% of saturation, hereafter S95) exhibits the highest LFC (Figure 3.4d). Within the same group of seven simulations, boundary layer relative humidity is lowest in S50 (within the lowest ~1.3 km of the atmosphere, and lower than the S95 value by as much as ~7.5 percentage points; not shown). As a result, not only do S50 parcels need to ascend more in order to reach their LFC, but they also entrain drier air as they rise, thereby reducing their ability to reach their LFC.

The amount of entrainment may be greater in S50 as well given that this simulation exhibits stronger boundary layer motions in general than do the progressively wetter-soil simulations. Therefore, the difference between the parcel theory-based LFC and the higher-altitude (due to entrainment) actual LFC may be greater in S50 than in the wetter-soil simulations, further limiting the amount of moist convection in S50 compared to the wetter-soil simulations. Although the effects of increased LFC height may be counteracted somewhat by the increased strength of boundary layer updrafts in S50, the latter evidently does not dominate, as

less precipitation ultimately forms in S50 than in the wetter-soil simulations (Figure 3.4i provides some indication of this).

Not all of the rain that is produced by the boundary layer cumulus clouds in these simulations reaches the ground, especially in the three driest-soil simulations. This fact is readily apparent from the first two panels in Figure 3.7, which exhibit substantial vertical gradients in precipitation mixing ratios within the lowest ~2 km of the atmosphere. Several factors influence the proportion of rain reaching the ground, including vertical air motions, rain drop size distributions, and the depth and dryness of the subcloud layer.

The subcloud-layer saturation deficit, i.e., the difference between the saturation water vapor mixing ratio and the actual water vapor mixing ratio, varies tremendously across simulations (not shown; see Figure 3.4d for near-surface values). In the three driest-soil simulations (S25, S40, and S45, using the same naming convention as above), the saturation deficit is larger than in the seven wettest-soil simulations. Furthermore, the subcloud layer is deeper in the three driest-soil simulations. Therefore, falling rain drops have both more time to evaporate and a stronger evaporative forcing in the three driest-soil simulations, and as a result, the fraction of rain that reaches the surface is much lower than in the wetter-soil simulations. Among the seven wettest-soil simulations, there is a greater (by ~2.5 g kg^{-1}) boundary-layer saturation deficit in S50 than in S95 (not shown). As a result, it can be expected that a greater fraction of rain will evaporate before reaching the surface in S50 (see Figure 3.7), thereby resulting in less surface precipitation.

Assessing the vertical air motions within rain shafts would require a more sophisticated analysis than is performed here and is thus left for future work, although composites from Drager et al. (2020) suggest that rain shaft downdrafts are stronger under drier-soil scenarios. Mass-

weighted mean drop sizes (averaged across all points at a given level with a rain mixing ratio greater than 0.1 g kg^{-1}) at the top of the subcloud layer are nearly identical for all of the Series 1 simulations (not shown). Therefore, differences in the drop size distribution across simulations are unlikely to have any effect on the trends in surface rainfall.

3.3.4 Timing of Precipitation Onset

We now discuss the mechanisms behind the differences in precipitation onset time across the simulations in Series 1. As discussed previously, the onset of surface rainfall is earliest in the three dry-soil simulations (S25, S40, and S45) and later in the seven wet-soil simulations. However, among the seven wet-soil simulations, the four wettest-soil simulations (S65, S70, S75, and S95) exhibit an earlier onset of surface rainfall than do the three drier-soil simulations (S50, S60, and S65). In order for precipitation to form in any given simulation, lower boundary layer-based parcels must ascend beyond their lifted condensation levels (and ideally their LFCs, although this is not strictly required). Once cloud droplets have formed, they must undergo transformation into rain drops if surface precipitation is to form. This requires them to be present in sufficient concentration to be able to undergo collision-coalescence. The resultant rain drops will reach the ground provided that they do not fully evaporate and are not lofted by updrafts.

The white curves in Figure 3.5 indicate the LFC time evolution for each simulation. The dry-soil simulations (S25, S40, and S45) experience the earliest precipitation because there is more surface sensible heating. This sensible heating causes more rapid boundary layer development and thus stronger boundary layer vertical motions. These motions enable parcels to reach their LFCs, despite the fact that the LFCs are higher than in the seven wet-soil simulations. Even though the boundary layer motions reach their maximum magnitudes around the same time

in each of the simulations, these motions are much weaker overall in the wet-soil simulations than in the dry-soil simulations.

3.3.5 Role of the Permanent Wilting Point

The trends in Series 2 (wooded grassland, clay loam; Figure 3.8) largely mirror those in Series 1 (wooded grassland, silty clay loam; Figure 3.4), although there are some important differences. Recall that the silty clay loam soil type (Series 1) has a permanent wilting point between 45% and 50% of saturation, whereas clay loam (Series 2) has a permanent wilting point between 50% and 55% of saturation. Therefore, while the S50 simulation in Series 1 is initialized with soil that is moister than the PWP, the S50 simulation in Series 2 is initialized with soil that is drier than the PWP.

It was shown previously that the PWP governs stomatal conductance and thus latent heat fluxes, and it was speculated previously that it is by virtue of this PWP threshold that the Series 1 simulations are divided into a group of three dry-soil simulations and a group of seven wet-soil simulations. Examination of Figure 3.8 reveals that for Series 2, there are four dry-soil simulations and six wet-soil simulations: the S50 simulation has joined the dry-soil group. Given that the S50 simulation is drier than the PWP in Series 2 but not in Series 1, this result provides evidence that it is indeed the PWP threshold that divides the two groups.

3.3.6 Without Vegetation

In the absence of vegetation (Series 3 and Series 4), there is no transpiration, and so latent heat fluxes are governed entirely by surface evaporation. Therefore, the PWP threshold, which does not enter the calculation of surface evaporation, does not play a direct role. Recall that the transition in surface evaporation from dry soil to wet soil is much more gradual (Figure 3.3b) than that of transpiration (Figure 3.3a). As a result, each vegetation-free series of simulations

exhibits a smooth transition from dry-soil to wet-soil, rather than an abrupt transition at the permanent wilting point that partitions the series into two groups as is seen in the vegetated simulations.

Given surface evaporation's dependence on field capacity (~68% for both soil types tested; Figure 3.3b), surface evaporation might naïvely be expected to be a very weak function of initial soil moisture for values at and above 70%. However, the soil moisture at the top soil level decreases substantially over the course of the day in many of the simulations, and as a result, the three wettest-soil simulations (S70, S75, and S95) do exhibit divergent behavior as the simulations progress (Figure 3.2b).

Overall, in Series 3 and Series 4 (non-vegetated), more rain generally reaches the surface under wet-soil conditions than under dry-soil conditions (Figure 3.1). This result contrasts with the results from Series 1 and Series 2 (vegetated), for which the most rain reaches the surface under dry-soil conditions and the least rain reaches the surface for soils slightly moister than the permanent wilting point. Furthermore, for the wet-soil simulations, nearly 300% more rain reaches the surface in the non-vegetated simulations than in the vegetated simulations.

Different processes dominate when vegetation is present than when vegetation is absent. Most obviously, there is no transpiration; all latent heat fluxes take the form of direct surface evaporation. It appears that two primary factors are responsible for the trends in the non-vegetated simulations. The first is that the latent heat fluxes in the non-vegetated wet-soil simulations are enhanced compared to the vegetated wet-soil simulations (not shown) by virtue of greater top soil layer heating (due to the lack of shading by vegetation). These effects enable the development of large amounts (> 5000 J kg^{-1}) of convective available potential energy (CAPE, not shown) and very low LFCs (~800 m). Deep convection is therefore able to form in

the wet-soil, non-vegetated simulations, resulting in enhanced rainfall. The second factor responsible for the trends in the non-vegetated simulations is that, as was found for the vegetated simulations, a greater fraction of the rain that is produced reaches the surface under wet-soil simulations than under dry-soil simulations due to the presence of a moister subcloud layer and therefore less subcloud evaporation of rain.

3.4 Discussion

In this study we have discussed an "intermediate-disadvantage" soil moisture-precipitation relationship in which soils slightly moister than the PWP receive less rain than do very wet or very dry soils. Under this regime, intermediate-wetness soils also experience the latest onset of precipitation. The "intermediate disadvantage" occurs only when vegetation is present, as it is largely the vegetation, via transpiration, that makes the PWP relevant.

Under the vegetated conditions tested in this study, the strong sensible heat fluxes induced by dry soils promote strong boundary layer vertical motions that are able to reach and exceed the LFC, which spurs condensation and the formation of precipitation. However, much of the precipitation evaporates before reaching the land surface due to the dryness of the boundary layer. On the other hand, when soil is wet, latent heat fluxes result in moistening of the near-surface layer and therefore act to lower the LFC. This lowering of the LFC enables the relatively weak boundary layer motions to reach the LFC more easily.

In vegetated intermediate-soil moisture simulations initialized with soil slightly wetter than the PWP, the sensible heat fluxes are slightly stronger than in the wet-soil simulations, and the latent heat fluxes are slightly weaker. These changes act to strengthen the boundary layer motions and increase the LFC relative to the wet-soil simulations. Evidently, the slightly increased boundary layer motion strength is insufficient to offset the effects of an increased LFC

in terms of precipitation. The boundary layer as a whole becomes drier than in the wet-soil simulations, which acts both to decrease the relative humidity within updrafts and to promote subcloud evaporation of falling precipitation. As a result, the intermediate-soil moisture simulations receive just over half as much precipitation as do the wet-soil and dry-soil simulations.

Most previous work examining soil moisture-precipitation interactions has considered only monotonic responses, in which precipitation either increases or decreases consistently with increasing soil moisture. One exception to this is Barthlott and Kalthoff (2011), who obtained an intermediate-soil wetness advantage when considering wet soils. The potential existence of non-monotonic responses, as suggested by both Barthlott and Kalthoff (2011) and the present study (albeit with opposite signs), is not considered by theoretical frameworks such as CTP-HI_{low}.

The present study implies that "wet-soil advantage" and "dry-soil advantage" are, at least in some cases, neither complete nor mutually exclusive descriptors. They are incomplete in that neither fully describes the response of afternoon precipitation to soil moisture. And although they seemingly describe opposite trends, both responses are present in a "piecewise" sense in the response obtained here. In Series 1 and Series 2, precipitation decreases with increasing soil moisture as the initial soil moisture approaches the PWP, constituting a dry-soil advantage, and then, as initial soil moisture approaches the field capacity, the precipitation increases with increasing soil moisture, which constitutes a wet-soil advantage. In other words, dry soils exhibit a dry-soil advantage, and wet soils exhibit a wet-soil advantage.

Our results for Series 1 and Series 2 also highlight the importance of the PWP for precipitation over vegetated surfaces. Several previous studies (e.g., Barthlott & Kalthoff, 2011; Hohenegger et al., 2009) have altered soil moisture in spatially heterogeneous conditions by

applying a spatially homogeneous soil moisture offset, thereby changing the locations in which the PWP is exceeded. Such an approach can obscure the effects of the underlying physical processes by altering the geographical locations in which soil-moisture breezes develop. Therefore, we recommend that future modeling studies aiming to elucidate the processes governing the soil moisture-precipitation relationship consider the existence of the PWP threshold when perturbing initial soil moisture conditions.

The non-vegetated Series 3 and Series 4, on the other hand, do not experience the intermediate-soil moisture disadvantage that constitutes the main focus of this study. Instead, there is a wet-soil advantage. The precipitation trends with changes in soil moisture do not exhibit strong PWP dependence either; instead, there is a gradual transition in simulation properties with changes in soil moisture. These results are attributable to the non-dependence of direct surface evaporation of moisture on the PWP. Other models use different formulations of direct surface evaporation. For instance, the scheme of Chen and Dudhia (2001) eliminates surface evaporation below the PWP and therefore might be expected to produce results that vary from those obtained here.

It is worth noting that when only the extreme cases (S25 and S95) of Series 1 and Series 2 are considered, the CTP-HI_{low} framework of Findell and Eltahir (2003a) does perform as intended. The CTP-HI_{low} framework predicts that our initial sounding will give rise to a dry-soil advantage situation, and indeed, the driest simulations exhibit earlier onset and somewhat greater accumulation of rainfall than do the wettest simulations. However, the CTP-HI_{low} framework does not predict the wet-soil advantage obtained in the bare-soil simulations (Series 3 and Series 4). Further investigation is required in order to determine the mechanisms behind this wet-soil advantage. Nevertheless, the existence of opposite soil moisture-precipitation relationships over

vegetated surfaces compared with bare soils suggests that different mechanisms may be active during different parts of the growing season as crops grow.

Our results suggest several potential avenues for future research. Similar experiments to those performed here should be conducted in which different initial atmospheric conditions (temperature, humidity, and wind) are used. Indeed, several studies, including Findell and Eltahir (2003b) and Cioni and Hohenegger (2017), suggest that initial wind conditions and large-scale forcing can play an important role in modulating soil moisture-precipitation feedbacks. This possibility is not explored in the present study, which examines scenarios with initially calm winds only in order to prevent large-scale winds from acting as a confounding factor. Furthermore, we have in effect sampled only one point in CTP-HI_{low} space, and it is likely that other initial thermodynamic and moisture conditions, particularly those with different CTP-HI_{low} classifications, would produce different responses. It would also be useful to perturb the land surface and vegetation properties and test different land-surface parameterization schemes. Finally, we have only considered short-duration simulations with essentially spatially homogeneous initial conditions. Although such simulations are essential for elucidating processes, there may exist other mechanisms in nature that emerge only in the presence of heterogeneity or over the course of several days. All of these avenues for future research have the potential to further our understanding of the conditions under which an intermediate-soil moisture disadvantage may be likely to occur.

3.5 Figures

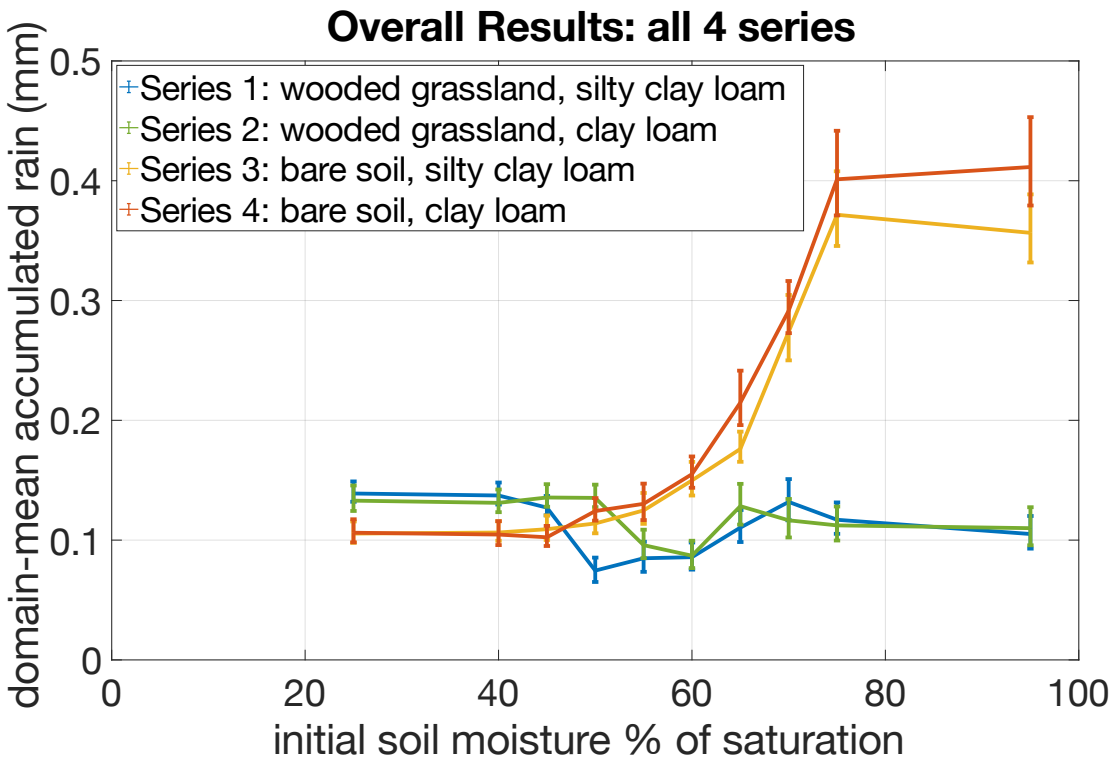

Figure 3.1. Domain-mean accumulated rainfall, as a function of initial soil moisture, at the end of each of the 40 simulations. Error bars indicate 95% confidence intervals for the mean calculated using the approach described in Section 3.2.

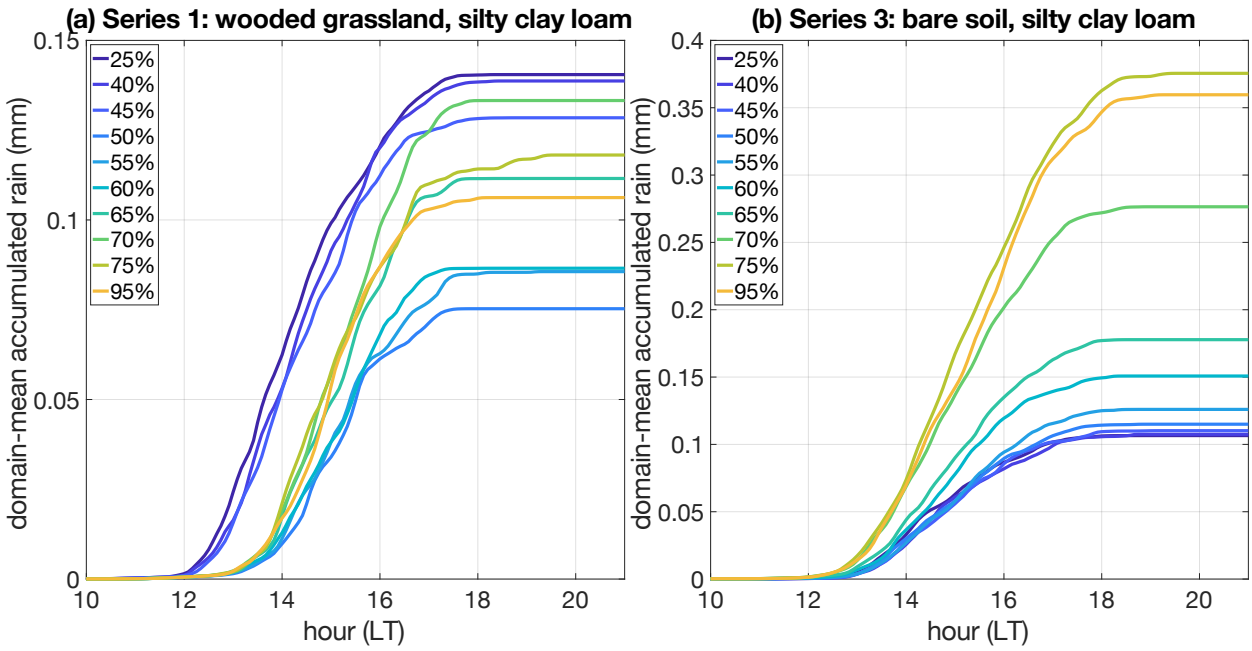

Figure 3.2. Accumulated precipitation as a function of time for the Series 1 (wooded grassland, silty clay loam) and Series 3 (bare soil, silty clay loam). Each curve corresponds to a single simulation whose initial soil moisture (fraction of saturation) is indicated by the legend.

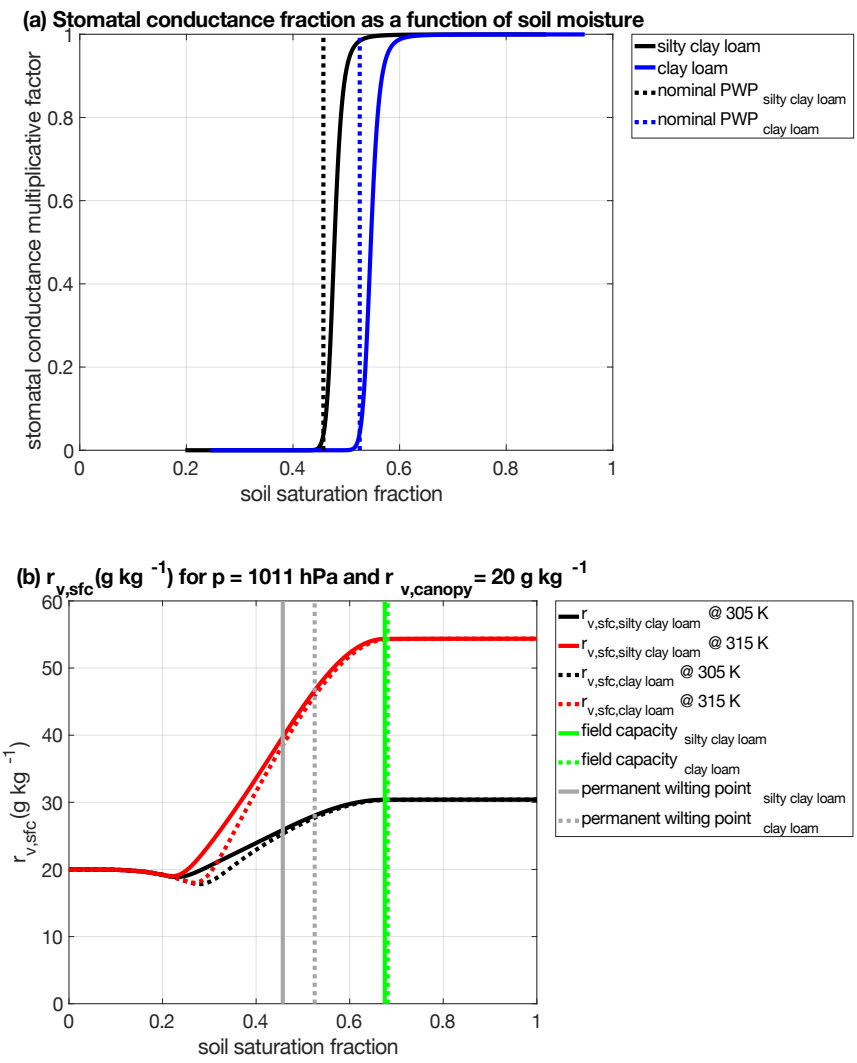

Figure 3.3. Evapotranspiration in the LEAF-3 soil-vegetation-atmosphere transfer scheme. Panel (a) shows the extent to which soil moisture limits transpiration, via a multiplicative factor that ranges from 0 (no transpiration allowed) to 1 (soil moisture does not limit stomatal conductance). Panel (b) shows the soil moisture dependence of the soil-surface water vapor mixing ratio, $r_{\mathrm{v,sfc}}$, for surface pressure $p_{\mathrm{sfc}} = 1011$ hPa, canopy water vapor mixing ratio $r_{\mathrm{v,canopy}} = 20$ g kg^{-1}, and top-soil layer temperature $T_{\mathrm{sfc}} = 305$ K (black) and $T_{\mathrm{sfc}} = 315$ K (red).

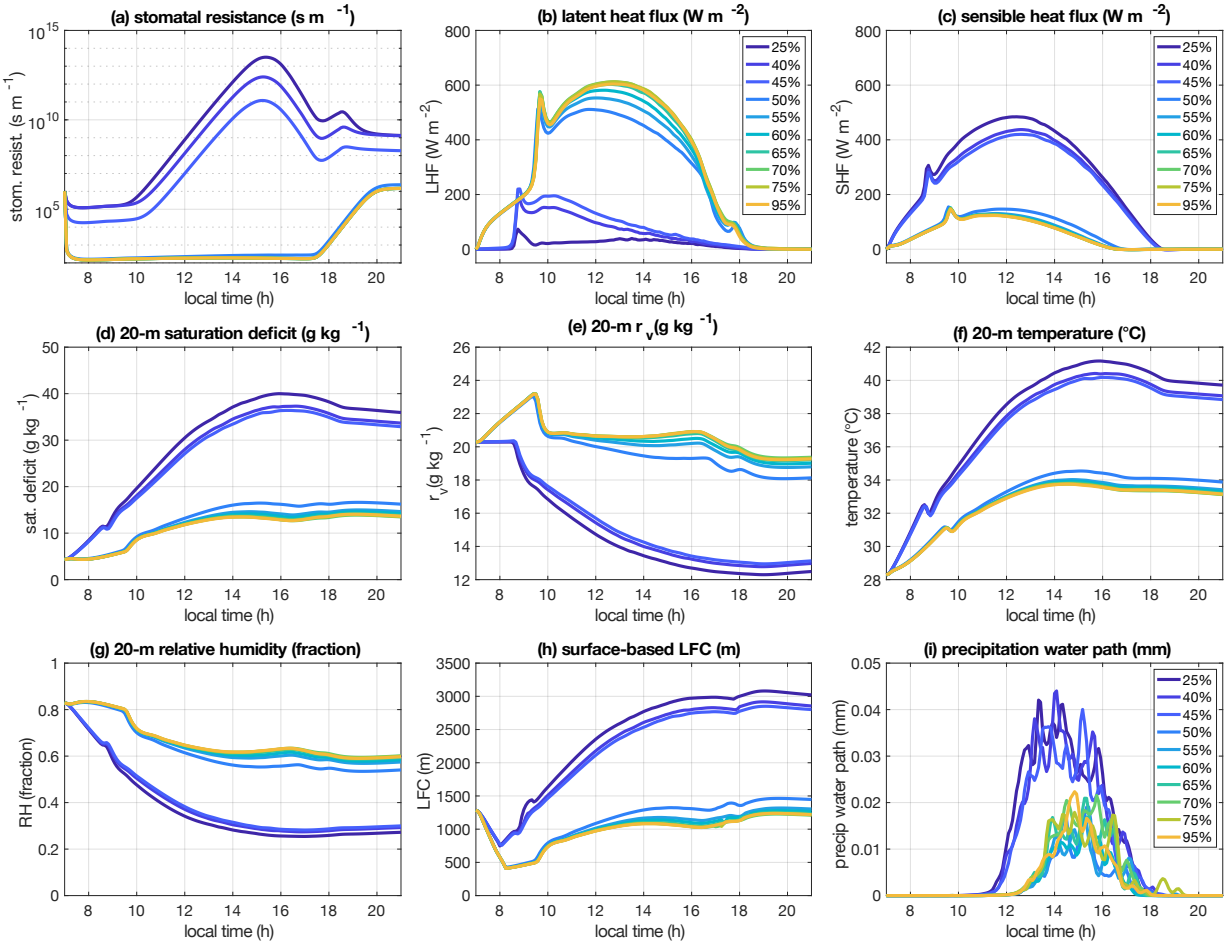

Figure 3.4. Time series of various quantities for Series 1 (wooded grassland, silty clay loam). Each curve represents a different simulation, with the legend indicating the initial soil moisture fraction. Quantities include (a) domain-mean stomatal resistance (note log scale); (b) domain-mean latent heat flux; (c) domain-mean sensible heat flux; (d) domain-mean saturation deficit at the lowest above-ground model level, $z \sim 20$ m; (e) domain-mean water vapor mixing ratio at $z \sim 20$ m; (f) domain-mean temperature at $z \sim 20$ m; (g) domain-mean relative humidity at $z \sim 20$ m; (h) level of free convection for the domain-mean sounding; and (i) domain-mean precipitation water path.

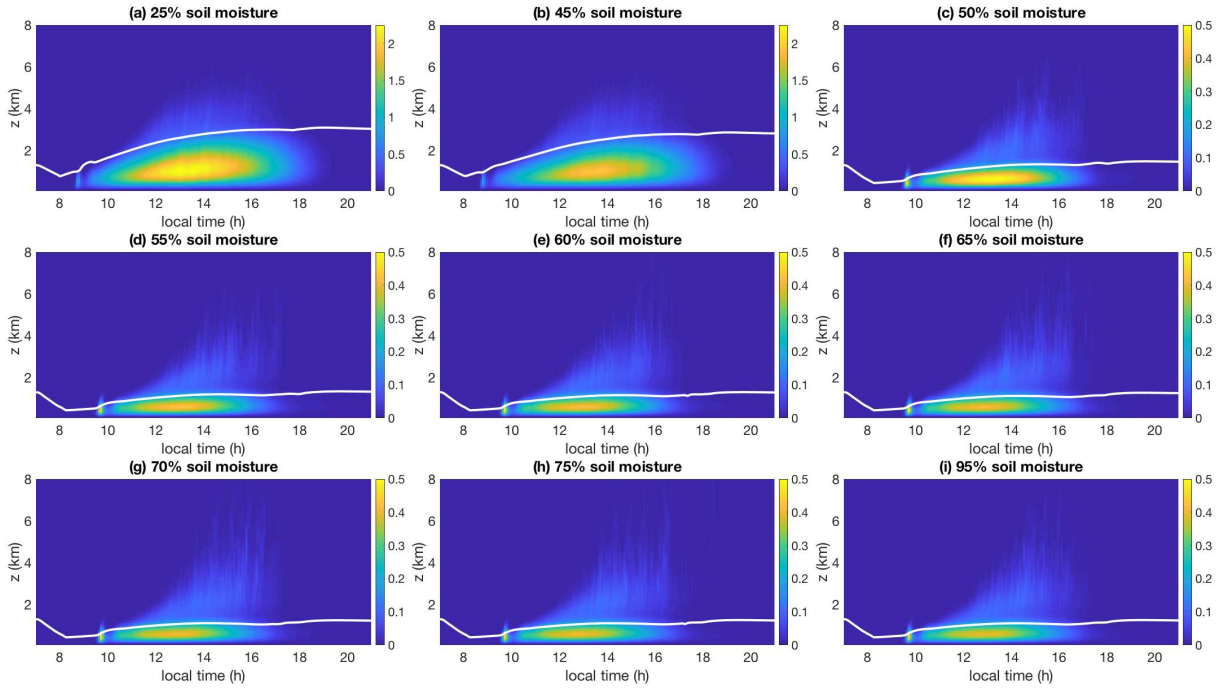

Figure 3.5. Domain-mean kinetic energy of vertical motions (J kg^{-1}), computed by taking the horizontal average of $\frac{w^2}{2}$, is plotted in the color shading as a function of time and altitude for nine out of the ten simulations in Series 1 (wooded grassland, silty clay loam). The surface parcel-based level of free convection, based on the domain-mean sounding at each output time, is plotted in white. The 40% soil moisture simulation is omitted here and in the next two figures due to graphical constraints. Note that the first two panels use a different color scale than do the remaining seven.

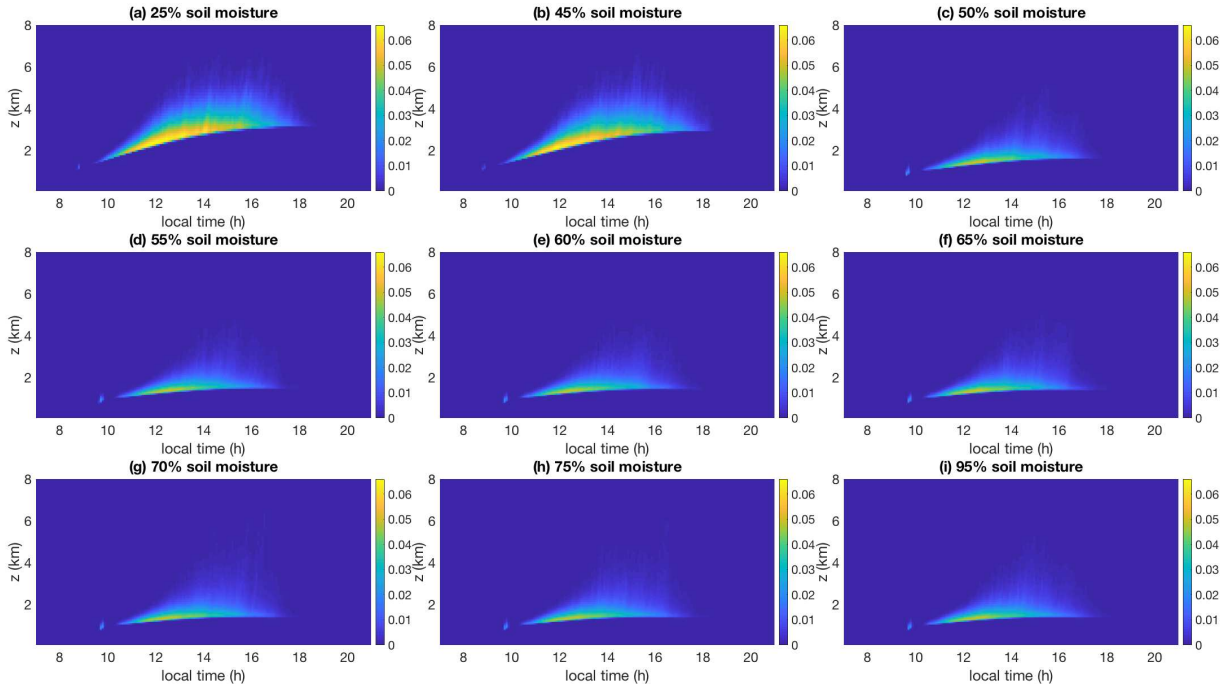

Figure 3.6. Cloud fraction, calculated as the fraction of points at a given height with a total cloud water and cloud ice mixing ratio of at least 0.1 g kg^{-1}, as a function of time and altitude for nine out of the ten simulations in Series 1 (wooded grassland, silty clay loam).

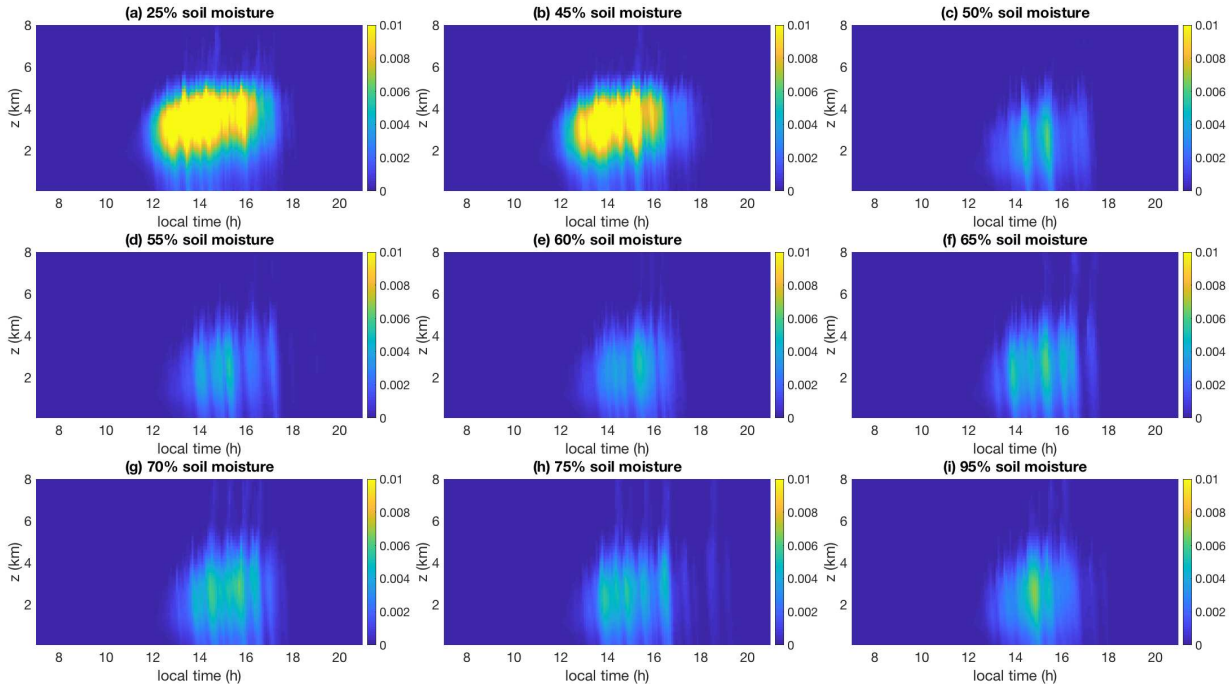

Figure 3.7. Horizontal-mean precipitation mixing ratio (g kg^{-1}), calculated based on the summed mixing ratios of all non-cloud hydrometeor types, as a function of time and altitude for nine out of the ten simulations in Series 1 (wooded grassland, silty clay loam).

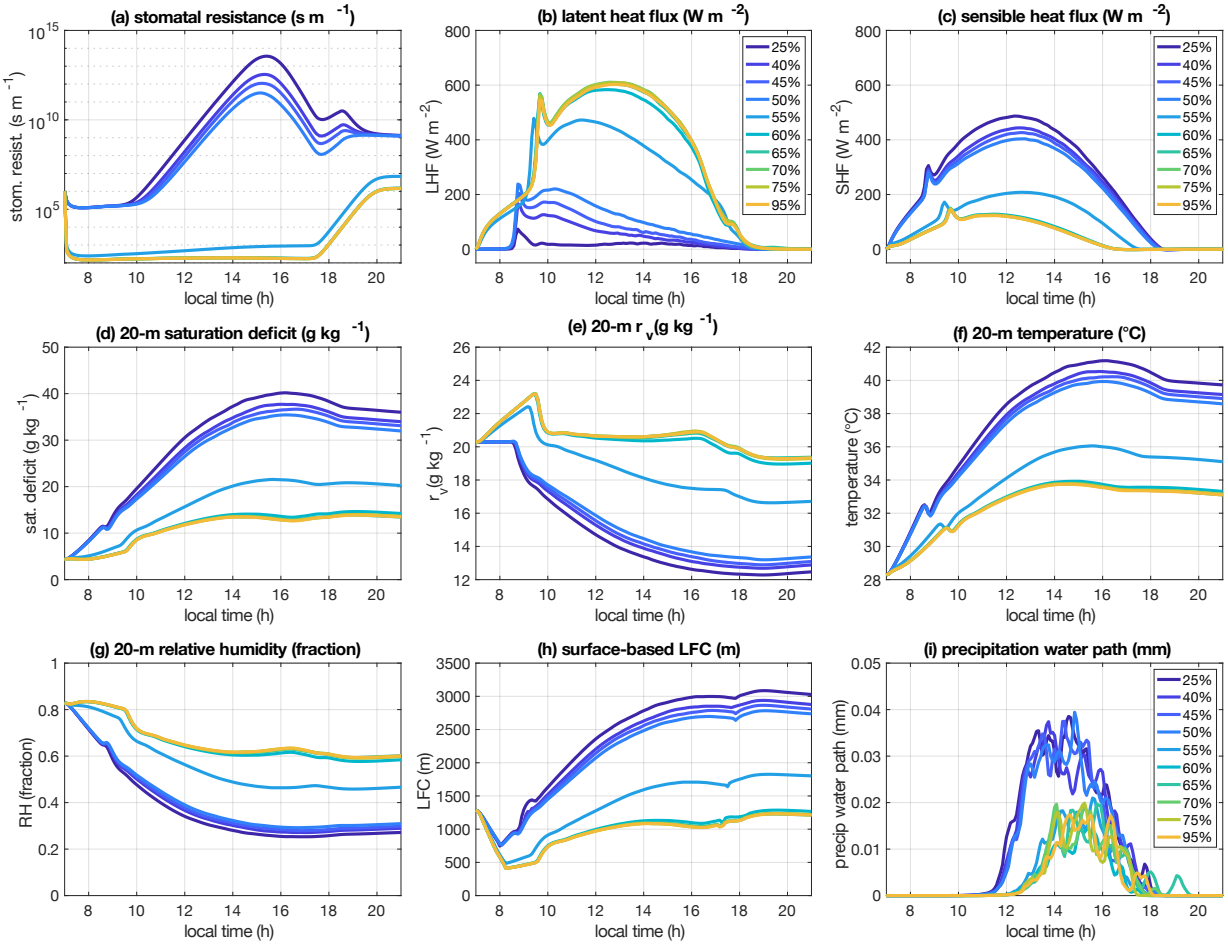

Figure 3.8. As in Figure 3.4, except for Series 2 (wooded grassland, clay loam).

CHAPTER 4: CONCLUDING REMARKS

4.1 Main Conclusions

The goals of this dissertation were (1) to understand how convective cold pool properties change as a function of soil moisture, and (2) to explore the mechanisms behind the "intermediate-soil moisture disadvantage" with respect to afternoon precipitation that was discovered during the cold pool investigation.

In order to achieve the first goal, five high-resolution ($\Delta x = \Delta y = 125$ m; $\Delta z =$ 40 m stretched to 250 m) simulations of continental convection were performed, each with a different initial spatially homogeneous soil moisture content. These were named the DRENCHED-SOIL (initialized at 95% of saturation), WET-SOIL (75%), MID-SOIL (50%), PWP-SOIL (45%), and DRY-SOIL (25%) simulations. Improvements were made to the Drager and van den Heever (2017) cold pool identification and tracking algorithm, and the revised algorithm was applied to the simulation outputs. From there, cold pool statistics were calculated, and cold pool composites were created. The main findings were as follows:

- The statistics and composites for the DRENCHED-SOIL, WET-SOIL, and MID-SOIL simulations closely resembled one another, as did those for the PWP-SOIL and DRY-SOIL simulations. The "dividing line" between these two groups of simulations was the permanent wilting point (PWP), which is a soil moisture threshold below which plants' roots are unable to extract water from the soil. The PWP has previously been hypothesized to be important for the formation of atmospheric circulations over land (Hohenegger & Stevens, 2018); however, this is the first time it has been shown to be relevant to cold pools.

- The cold pools in the dry-soil group of simulations (PWP-SOIL and DRY-SOIL) were wider, deeper, shorter-lived, and stronger than those in the wet-soil group of simulations (DRENCHED-SOIL, WET-SOIL, and MID-SOIL).
- The rings of enhanced humidity surrounding cold pools that have been hypothesized in previous studies (see Chapter 1) were only present in the wet-soil group of simulations. Furthermore, these rings were located outside the boundaries of the cold pools, rather than inside the cold pool boundaries as some previous studies have suggested.
- In the dry-soil group of simulations, "puddles" of enhanced humidity were present throughout the cold pool interiors. This result is consistent with a study by Redl et al. (2015), which identified cold pools from surface observations in semiarid northern Africa using a characteristic increase in dew-point temperature.

Overall, these results imply different potential roles for cold pools in wetter-soil versus drier-soil environments. We hypothesized that in wet-soil situations, the *thermodynamic forcing* mechanism of cold pool-induced convective initiation (see Chapter 1) dominates, whereas in dry-soil situations, the *mechanical forcing* mechanism dominates.

The second goal of the dissertation, which was to understand the "intermediate-soil moisture disadvantage" obtained in Chapter 2, was addressed by running four suites of ten simulations. Each simulation used a setup similar to that of Chapter 2, except with somewhat coarser resolution ($\Delta x = \Delta y = 250$ m; Δz same as before) and a somewhat smaller domain in order to reduce computational expense per simulation. Each suite had a different type of land surface (silty clay loam vs. clay loam, wooded grassland vs. no vegetation), and each simulation within a given suite was initialized with a different soil moisture content (25%, 40%, 45%, 50%, 55%, 60%, 65%, 70%, 75%, and 95% of saturation). When the wooded grassland vegetation type

and silty clay loam soil texture from Chapter 2 were used, this setup was able to reproduce the "intermediate-soil moisture disadvantage" that was identified in the higher-resolution simulations that were performed to address the first goal. Several diagnostic analyses were performed on the model outputs, resulting in the following conclusions:

- The intermediate-soil moisture disadvantage occurred for soils slightly moister than the PWP in the presence of vegetation. This result held for both soil textures tested, despite the fact that these soil textures' PWP values differed by ~5%.
- When vegetation was present, latent heat fluxes were largely controlled by the PWP, which governed transpiration through the model's stomatal resistance formulation.
- For soils drier than the PWP, latent heat fluxes were suppressed, and sensible heat fluxes were enhanced. This resulted in a dry, warm, deep boundary layer with strong vertical motions that were able to reach beyond the level of free convection (LFC), thereby producing abundant clouds and precipitation. However, most of the precipitation evaporated before reaching the ground by virtue of the dryness of the boundary layer.
- For soils wetter than the PWP, latent heat fluxes were enhanced and increased with increasing soil moisture. Sensible heat fluxes were suppressed, decreasing with increasing soil moisture. As a result, the boundary layer relative humidity increased with increasing soil moisture. This had two implications: (1) the LFC was lowest in the wettest-soil simulations, which allowed clouds to form more easily; and (2) the boundary layer saturation deficit was smallest in the wettest-soil simulations, which reduced the amount of precipitation that evaporated as it fell through the subcloud layer. As a result, more surface precipitation occurred in the wettest-soil simulations than in the moderately-wet soil simulations that were only slightly moister than the PWP.

- In the absence of vegetation, the PWP was unimportant because it does not play a role in direct surface evaporation, although this result may be particularly sensitive to the choice of parameterization. Overall, in the two bare-soil simulations, there was a wet-soil advantage.

These results suggested that vegetation plays an important role in modulating soil moisture-precipitation interactions. Another important implication was that dry-soil advantage and wet-soil advantage regimes are not mutually exclusive: they can both be present in a "piecewise" sense, such that dry soils exhibit a dry-soil advantage, wet-soils exhibit a wet-soil advantage trend, and intermediate-soil moisture simulations experience the lowest amount and latest onset of precipitation.

4.2 Future Work

The results from the two studies presented in this dissertation suggest multiple avenues for future research. One challenge in addressing the first goal of the dissertation was to track cold pools from their first appearance through to their dissipation. In the time since the work for Chapter 2 was completed, two promising cold pool tracking algorithms have been developed (Fournier & Haerter, 2019; Henneberg et al., 2020). It would be interesting to apply these algorithms to the simulations performed in Chapter 2 and to see whether the results differ. Furthermore, in light of the results of Chapter 3, it is unlikely that the same grouping of the Chapter 2 simulations into three wet-soil simulations and two dry-soil simulations would emerge in the absence of vegetation.

The results of Chapter 3 imply that future studies, especially case-study simulations, should take the PWP into account in their experimental design. It would be interesting to conduct simulations such as those conducted by Barthlott and Kalthoff (2011) with uniform soil moisture

values relative to the PWP, rather than with uniform offsets from the observed soil moisture. Such an approach is recommended because localized variations above and below the PWP can create local circulations that could complicate attempts to isolate the physical mechanisms governing the precipitation response to soil moisture. Furthermore, in both Chapter 2 and Chapter 3, only one sounding, from the Philippine archipelago, is used to initialize simulations. In order to assess the potential prevalence of the "intermediate-soil moisture disadvantage," as well as the applicability of the cold pool results to other situations, it is necessary to run additional simulations with soundings from other times of year and other geographical locations.

Finally, it should be emphasized that all conclusions obtained from these two studies are based on simulations, not observations. Field campaigns and other types of observations (e.g., radar, satellite) are essential for assessing the validity of the soil moisture-cold pool and soil moisture-precipitation relationships obtained here.

Nevertheless, much has been learned from these high-resolution, process-oriented model simulations regarding the mechanisms behind the interactions between soil moisture, cold pools, and afternoon convective precipitation. It is hoped that in the future, this new knowledge can be applied to parameterizations used in large-scale, coarse-resolution models in order to improve predictions and projections of weather and climate for the good of society.

REFERENCES

Baranowski, D. B., Waliser, D. E., Jiang, X., Ridout, J. A., & Flatau, M. K. (2018). Contemporary GCM Fidelity In Representing The Diurnal Cycle Of Precipitation Over The Maritime Continent. *Journal of Geophysical Research: Atmospheres*. https://doi.org/10.1029/2018JD029474

Barthlott, C., & Kalthoff, N. (2011). A Numerical Sensitivity Study on the Impact of Soil Moisture on Convection-Related Parameters and Convective Precipitation over Complex Terrain. *Journal of the Atmospheric Sciences*, *68*(12), 2971–2987. https://doi.org/10.1175/JAS-D-11-027.1

Böing, S. J., Jonker, H. J. J., Siebesma, A. P., & Grabowski, W. W. (2012). Influence of the Subcloud Layer on the Development of a Deep Convective Ensemble. *Journal of the Atmospheric Sciences*, *69*(9), 2682–2698. https://doi.org/10.1175/JAS-D-11-0317.1

Bowen, I. S. (1926). The Ratio of Heat Losses by Conduction and by Evaporation from any Water Surface. *Physical Review*, *27*(6), 779–787. https://doi.org/10.1103/PhysRev.27.779

Bryan, G. H., & Fritsch, J. M. (2002). A Benchmark Simulation for Moist Nonhydrostatic Numerical Models. *Monthly Weather Review*, *130*(12), 2917–2928. https://doi.org/10.1175/1520-0493(2002)130<2917:ABSFMN>2.0.CO;2

Chandra, A. S., Zuidema, P., Krueger, S., Kochanski, A., de Szoeke, S. P., & Zhang, J. (2018). Moisture Distributions in Tropical Cold Pools From Equatorial Indian Ocean Observations and Cloud-Resolving Simulations. *Journal of Geophysical Research: Atmospheres*, *123*(20), 11,445-11,465. https://doi.org/10.1029/2018JD028634

Chen, F., & Dudhia, J. (2001). Coupling an Advanced Land Surface–Hydrology Model with the Penn State–NCAR MM5 Modeling System. Part I: Model Implementation and Sensitivity. *Monthly Weather Review*, *129*(4), 569–585. https://doi.org/10.1175/1520-0493(2001)129<0569:CAALSH>2.0.CO;2

Chlond, A., Böhringer, O., Auerswald, T., & Müller, F. (2014). The effect of soil moisture and atmospheric conditions on the development of shallow cumulus convection: A coupled large-eddy simulation–land surface model study. *Meteorologische Zeitschrift*, 491–510. https://doi.org/10.1127/metz/2014/0576

Cioni, G., & Hohenegger, C. (2017). Effect of Soil Moisture on Diurnal Convection and Precipitation in Large-Eddy Simulations. *Journal of Hydrometeorology*, *18*(7), 1885–1903. https://doi.org/10.1175/JHM-D-16-0241.1

Copernicus Climate Change Service (C3S). (2017). ERA5: Fifth generation of ECMWF atmospheric reanalyses of the global climate. Retrieved January 1, 2019, from https://cds.climate.copernicus.eu/cdsapp#!/home

Cotton, W. R., Pielke Sr., R. A., Walko, R. L., Liston, G. E., Tremback, C. J., Jiang, H., et al. (2003). RAMS 2001: Current status and future directions. *Meteorology and Atmospheric Physics*, *82*(1), 5–29. https://doi.org/10.1007/s00703-001-0584-9

Dawson, D. T., Xue, M., Milbrandt, J. A., & Yau, M. K. (2010). Comparison of Evaporation and Cold Pool Development between Single-Moment and Multimoment Bulk Microphysics Schemes in Idealized Simulations of Tornadic Thunderstorms. *Monthly Weather Review*, *138*(4), 1152–1171. https://doi.org/10.1175/2009MWR2956.1

de Szoeke, S. P., Skyllingstad, E. D., Zuidema, P., & Chandra, A. S. (2017). Cold Pools and Their Influence on the Tropical Marine Boundary Layer. *Journal of the Atmospheric Sciences*, *74*(4), 1149–1168. https://doi.org/10.1175/JAS-D-16-0264.1

Del Genio, A. D., Wu, J., Wolf, A. B., Chen, Y., Yao, M.-S., & Kim, D. (2015). Constraints on Cumulus Parameterization from Simulations of Observed MJO Events. *Journal of Climate*, *28*(16), 6419–6442. https://doi.org/10.1175/JCLI-D-14-00832.1

DeMott, P. J., Prenni, A. J., Liu, X., Kreidenweis, S. M., Petters, M. D., Twohy, C. H., et al. (2010). Predicting global atmospheric ice nuclei distributions and their impacts on climate. *Proceedings of the National Academy of Sciences of the United States of America*, *107*(25), 11217–22. https://doi.org/10.1073/pnas.0910818107

Dirmeyer, P. A., Cash, B. A., Kinter, J. L., Jung, T., Marx, L., Satoh, M., Stan, C., Tomita, H., et al. (2012). Simulating the diurnal cycle of rainfall in global climate models: resolution versus parameterization. *Climate Dynamics*, *39*(1), 399–418. https://doi.org/10.1007/s00382-011-1127-9

Drager, A. J. (2016). *Convective Cold Pools: Characterization and Soil Moisture Dependence* (M.S.). Colorado State University.

Drager, A. J., & van den Heever, S. C. (2017). Characterizing convective cold pools. *Journal of Advances in Modeling Earth Systems*, *9*(2), 1091–1115. https://doi.org/10.1002/2016MS000788

Drager, A. J., Grant, L. D., & van den Heever, S. C. (2020). *Cold Pool Responses to Changes in Soil Moisture*.

Ek, M., & Mahrt, L. (1994). Daytime Evolution of Relative Humidity at the Boundary Layer Top. *Monthly Weather Review*, *122*(12), 2709–2721. https://doi.org/10.1175/1520-0493(1994)122<2709:DEORHA>2.0.CO;2

Ek, M. B., & Holtslag, A. A. M. (2004). Influence of Soil Moisture on Boundary Layer Cloud Development. *Journal of Hydrometeorology*, *5*(1), 86–99. https://doi.org/10.1175/1525-7541(2004)005<0086:IOSMOB>2.0.CO;2

Eltahir, E. A. B., & Bras, R. L. (1996). Precipitation recycling. *Reviews of Geophysics*, *34*(3), 367–378. https://doi.org/10.1029/96RG01927

Emanuel, K. A. (1994). *Atmospheric Convection*. New York: Oxford University Press.

Falk, N. M., Igel, A. L., & Igel, M. R. (2019). The Relative Impact of Ice Fall Speeds and Microphysics Parameterization Complexity on Supercell Evolution. *Monthly Weather Review*, *147*(7), 2403–2415. https://doi.org/10.1175/MWR-D-18-0417.1

Fast, J. D., Berg, L. K., Feng, Z., Mei, F., Newsom, R., Sakaguchi, K., & Xiao, H. (2019). The Impact of Variable Land-Atmosphere Coupling on Convective Cloud Populations Observed During the 2016 HI-SCALE Field Campaign. *Journal of Advances in Modeling Earth Systems*, *11*(8), 2629–2654. https://doi.org/10.1029/2019MS001727

Feng, Z., Hagos, S., Rowe, A. K., Burleyson, C. D., Martini, M. N., & de Szoeke, S. P. (2015). Mechanisms of convective cloud organization by cold pools over tropical warm ocean during the AMIE/DYNAMO field campaign. *Journal of Advances in Modeling Earth Systems*, 357–381. https://doi.org/10.1002/2014MS000384

Findell, K. L., & Eltahir, E. A. B. (1997). An analysis of the soil moisture-rainfall feedback, based on direct observations from Illinois. *Water Resources Research*, *33*(4), 725–735. https://doi.org/10.1029/96WR03756

Findell, K. L., & Eltahir, E. A. B. (2003a). Atmospheric Controls on Soil Moisture–Boundary Layer Interactions. Part I: Framework Development. *Journal of Hydrometeorology*, *4*(3), 552–569. https://doi.org/10.1175/1525-7541(2003)004<0552:ACOSML>2.0.CO;2

Findell, K. L., & Eltahir, E. A. B. (2003b). Atmospheric controls on soil moisture-boundary layer interactions: Three-dimensional wind effects. *Journal of Geophysical Research*, *108*(D8), 8385. https://doi.org/10.1029/2001JD001515

Findell, K. L., Gentine, P., Lintner, B. R., & Kerr, C. (2011). Probability of afternoon precipitation in eastern United States and Mexico enhanced by high evaporation. *Nature Geoscience*, *4*(7), 434–439. https://doi.org/10.1038/ngeo1174

Ford, T. W., Rapp, A. D., Quiring, S. M., & Blake, J. (2015). Soil moisture–precipitation coupling: observations from the Oklahoma Mesonet and underlying physical mechanisms. *Hydrology and Earth System Sciences*, *19*(8), 3617–3631. https://doi.org/10.5194/hess-19-3617-2015

Fournier, M. B., & Haerter, J. O. (2019). Tracking the Gust Fronts of Convective Cold Pools. *Journal of Geophysical Research: Atmospheres*, *124*(21), 11103–11117. https://doi.org/10.1029/2019JD030980

Garratt, J. R. (1992). *The Atmospheric Boundary Layer*. Cambridge University Press.

Gentine, P., Holtslag, A. A. M., D'Andrea, F., & Ek, M. (2013). Surface and Atmospheric Controls on the Onset of Moist Convection over Land. *Journal of Hydrometeorology*, *14*(5), 1443–1462. https://doi.org/10.1175/JHM-D-12-0137.1

Gentine, P., Garelli, A., Park, S. B., Nie, J., Torri, G., & Kuang, Z. (2016). Role of surface heat fluxes underneath cold pools. *Geophysical Research Letters*, *43*(2), 874–883. https://doi.org/10.1002/2015GL067262

Giorgi, F., Mearns, L. O., Shields, C., & Mayer, L. (1996). A Regional Model Study of the Importance of Local versus Remote Controls of the 1988 Drought and the 1993 Flood over the Central United States. *Journal of Climate*, *9*(5), 1150–1162. https://doi.org/10.1175/1520-0442(1996)009<1150:ARMSOT>2.0.CO;2

Grant, L. D., & van den Heever, S. C. (2014). Aerosol-cloud-land surface interactions within tropical sea breeze convection. *Journal of Geophysical Research: Atmospheres*, *119*, 8340–8361. https://doi.org/10.1002/2014JD021912

Grant, L. D., & van den Heever, S. C. (2015). Cold Pool and Precipitation Responses to Aerosol Loading: Modulation by Dry Layers. *Journal of the Atmospheric Sciences*, *72*(4), 1398–1408. https://doi.org/10.1175/JAS-D-14-0260.1

Grant, L. D., & van den Heever, S. C. (2016). Cold pool dissipation. *Journal of Geophysical Research: Atmospheres*, *121*(3), 1138–1155. https://doi.org/10.1002/2015JD023813

Grant, L. D., & van den Heever, S. C. (2018). Cold Pool-Land Surface Interactions in a Dry Continental Environment. *Journal of Advances in Modeling Earth Systems*, *10*(7), 1513–1526. https://doi.org/10.1029/2018MS001323

Guillod, B. P., Orlowsky, B., Miralles, D. G., Teuling, A. J., & Seneviratne, S. I. (2015). Reconciling spatial and temporal soil moisture effects on afternoon rainfall. *Nature Communications*, *6*(1), 1–6. https://doi.org/10.1038/ncomms7443

Harrington, J. Y. (1997). *The effects of radiative and microphysical processes on simulated warm and transition season Arctic stratus* (Ph.D. dissertation). Colorado State Univ., Fort Collins.

Henneberg, O., Meyer, B., & Haerter, J. O. (2020). Particle-based tracking of cold pool gust fronts. *Journal of Advances in Modeling Earth Systems*, *n/a*(n/a), e2019MS001910. https://doi.org/10.1029/2019MS001910

Hill, G. E. (1974). Factors Controlling the Size and Spacing of Cumulus Clouds as Revealed by Numerical Experiments. *Journal of the Atmospheric Sciences*, *31*(3), 646–673. https://doi.org/10.1175/1520-0469(1974)031<0646:FCTSAS>2.0.CO;2

Hillel, D. (2003). *Introduction to Environmental Soil Physics*. Elsevier. https://doi.org/10.1016/B978-0-12-348655-4.X5000-X

Hohenegger, C., & Stevens, B. (2018). The role of the permanent wilting point in controlling the spatial distribution of precipitation. *Proceedings of the National Academy of Sciences*, *115*(22), 5692–5697. https://doi.org/10.1073/pnas.1718842115

Hohenegger, C., Brockhaus, P., Bretherton, C. S., & Schär, C. (2009). The Soil Moisture–Precipitation Feedback in Simulations with Explicit and Parameterized Convection. *Journal of Climate*, *22*(19), 5003–5020. https://doi.org/10.1175/2009JCLI2604.1

Hu, X.-M., Xue, M., & McPherson, R. A. (2017). The Importance of Soil-Type Contrast in Modulating August Precipitation Distribution Near the Edwards Plateau and Balcones Escarpment in Texas. *Journal of Geophysical Research: Atmospheres*, *122*(20), 10,711-10,728. https://doi.org/10.1002/2017JD027035

Huang, Q., Marsham, J. H., Tian, W., Parker, D. J., & Garcia-Carreras, L. (2018). Large-eddy simulation of dust-uplift by a haboob density current. *Atmospheric Environment*, *179*(January), 31–39. https://doi.org/10.1016/j.atmosenv.2018.01.048

Jeevanjee, N., & Romps, D. M. (2015). Effective Buoyancy, Inertial Pressure, and the Mechanical Generation of Boundary Layer Mass Flux by Cold Pools. *Journal of the Atmospheric Sciences*, *72*(8), 3199–3213. https://doi.org/10.1175/JAS-D-14-0349.1

Kang, S.-L. (2016). Regional Bowen ratio controls on afternoon moist convection: A large eddy simulation study. *Journal of Geophysical Research: Atmospheres*, *121*(23), 14,056-14,083. https://doi.org/10.1002/2016JD025567

Khairoutdinov, M., & Randall, D. (2006). High-Resolution Simulation of Shallow-to-Deep Convection Transition over Land. *Journal of the Atmospheric Sciences*, *63*(12), 3421–3436. https://doi.org/10.1175/JAS3810.1

Koster, R. D., Dirmeyer, P. A., Guo, Z., Bonan, G., Chan, E., Cox, P., et al. (2004). Regions of Strong Coupling Between Soil Moisture and Precipitation. *Science*, *305*(5687), 1138–1140. https://doi.org/10.1126/science.1100217

Kristianti, F., Nguyen-Le, D., & Yamada, T. J. (2018). Effect of Soil Moisture on Shallow Cumulus Cloud in Large Eddy Simulation. *Journal of Japan Society of Civil Engineers, Ser. G (Environmental Research)*, *74*(5), I_33-I_40. https://doi.org/10.2208/jscejer.74.I_33

Kurowski, M. J., Suselj, K., Grabowski, W. W., & Teixeira, J. (2018). Shallow-to-Deep Transition of Continental Moist Convection: Cold Pools, Surface Fluxes, and Mesoscale Organization. *Journal of the Atmospheric Sciences*, *75*(12), 4071–4090. https://doi.org/10.1175/JAS-D-18-0031.1

Langhans, W., & Romps, D. M. (2015). The origin of water vapor rings in tropical oceanic cold pools. *Geophysical Research Letters*, *42*(18), 7825–7834. https://doi.org/10.1002/2015GL065623

Lawston, P. M. (2017). *Impacts of irrigation on land-atmosphere interactions in high-resolution model simulations* (Ph.D. dissertation). University of Delaware. Retrieved from https://pdfs.semanticscholar.org/8234/1ad3142ffd06780546c729a43e3ba0dd6ee0.pdf

Lee, T. J. (1992). *The impact of vegetation on the atmospheric boundary layer and convective storms*. Colorado State University.

Lee, T. J., & Pielke, R. A. (1992). Estimating the Soil Surface Specific Humidity. *Journal of Applied Meteorology*, *31*(5), 480–484. https://doi.org/10.1175/1520-0450(1992)031<0480:ETSSSH>2.0.CO;2

Li, Z., Zuidema, P., Zhu, P., & Morrison, H. (2015). The Sensitivity of Simulated Shallow Cumulus Convection and Cold Pools to Microphysics. *Journal of the Atmospheric Sciences*, *72*(9), 3340–3355. https://doi.org/10.1175/JAS-D-14-0099.1

Mallinson, H. M., & Lasher-Trapp, S. G. (2019). An Investigation of Hydrometeor Latent Cooling upon Convective Cold Pool Formation, Sustainment, and Properties. *Monthly Weather Review*, *147*(9), 3205–3222. https://doi.org/10.1175/MWR-D-18-0382.1

Mathworks. (2012). Contour Plots. Retrieved December 31, 2018, from https://web.archive.org/web/20120513041859/http://www.mathworks.fr/help/techdoc/creating_plots/f10-2524.html

McCaul Jr., E. W., & Cohen, C. (2002). The Impact on Simulated Storm Structure and Intensity of Variations in the Mixed Layer and Moist Layer Depths. *Monthly Weather Review*, *130*(7), 1722–1748. https://doi.org/10.1175/1520-0493(2002)130<1722:TIOSSS>2.0.CO;2

Meyers, M. P., Walko, R. L., Harrington, J. Y., & Cotton, W. R. (1997). New RAMS cloud microphysics parameterization. Part II: The two-moment scheme. *Atmospheric Research*, *45*(1), 3–39. https://doi.org/10.1016/S0169-8095(97)00018-5

Mission Research Corporation. (1997). RAMS Technical Description. Mission Research Corporation/*ASTER Division. Retrieved February 20, 2019, from https://vandenheever.atmos.colostate.edu/vdhpage/rams/docs/RAMS-TechnicalManual.pdf

Mohanty, B. P., & Zhu, J. (2007). Effective Hydraulic Parameters in Horizontally and Vertically Heterogeneous Soils for Steady-State Land–Atmosphere Interaction. *Journal of Hydrometeorology*, *8*(4), 715–729. https://doi.org/10.1175/JHM606.1

Moncrieff, M. W., & Liu, C. (1999). Convection Initiation by Density Currents: Role of Convergence, Shear, and Dynamical Organization. *Monthly Weather Review*, *127*(10), 2455–2464. https://doi.org/10.1175/1520-0493(1999)127<2455:CIBDCR>2.0.CO;2

Morin, J., & Benyamini, Y. (1977). Rainfall infiltration into bare soils. *Water Resources Research*, *13*(5), 813–817. https://doi.org/10.1029/WR013i005p00813

Morrison, H. (2012). On the robustness of aerosol effects on an idealized supercell storm simulated with a cloud system-resolving model. *Atmospheric Chemistry and Physics*, *12*(16), 7689–7705. https://doi.org/10.5194/acp-12-7689-2012

Nicolai-Shaw, N., Hirschi, M., Mittelbach, H., & Seneviratne, S. I. (2015). Spatial representativeness of soil moisture using in situ, remote sensing, and land reanalysis data. *Journal of Geophysical Research: Atmospheres*, *120*(19), 9955–9964. https://doi.org/10.1002/2015JD023305

Office of Naval Research. (2016). *Propagation of Intra-Seasonal Tropical Oscillations (PISTON) Science Plan*.

Park, S. (2014). A Unified Convection Scheme (UNICON). Part I: Formulation. *Journal of the Atmospheric Sciences*, *71*(11), 3902–3930. https://doi.org/10.1175/JAS-D-13-0233.1

Pei, S., Shinoda, T., Soloviev, A., & Lien, R.-C. (2018). Upper Ocean Response to the Atmospheric Cold Pools Associated With the Madden-Julian Oscillation. *Geophysical Research Letters*, *45*(10), 5020–5029. https://doi.org/10.1029/2018GL077825

Philip, J. R. (1957). Evaporation, and moisture and heat fields in the soil. *Journal of Meteorology*, *14*(4), 354–366. https://doi.org/10.1175/1520-0469(1957)014<0354:EAMAHF>2.0.CO;2

Pucillo, A., Miglietta, M. M., Lombardo, K., & Manzato, A. (2020). Application of a simple analytical model to severe winds produced by a bow echo like storm in northeast Italy. *Meteorological Applications*, *27*(1), 1–18. https://doi.org/10.1002/met.1868

Purdom, J. F. W. (1982). Subjective interpretation of geostationary satellite data for nowcasting. *Nowcasting*, 149–166.

Randall, D., Khairoutdinov, M., Arakawa, A., & Grabowski, W. (2003). Breaking the Cloud Parameterization Deadlock. *Bulletin of the American Meteorological Society*, *84*(11), 1547–1564. https://doi.org/10.1175/BAMS-84-11-1547

Redl, R., Fink, A. H., & Knippertz, P. (2015). An Objective Detection Method for Convective Cold Pool Events and Its Application to Northern Africa. *Monthly Weather Review*, *143*(12), 5055–5072. https://doi.org/10.1175/MWR-D-15-0223.1

Riley Dellaripa, E. M., Maloney, E. D., Toms, B. A., Saleeby, S. M., & van den Heever, S. C. (2020). Topographic Effects on the Luzon Diurnal Cycle during the BSISO. *Journal of the Atmospheric Sciences*, *77*(1), 3–30. https://doi.org/10.1175/JAS-D-19-0046.1

Rio, C., Hourdin, F., Grandpeix, J.-Y., & Lafore, J.-P. (2009). Shifting the diurnal cycle of parameterized deep convection over land. *Geophysical Research Letters*, *36*, L07809. https://doi.org/10.1029/2008GL036779

Rio, C., Grandpeix, J.-Y., Hourdin, F., Guichard, F., Couvreux, F., Lafore, J.-P., et al. (2013). Control of deep convection by sub-cloud lifting processes: the ALP closure in the LMDZ5B general circulation model. *Climate Dynamics*, *40*(9–10), 2271–2292. https://doi.org/10.1007/s00382-012-1506-x

Rodell, M., Beaudoing, H. K., L'Ecuyer, T. S., Olson, W. S., Famiglietti, J. S., Houser, P. R., et al. (2015). The Observed State of the Water Cycle in the Early Twenty-First Century. *Journal of Climate*, *28*(21), 8289–8318. https://doi.org/10.1175/JCLI-D-14-00555.1

Rotunno, R., Klemp, J. B., & Weisman, M. L. (1988). A Theory for Strong, Long-Lived Squall Lines. *Journal of the Atmospheric Sciences*, *45*(3), 463–485. https://doi.org/10.1175/1520-0469(1988)045<0463:ATFSLL>2.0.CO;2

Saleeby, S. M., & Cotton, W. R. (2004). A Large-Droplet Mode and Prognostic Number Concentration of Cloud Droplets in the Colorado State University Regional Atmospheric Modeling System (RAMS). Part I: Module Descriptions and Supercell Test Simulations. *Journal of Applied Meteorology*, *43*(1), 182–195. https://doi.org/10.1175/1520-0450(2004)043<0182:ALMAPN>2.0.CO;2

Saleeby, S. M., & Cotton, W. R. (2008). A Binned Approach to Cloud-Droplet Riming Implemented in a Bulk Microphysics Model. *Journal of Applied Meteorology and Climatology*, *47*(2), 694–703. https://doi.org/10.1175/2007JAMC1664.1

Saleeby, S. M., & van den Heever, S. C. (2013). Developments in the CSU-RAMS aerosol model: Emissions, nucleation, regeneration, deposition, and radiation. *Journal of Applied Meteorology and Climatology*, *52*(12), 2601–2622. https://doi.org/10.1175/JAMC-D-12-0312.1

Santanello, J. A., Dirmeyer, P. A., Ferguson, C. R., Findell, K. L., Tawfik, A. B., Berg, A., et al. (2017). Land–Atmosphere Interactions: The LoCo Perspective. *Bulletin of the American Meteorological Society*, *99*(6), 1253–1272. https://doi.org/10.1175/BAMS-D-17-0001.1

Schiro, K. A., & Neelin, J. D. (2018). Tropical continental downdraft characteristics: mesoscale systems versus unorganized convection. *Atmospheric Chemistry and Physics*, *18*(3), 1997–2010. https://doi.org/10.5194/acp-18-1997-2018

Schlemmer, L., & Hohenegger, C. (2014). The Formation of Wider and Deeper Clouds as a Result of Cold-Pool Dynamics. *Journal of the Atmospheric Sciences*, *71*(8), 2842–2858. https://doi.org/10.1175/JAS-D-13-0170.1

Schlemmer, L., & Hohenegger, C. (2016). Modifications of the atmospheric moisture field as a result of cold-pool dynamics. *Quarterly Journal of the Royal Meteorological Society*, *142*(694), 30–42. https://doi.org/10.1002/qj.2625

Smagorinsky, J. (1963). General circulation experiments with the primitive equations I. The basic experiment. *Monthly Weather Review*, *91*(3), 99–164. https://doi.org/10.1175/1520-0493(1963)091<0099:GCEWTP>2.3.CO;2

Stull, R. B. (1988). Boundary Conditions and Surface Forcings. In R. B. Stull (Ed.), *An Introduction to Boundary Layer Meteorology* (pp. 251–294). Dordrecht: Springer Netherlands. https://doi.org/10.1007/978-94-009-3027-8_7

Suselj, K., Kurowski, M. J., & Teixeira, J. (2019). A Unified Eddy-Diffusivity/Mass-Flux Approach for Modeling Atmospheric Convection. *Journal of the Atmospheric Sciences*, JAS-D-18-0239.1. https://doi.org/10.1175/JAS-D-18-0239.1

Tan, J., Huffman, G. J., Bolvin, D. T., & Nelkin, E. J. (2019). Diurnal Cycle of IMERG V06 Precipitation. *Geophysical Research Letters*, *46*(22), 13584–13592. https://doi.org/10.1029/2019GL085395

Taylor, C. M., Jeu, R. A. M. de, Guichard, F., Harris, P. P., & Dorigo, W. A. (2012). Afternoon rain more likely over drier soils. *Nature*, *489*(7416), 423–426. https://doi.org/10.1038/nature11377

Tegen, I., & Fung, I. (1994). Modeling of mineral dust in the atmosphere: Sources, transport, and optical thickness. *Journal of Geophysical Research: Atmospheres*, *99*(D11), 22897–22914. https://doi.org/10.1029/94JD01928

Tompkins, A. M. (2001). Organization of Tropical Convection in Low Vertical Wind Shears: The Role of Cold Pools. *Journal of the Atmospheric Sciences*, *58*(13), 1650–1672. https://doi.org/10.1175/1520-0469(2001)058<1650:OOTCIL>2.0.CO;2

Toms, B. A., van den Heever, S. C., Riley Dellaripa, E. M., Saleeby, S. M., & Maloney, E. D. (2020). The Boreal Summer Madden–Julian Oscillation and Moist Convective Morphology over the Maritime Continent. *Journal of the Atmospheric Sciences*, *77*(2), 647–667. https://doi.org/10.1175/JAS-D-19-0029.1

Torri, G., & Kuang, Z. (2016). Rain evaporation and moist patches in tropical boundary layers. *Geophysical Research Letters*, *43*(18), 9895–9902. https://doi.org/10.1002/2016GL070893

Torri, G., Kuang, Z., & Tian, Y. (2015). Mechanisms for convection triggering by cold pools. *Geophysical Research Letters*, *42*(6), 1943–1950. https://doi.org/10.1002/2015GL063227

Tuttle, S., & Salvucci, G. (2016). Empirical evidence of contrasting soil moisture–precipitation feedbacks across the United States. *Science*, *352*(6287), 825–828. https://doi.org/10.1126/science.aaa7185

van den Heever, S. C., & Cotton, W. R. (2004). The Impact of Hail Size on Simulated Supercell Storms. *Journal of the Atmospheric Sciences*, *61*(13), 1596–1609. https://doi.org/10.1175/1520-0469(2004)061<1596:TIOHSO>2.0.CO;2

Walko, R. L., Band, L. E., Baron, J., Kittel, T. G. F., Lammers, R., Lee, T. J., et al. (2000). Coupled Atmosphere–Biophysics–Hydrology Models for Environmental Modeling. *Journal of Applied Meteorology*, *39*(6), 931–944. https://doi.org/10.1175/1520-0450(2000)039<0931:CABHMF>2.0.CO;2

Williams, E., & Stanfill, S. (2002). The physical origin of the land–ocean contrast in lightning activity. *Comptes Rendus Physique*, *3*(10), 1277–1292. https://doi.org/10.1016/S1631-0705(02)01407-X

Wilson, J. W., & Schreiber, W. E. (1986). Initiation of Convective Storms at Radar-Observed Boundary-Layer Convergence Lines. *Monthly Weather Review*, *114*(12), 2516–2536. https://doi.org/10.1175/1520-0493(1986)114<2516:IOCSAR>2.0.CO;2

Yuan, S., Wang, Y., Quiring, S. M., Ford, T. W., & Houston, A. L. (2020). A sensitivity study on the response of convection initiation to in situ soil moisture in the central United States. *Climate Dynamics*, *54*(3), 2013–2028. https://doi.org/10.1007/s00382-019-05098-0

Zhao, M., Golaz, J.-C., Held, I. M., Guo, H., Balaji, V., Benson, R., et al. (2018). The GFDL Global Atmosphere and Land Model AM4.0/LM4.0: 2. Model Description, Sensitivity Studies, and Tuning Strategies. *Journal of Advances in Modeling Earth Systems*, *10*(3), 735–769. https://doi.org/10.1002/2017MS001209

Zuidema, P., Torri, G., Muller, C., & Chandra, A. (2017). A Survey of Precipitation-Induced Atmospheric Cold Pools over Oceans and Their Interactions with the Larger-Scale Environment. *Surveys in Geophysics*, *38*(6), 1283–1305. https://doi.org/10.1007/s10712-017-9447-x

APPENDIX: SUPPORTING INFORMATION FOR CHAPTER 2

A.1 Cold Pool Identification and Tracking: Updates to Drager and van den Heever (2017)

The algorithm contains three steps: (1) identification of cold pools at each output time, (2) preliminary tracking across output times to prevent double-counting, and (3) final tracking across output times.

As part of the data post-processing, RAMS model outputs are coarsened in the horizontal to a 250 m × 250 m grid prior to analysis by replacing the values in each 2 × 2 square with their arithmetic mean. This step helps to expedite the subsequent analyses while preserving all features that are resolved by the model grid.

Step 1: Rain Shafts and Cold Pool Boundaries

Convective cold pools only form in the presence of precipitation (either aloft or at the surface). Therefore, Step 1 begins with the identification of cold pools' parent rain shafts. One modification of the Drager and van den Heever (2017) algorithm is that the surface rainfall rate threshold is replaced with local rain water path maxima in order to permit the detection of cold pools spawned by virga. The $z \sim 0$ m to $z \sim 3000$ m rain water path is calculated, and rain water path values less than 0.1 mm are set to zero. Then, regions of non-zero rain water path containing 3 or fewer contiguous grid cells (where grid cells sharing edges or corners are considered contiguous) are also set to zero. The resulting two-dimensional field contains contiguous regions of non-zero values at least 4 grid cells in area. This field is then smoothed using a circular moving average ("pillbox") filter with a two-grid cell (500 m, on the coarsened 250 m grid) radius. Locations of local maxima in the resulting smoothed, filtered RWP field, each of which represents a single rain shaft, are taken to be potential cold pool formation locations.

Ten simulation minutes following the identification of RWP maxima, $\frac{\partial^2 \widehat{\theta_\rho}}{\partial r^2}$ is calculated for each RWP maximum, where $\widehat{\theta_\rho}$ is the horizontally smoothed density potential temperature field at $z \sim 20$ m ($k = 2$) and r is a cylindrical polar radial coordinate centered on the RWP local maximum. The $\widehat{\theta_\rho}$ field is obtained by convolving the original, full-resolution ($\Delta x = \Delta y = 125$ m, prior to coarsening) θ_ρ field with a pillbox filter with a four-grid cell (500 m) radius and then coarsening the result to a $\Delta x = \Delta y = 250$ m grid according to the procedure given in Section 2.1. This smoothing step represents another update to the Drager and van den Heever (2017) algorithm and was added in order to minimize the influence of small-scale horizontal fluctuations, which are better-resolved here than in the $\Delta x = \Delta y = 1000$ m simulation analyzed in Drager and van den Heever (2017), on the spatial derivatives.

The MATLAB contouring algorithm (Mathworks, 2012) is used to obtain closed contours (i.e., polygons) along which $\frac{\partial^2 \widehat{\theta_\rho}}{\partial r^2} \approx 0$ K m^{-2} [see Figure 8 of Drager and van den Heever (2017)] within a 60 km × 60 km subdomain centered at $r = 0$ km. These are taken to be candidate cold pool boundaries. A cold pool is identified if there exists at least one contour that satisfies the following criteria:

1A. The contour must be closed.

1B. The contour must contain at least 4 points.

1C. The contour must enclose the point $r = 0$ km.

1D. The mean value of $\frac{\partial \widehat{\theta_\rho}}{\partial r}$ calculated along the contour path must be positive (corresponding to a transition from lower $\widehat{\theta_\rho}$ to higher $\widehat{\theta_\rho}$ in the radially outward direction).

1E. The contour must enclose an area with an equivalent diameter (calculated as $2\sqrt{\frac{\text{area}}{\pi}}$) between 1 km and 8 km.

1F. The location of the centroid of the contour must be less than 1 equivalent diameter away from the point $r = 0$ km.

1G. The solidity of the contour (defined as the ratio of its area to the area of its convex hull) must be at least 0.8, following Drager and van den Heever (2017).

If more than one contour satisfies these criteria (very rare), then the contour with the least (most negative) contour-path-averaged θ_ρ advection is selected as the cold pool boundary. At this point, if a contour is selected, then future calculations will take the centroid of this contour to be the cold pool center.

Step 2: Preliminary Tracking to Avoid Double-Counting

Step 1 results in a collection of cold pool boundaries at each output time. If a cold pool's parent rain shaft persists across two or more output times, then the cold pool may appear in the data set more than once. Therefore, in Step 2, preliminary tracking is used to eliminate cold pools appearing for the second time or beyond (thereby preventing double-counting), as well as to establish a reference time for each cold pool. The specific method for the Step 2 preliminary tracking is as follows:

2A. For a given contour c at output time number τ, find all of the cold pool boundary contours at output time $\tau + 1$ (five minutes later) whose centroids are enclosed by c and are a distance less than half of c's equivalent diameter from c's centroid.

2B. For the remaining candidate contours d_i, define the overlap region $c \cap d_i$. Select the contour for which the product $\frac{\text{area}(c \cap d_i)}{\text{area}(c)} \cdot \frac{\text{area}(c \cap d_i)}{\text{area}(d_i)}$ ("overlap product") is maximized.

2C. For the contour d selected in 2B, assess whether $\frac{\text{area}(c \cap d)}{\text{area}(c)}$ and $\frac{\text{area}(c \cap d)}{\text{area}(d)}$ are each at least 0.25. If (and only if) this is the case, then consider contour d to be an extension of contour c at output time $\tau + 1$, remove contour d from consideration as a potential new cold pool (and from consideration as an extension of any other cold pool at output time number τ), and follow the same procedure (starting with 2A) to compare contour d to cold pool boundary contours at output time $\tau + 2$. Otherwise, stop attempting to track contour c, and move on to the next contour at output time number τ.

The time of each cold pool's initial detection is defined as $t = 0$ minutes. For example, if a cold pool is detected at 14:15 LT, 14:20 LT, and 14:25 LT, then $t = 0$ minutes for that cold pool is defined to be 14:15 LT.

Step 3: Final Tracking

The preliminary tracking in Step 2 is useful for preventing double-counting, but it is fundamentally limited in that it only considers boundaries appearing a maximum of 10 simulation minutes after the parent rain shaft dissipates. Therefore, we have added an additional processing step, Step 3, in which cold pools are tracked anew, starting from the $t = 0$ minutes boundaries. Each remaining cold pool in the data set is tracked backward and forward in time (where possible, as far backward as $t = -30$ minutes and as far forward as $t = 60$ minutes) starting from $t = 0$ minutes, so as to obtain a series of one or more contours for each cold pool. This tracking step assumes that cold pools are stationary. The following tracking procedure is used:

3A. First, attempt to recalculate the cold pool boundary at $t = 0$ minutes. Recall that the original cold pool boundary contours are based upon the zero contours of $\frac{\partial^2 \widehat{\theta_\rho}}{\partial r^2}$, where r is defined relative to the location of the local maximum in rain water path (i.e., the rain

shaft). In this step, r is redefined to be centered at the location of the centroid of the original cold pool boundary, and $\frac{\partial^2 \widehat{\theta_\rho}}{\partial r^2}$ is recalculated on a new 60 km × 60 km subdomain centered at the same location. Zero contours are located using the same MATLAB contouring algorithm as before, and the best contour is identified using the same tests as in 1A–1G, with the following exceptions:

a. Test 1E (the area restriction) is not applied.

b. Test 1F is modified to use a threshold distance of half the equivalent diameter.

If multiple contours satisfy these criteria, then the one with the highest overlap product (see Step 2B) with the original contour is selected. Two additional criteria are applied to the contour with the highest overlap product: each ratio within the overlap product must be at least 0.9, and the solidity must "improve," i.e., the contour's solidity must be greater than or equal to that of the original cold pool boundary. If this contour satisfies all criteria, then it replaces the original cold pool boundary for the remainder of the analysis. Otherwise, the original cold pool boundary is retained.

3B. Calculate the $\frac{\partial^2 \widehat{\theta_\rho}}{\partial r^2}$ field at every output time ranging from $t = -30$ minutes to $t = 60$ minutes on the same subdomain and using the same radial coordinate as in Step 3A. Implicit in this step is the assumption that the center of the cold pool does not move over time.

3C. Track cold pools backward in time, starting from $t = 0$ minutes, using essentially the same procedure as was used in Step 3A to attempt to recalculate the cold pool boundary at $t = 0$ minutes. In the first backward-tracking step, the zero contours of $\frac{\partial^2 \widehat{\theta_\rho}}{\partial r^2}$ at $t = -5$ minutes are compared to the cold pool boundary at $t = 0$ minutes. If a boundary is

identified at $t = -5$ minutes, then this boundary is compared to the zero contours of $\frac{\partial^2 \widehat{\theta_\rho}}{\partial r^2}$ at $t = -10$ minutes, and so on. If no zero contour is selected as the cold pool boundary, then tracking ceases. Two modifications are made to the procedure in Step 3A when tracking across different output times. Firstly, the requirement that solidity "improve" is not applied. Secondly, in order to account for expanding cold pools, the area enclosed by the cold pool boundary at each earlier time need only occupy at least 25%, rather than 90%, of the area at the later time. The cold pool at the later time does still need to occupy at least 90% of the cold pool at the earlier time.

3D. Track cold pools forward in time, starting from $t = 0$ minutes, using the same procedure as in Step 3C except directed toward higher values of t.

A.2 Algorithm Performance

Snapshots of cold pool boundaries identified at 13:00 LT, 14:00 LT, and 15:00 LT in the WET-SOIL and DRY-SOIL simulations are provided in Figure A.1. Many cold pools are correctly identified, but false negatives and false positives both exist. Most, but not all, of the false negatives are mature cold pools that were identified earlier in their lifecycles (not shown) but for which our methods can no longer discern a boundary contour meeting all selection criteria. The false positives, evident primarily in the DRY-SOIL snapshot, arise when some zero-contour of $\frac{\partial^2 \widehat{\theta_\rho}}{\partial r^2}$ that circumscribes multiple cold pools happens to meet the Step 1 criteria outlined in Section A.1. We performed an analysis in which we manually identified and excluded these "false cold pools," which were found to represent approximately 5 – 10% of the identified cold pools. Their removal did not substantially affect the trends with respect to soil moisture presented in the main text.

Figures A.2a, A.2b, and A.2c show time series of the number of rain shafts (local maxima in the 0 – 3 km rain water path), number of cold pools ("Step 1" in Section A.1), and number of new (unique) cold pools following preliminary tracking ("Step 2" in Section A.1), respectively, at each output time. For plotting purposes, the number of rain shafts is shifted 10 minutes (2 output times) forward in time. This is in accordance with the fact that cold pools are detected 10 minutes following the identification of their parent rain shafts. The DRY-SOIL simulation consistently exhibits the most rain shafts (Figure A.2a) and the most new cold pools (Figure A.2c). However, during the afternoon hours, the DRY-SOIL simulation does not have the greatest number of non-unique cold pools (Figure A.2b). Considered together, these results imply that in the DRY-SOIL simulation (compared to the other three simulations), a smaller fraction of rain shafts spawn cold pools that are detectable by our identification algorithm, and that these cold pools are detected for fewer consecutive output times (due to shorter-lived rain shafts and/or shorter-lived cold pools).

A.3 Figures

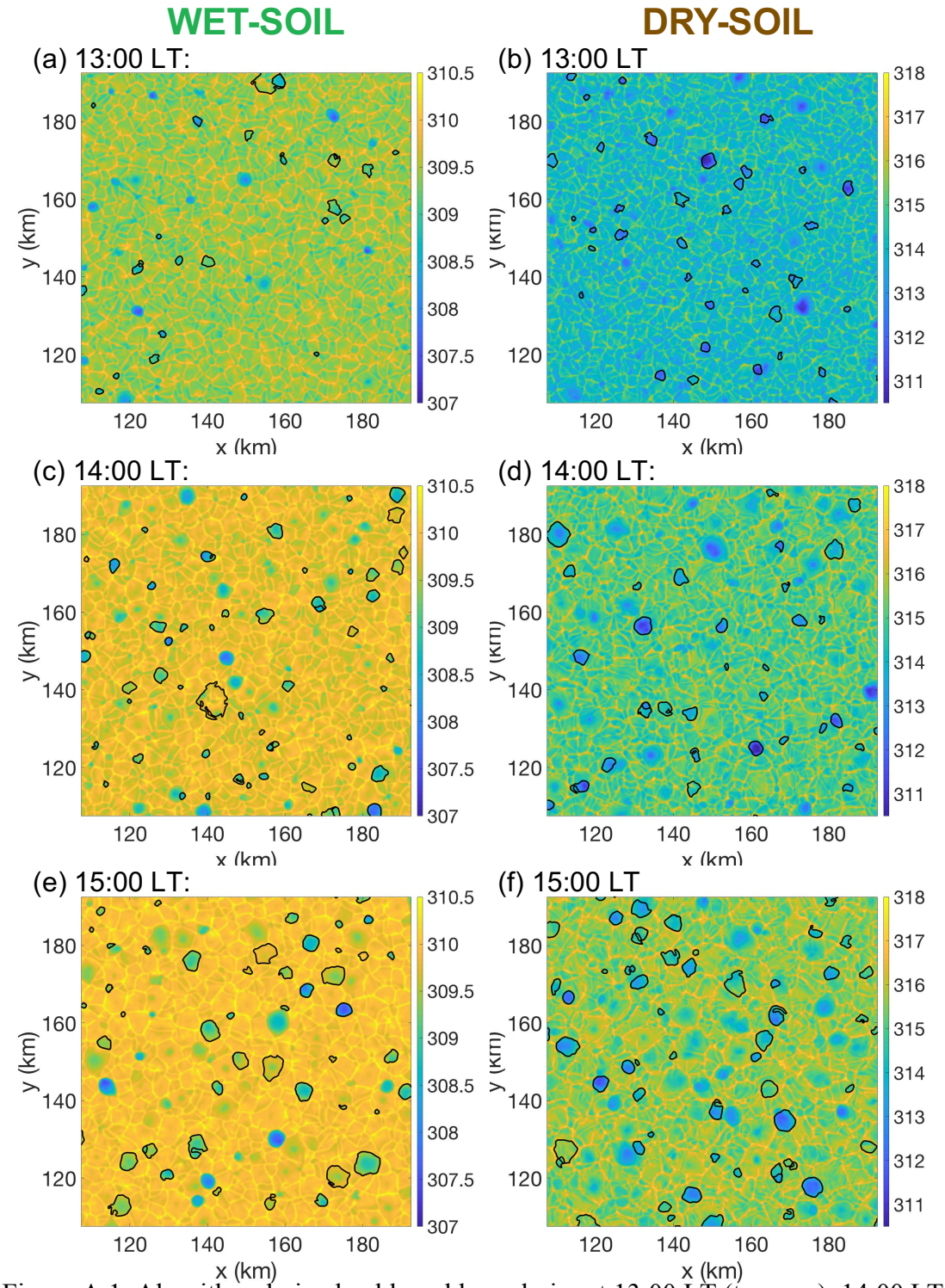

Figure A.1. Algorithm-derived cold pool boundaries at 13:00 LT (top row), 14:00 LT (middle row), and 15:00 LT (bottom row) within 80 km × 80 km subsets of the domain for the WET-SOIL (left column) and DRY-SOIL (right column) simulations. In all panels, the colors indicate θ_ρ (density potential temperature) at the lowest above-ground model level, $z \sim 20$ m (note

different color scales for WET-SOIL versus DRY-SOIL), and the black contours indicate algorithm-derived cold pool boundaries.

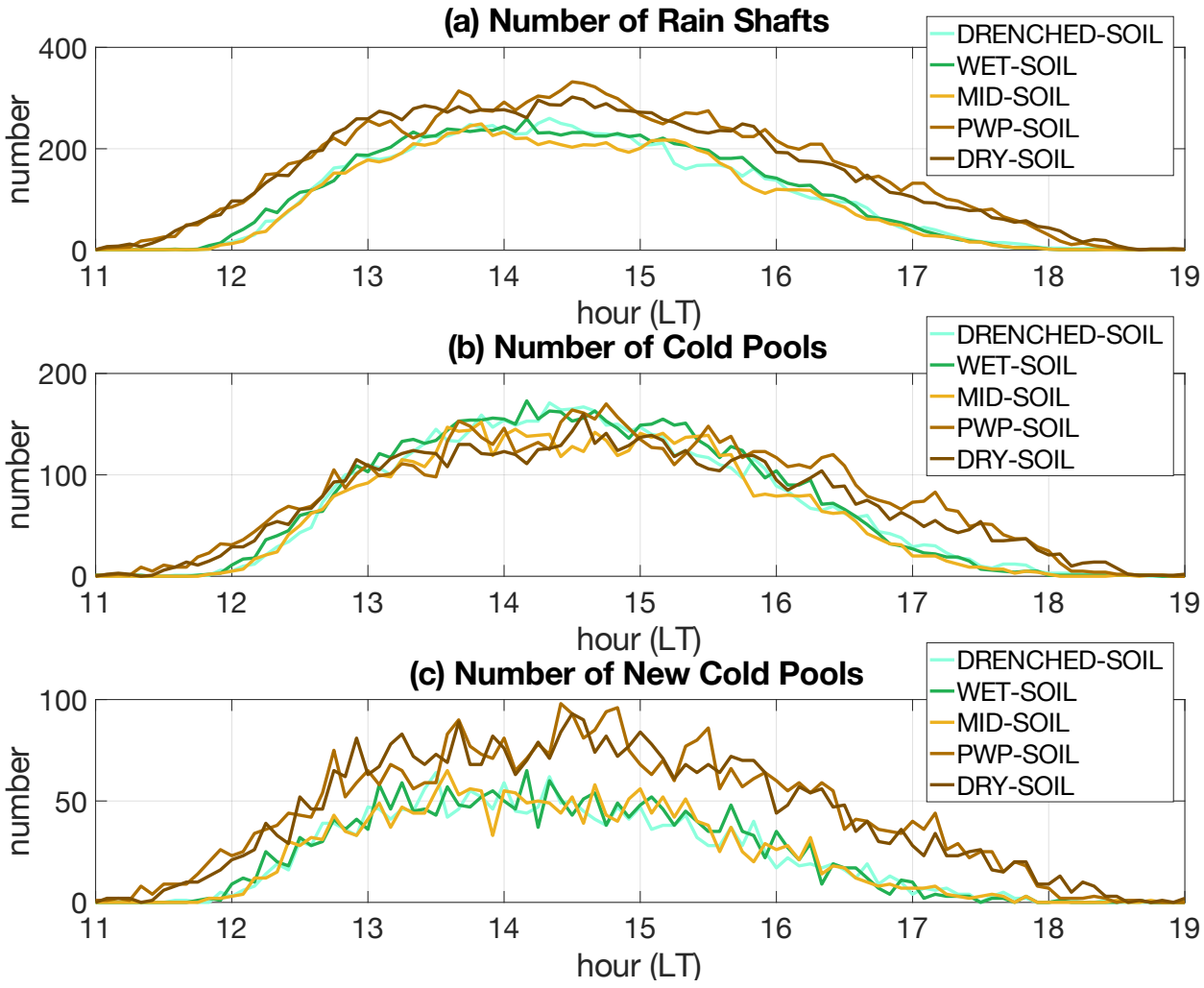

Figure A.2. Time series of (a) the number of rain shafts identified 10 minutes before a given output time, (b) number of cold pools identified at a given output time, and (c) number of new cold pools, i.e., cold pools that cannot be traced back to an earlier detected cold pool, at each output time.